UNIVERSIDAD DE CHILE
FACULTAD DE CIENCIAS FÍSICAS Y MATEMÁTICAS
DEPARTAMENTO DE INGENIERÍA ELÉCTRICA

DROOP-CONTROLLED INVERTERS SMALL-SIGNAL IMPEDANCE CHARACTERIZATION FOR STABILITY STUDIES

TESIS PARA OPTAR AL GRADO DE
MAGÍSTER EN CIENCIAS DE LA INGENIERÍA, MENCIÓN ELÉCTRICA

MEMORIA PARA OPTAR AL TÍTULO DE INGENIERO CIVIL ELÉCTRICO

NICOLÁS FRANCISCO MIRA GEBAUER

PROFESOR GUÍA:
PATRICIO MENDOZA ARAYA

MIEMBROS DE LA COMISIÓN:
CLAUDIA RAHMANN ZÚÑIGA
FREDDY FLORES BAHAMONDE

Este trabajo ha sido parcialmente financiado por Conicyt Proyecto
PFCHA/MagísterNacional/2017- 22172061

SANTIAGO DE CHILE
2019

RESUMEN DE LA MEMORIA PARA OPTAR AL
TÍTULO DE INGENIERO CIVIL ELÉCTRICO Y DE LA
TESIS PARA OPTAR AL GRADO DE MAGÍSTER EN
CIENCIAS DE LA INGENIERÍA, MENCIÓN ELÉCTRICA
POR: NICOLÁS FRANCISCO MIRA GEBAUER
FECHA: 2019
PROF. GUÍA: PATRICIO MENDOZA ARAYA

DROOP-CONTROLLED INVERTERS SMALL-SIGNAL IMPEDANCE CHARACTERIZATION FOR STABILITY STUDIES

Las microrredes son una de las tecnologías claves para la integración de grandes cantidades de tecnologías de generación a partir de fuentes renovables a la red eléctrica. Las principales fuentes de generación dentro de una microrred son los dispositivos de electrónica de potencia, responsables de la conversión de energía y del control necesario para la operación. La interacción dinámica entre la microrred y una fuente basada en electrónica de potencia recién integrada puede llevar a inestabilidad de pequeña señal. Es por esto que distintos enfoques para el estudio de estabilidad se han desarrollado en los últimos años, particularmente métodos para asegurar estabilidad a través de la división del sistema en subsistemas para la fuente y para la carga, aplicando posteriormente el criterio de Nyquist a la respectiva razón de impedancias fuente/carga. Sin embargo, este aspecto ha sido raramente estudiado considerando inversores controlados por droop, en los cuales el control de potencia activa impacta además la frecuencia de salida de las fuentes, teniendo un impacto considerable en las impedancias de pequeña señal de los inversores.

El principal objetivo de esta tesis es la caracterización de la impedancia de pequeña señal de inversores controlados por control droop, típicamente usados en microrredes, mediante modelos simplificados, en función de lograr un amplio entendimiento de su comportamiento ante cambios en las condiciones de operación. Este trabajo postula como hipótesis que el comportamiento general de la impedancia de pequeña señal de inversores controlados por droop ante cambios en las condiciones de operación puede ser caracterizada a través del análisis de la funcion de transferencia MIMO (múltiples-entradas múltiples-salidas) de modelos linealizados de inversores de orden reducido, al contrastarla con las impedancias de pequeña señal de modelos más complejos.

Los resultados obtenidos muestran que la impedancia de pequeña señal de este tipo de inversores fué efectivamente caracterizada, especialmente por uno de los modelos propuestos. Dos indicadores fueron desarrollados para cuantificar los resultados obtenidos de manera gráfica, los cuales confirmaron el desempeño de los modelos desarrollados, especialmente con respecto a los canales DD, DQ y QD, identificando correctamente las variables de operación que más impactan la impedancia de pequeña señal al ser perturbadas. Los resultados indican además que principalmente es el rango de baja frecuencia de la impedancia de pequeña señal el que se ve mayormente afectado al cambiar las condiciones de operación, mientras que el rango de frecuencias altas tiende a converger a la impedancia de gran señal.

Este trabajo de tesis podría llevar a mejores estudios de estabilidad de pequeña señal, en los cuales uno de los mayores problemas hoy en día es la dependencia de la impedancia de pequeña señal con respecto a los cambios en el punto de operación del sistema.

RESUMEN DE LA MEMORIA PARA OPTAR AL
TÍTULO DE INGENIERO CIVIL ELÉCTRICO Y DE LA
TESIS PARA OPTAR AL GRADO DE MAGÍSTER EN
CIENCIAS DE LA INGENIERÍA, MENCIÓN ELÉCTRICA
POR: NICOLÁS FRANCISCO MIRA GEBAUER
FECHA: 2019
PROF. GUÍA: PATRICIO MENDOZA ARAYA

DROOP-CONTROLLED INVERTERS SMALL-SIGNAL IMPEDANCE CHARACTERIZATION FOR STABILITY STUDIES

Microgrids are one of the key technologies to facilitate the integration of large amounts of renewable generation technologies to the main grid. The main power supplies inside the microgrid are power electronic devices which are responsible for energy conversion and provide the necessary control. Dynamical interactions between the microgrid and newly connected power electronic-based sources can lead to small-signal instability. Hence, several stability analysis approaches have been developed over the recent years, particularly methods to ensure stability by first dividing the system into source and load subsystems and then applying the Nyquist criterion to the respective source/load impedances ratio. Nevertheless, this aspect has been rarely studied considering droop-controlled inverters, as the active power droop control also impacts the output frequency of micro-sources and has a deep impact in the small-signal impedances of the inverters.

The main objective of this thesis is to characterize the small-signal impedance of droop-controlled inverters typically used in microgrids through simplified models, in order to achieve a comprehensive understanding of their behavior. This work postulates as hypothesis that the general behavior of the small-signal impedance of droop-controlled inverters when operation conditions change can be characterized through the analysis of the transfer functions of linearized multi-input multi-output reduced-order inverter models, by contrasting them with the resulting small-signal impedances of more complex models.

The obtained results show that the small-signal impedance of these inverters were effectively characterized, specially by one of the proposed models. Two indices were developed in order to quantify the graphically obtained results, which confirmed the performance of the developed models, specially with respect to DD, DQ and QD-Channels.The indices confirmed the identification of the operating variables that impact the small-signal impedance the most when perturbed. The results also indicate that the low-frequency range of the small-signal impedance is the most affected range when changing the operating conditions, as the high-frequency range tends to converge to the large-signal impedance.

This work could lead to improved small-signal stability studies, in which one of the biggest problems nowadays is the dependence of the small-signal impedance on the changing operating point.

Para mi familia, mis amigos y en especial, Pelu.

Agradecimientos

En primer lugar quiero agradecer a mis padres Jorge y Yenny, gracias a quienes puedo estar hoy aquí. Gracias a su formación, enseñanzas y paciencia puedo ser la persona que soy hoy. También quiero extender este agradecimiento a toda mi familia, partiendo por mis hermanos Coke, Juanpa y Carlitos, quienes mas de una vez tuvieron que aguantar alguna que otra rabieta relacionada a mis estudios, tanto en el colegio como en la universidad.

También agradezco a todos mis amigos, tanto valdivianos como los que fuí haciendo en el camino, quienes de una u otra forma se han hecho parte de mi vida y espero que lo sigan siendo por toda la vida. En particular agradezco la comprensión al momento de ausentarme por períodos al priorizar muchas veces los estudios. Un abrazo en particular a Gabriel, cuyo recuerdo estará siempre presente.

Agradezco de manera especial a mi Pelu, quien estuvo en los momentos más difíciles de este proceso, de muchos altibajos, y que sin ella no habría sido posible lograr los resultados que logré. Gracias por estar siempre en todas y apoyarme en todo momento, te amo muchísimo y para siempre. Sé que podré contar contigo en los innumerables desafíos que vendrán de aquí en más.

Finalmente quiero darle las gracias a quienes han sido parte de este trabajo. Al profesor Patricio, con quien ideamos este proyecto y el cual venimos trabajando desde el año 2017. A la proferosa Claudia, quien ha sido fundamental en el desarrollo de este trabajo y quien ha influido enormemente en la finalización del mismo, brindando ideas nuevas cuando parecían no haber resultados exitosos. Espero que podamos seguir trabajando juntos en el futuro. A Freddy, quien se sumó a los esfuerzos y con quien pudimos darle el cierre definitivo al trabajo.

Se agradece el apoyo otorgado por Conicyt a través de los programas PFCHA/Magíster Nacional/2017- 22172061, FONDAP - 15110019 y REDES ETAPA INICIAL - REDI170224.

Contents

List of Tables

List of Figures

Nomenclature

δ	Reference frame angle with respect to the common reference frame [°]
δ_i	Reference frame angle of the ith inverter [°]
γ	Current controller auxiliary variable
ω	Angular frequency [rad/s]
ω^*	Angular frequency reference [rad/s]
ω_c	Low-pass filter cut-off frequency [rad/s]
ω_i	Angular frequency of the ith inverter [rad/s]
ω_n	Rated angular frequency [rad/s]
ω_{com}	Angular frequency of the common reference [rad/s]
$\omega_{j,k}^{p_i}$	Frequency of the poles of the small-signal impedance, with $j = \{D, Q\}$ and $k = \{D, Q\}$ referring to the respective rotating reference frame channel, and i indicating the corresponding pole [rad/s]
$\omega_{j,k}^{z_i}$	Frequency of the zeros of the small-signal impedance, with $j = \{D, Q\}$ and $k = \{D, Q\}$ referring to the respective rotating reference frame channel, and i indicating the corresponding zero [rad/s]
ω_{max}	Maximum angular frequency [rad/s]
ω_{min}	Minimum angular frequency [rad/s]
ϕ	Voltage controller auxiliary variable
$\phi_{j,k}^0$	Phase of the zero frequency value of the small-signal impedance, with $j = \{D, Q\}$ and $k = \{D, Q\}$ referring to the respective rotating reference frame channel for a specific inverter model
θ	Rotating angle [°]
ξ	Damping factor of the system

a_n	Multiplicity of the zeros of the system
AC	Alternating current
b_n	Multiplicity of the poles of the system
$BESS$	Battery energy storage system
C_F or C_f	Output filter capacitance [F]
CSC	Current source converter
DC	Direct current
DER	Distributed energy resources
DG	Diesel Generation
dq	Direct-quadrature reference frame
E^*	Output voltage reference [V]
EPS	Electric power sources
$H(s)$ or $G(s)$	Transfer function of the system
$H_1(s)$	Subsystem 1 transfer function relating input current and output voltage
$H_1^\omega(s)$	Subsystem 1 transfer function relating input angular frequency and output voltage
$H_2(s)$	Subsystem 2 transfer function relating input voltage and output current
$H_2^\omega(s)$	Subsystem 2 transfer function relating input voltage and output angular frequency
I_f^1	Index 1
I_f^2	Index 2
i_l	Current at the input of the output filter [A]
i_l^*	Current reference at the input of the output filter [A]
i_o	Output current [A]
i_{PoC}	Current at the PoC [A]
$IEEE$	Institute of Electrical and Electronics Engineers
K_{ic}	Current controller PI integral coefficient

K_{iv}	Voltage controller PI integral coefficient
K_{pc}	Current controller PI proportional coefficient
K_{pv}	Voltage controller PI proportional coefficient
L_C or L_c	Output filter inductance [H]
L_F or L_f	Output filter inductance [H]
M_i	Model i of the inverter, with $i = 1, 2, 3, 4, 5, 6$
m_p	Active power droop gain
$MIMO$	Multi-input multi-output
n_p	Number of poles
n_q	Reactive power droop gain
n_z	Number of zeros
P	Measured active power [W]
p	Output active power [W]
P^*	Output active power reference [W]
P^c	Critical active power that determines the zeros complexity in model 2 [W]
P_+^c	Critical active power that determines the existence of a positive zero in model 2 [W]
P_n	Rated active power [W]
p_n	Poles of the system
$p_{j,k}^{M_i}$	Poles of the small-signal impedance, with $j = \{D, Q\}$ and $k = \{D, Q\}$ referring to the respective rotating reference frame channel, and $i = \{1, 2, 3\}$ indicating the corresponding model
P_{max}	Maximum active power [W]
PI	Proportional–integral controller
PLL	Phase-locked loop
PoC	Point of connection
Q	Measured reactive power [W]

q	Output reactive power [W]
Q^*	Output reactive power reference [VAr]
Q_{max}	Maximum reactive power [VAr]
R	Resistance [Ω]
RES	Renewable energy sources
s	Frequency domain complex frequency
Std	Standard
$U.S$	United States
v_b	Output voltage [V]
v_i	Power electronics source voltage [V]
v_i^*	Power electronics source voltage reference [V]
V_n	Rated voltage [V]
v_o	Output filter voltage [V]
v_o^*	Output filter voltage reference [V]
v_{abc}	Three-Phase voltage at the PoC [V]
v_{PoC}	Voltage at the PoC [V]
VSC	Voltage source converter
X	Reactance [Ω]
Y_2	Subsystem 2 small-signal admittance [Ω^{-1}]
$Y_{jk}(s)$	Small-signal admittance with $j = \{d, q, D, Q\}$ and $k = \{d, q, D, Q\}$ referring to the respective rotating reference frame channel [Ω^{-1}]
Z_1	Subsystem 1 small-signal impedance [Ω]
z_n	Zeros of the system
Z^i_{asym}	Magnitude or phase of asymptotic limits, with i=1,2 indicating if the expression is evaluated in the minimum or maximum values, respectively
$z^{M_i}_{j,k}$	Zeros of the small-signal impedance, with $j = \{D, Q\}$ and $k = \{D, Q\}$ referring to the respective rotating reference frame channel, and $i = \{1, 2, 3\}$ indicating the corresponding model

$Z_{j,k}^{M_i}(0)$	Zero frequency value of the small-signal impedance, with $j = \{D, Q\}$ and $k = \{D, Q\}$ referring to the respective rotating reference frame channel, and $i = \{1, 2, 3\}$ indicating the corresponding model
$Z_{jk}(s)$	Small-signal impedance with $j = \{d, q, D, Q\}$ and $k = \{d, q, D, Q\}$ referring to the respective rotating reference frame channel [Ω]
Z_{M6}^{i}	Magnitude or phase of the impedance of model 6, with i=1,2 indicating if the expression is evaluated in the minimum or maximum values, respectively

Additionally, non-specified capital letters and overlines represent variables evaluated in the operating point. Furthermore, subscripts d and q indicate direct or quadrature components, respectively. In addition, dq and DQ indicate locally-referred and globally-referred rotating reference frames, respectively.

Chapter 1

Introduction

1.1. Motivation

Distributed energy resources (DER) and microgrids have become an important research focus in recent years. Microgrids are one of the key technologies to accomplish a large-scale application of distributed power generation systems, facilitating the integration of large amounts of renewable generation technologies to the main grid [1].

One of the main power supplies inside a microgrid are power electronic devices, which are responsible for energy conversion and for providing the necessary control of the microgrid itself [1]. Therefore the stability in a microgrid largely depends on the characteristics of these sources [2]. One of the desired characteristics of a microgrid is the capability to ensure beforehand its stable operation after a change in its topology due to the connection of new generation units, usually denominated 'plug & play' capability [3]. This characteristic could allow power electronic inverters in particular to be easily connected to the microgrid, without concerning about stability issues.

As the penetration of inverted-interfaced DER increases, so does the complexity of analyzing the stability of the microgrid [4]. In particular, small-signal stability has become an important issue under study in the recent years. Dynamical interactions between existing elements and newly connected renewable generation technologies affect the small-signal stability of the whole system, even if the microgrid and the new source are separately stable. A popular approach to analyze the stability and dynamical response of a particular system is its simulation through a dynamic model. Nevertheless, considering the desired 'plug & play' capability of microgrids, this approach would require to constantly model new elements whenever a new source is added to such system. Due to the complexity of this, many efforts have been made to simplify the stability analysis in microgrids with grid-feeding inverters, most commonly known as PQ inverters. Particularly, in 1976, Middlebrook introduced an impedance-based criterion for ensuring small-signal stability operation in direct current (DC) systems by first dividing the system into source and load subsystems and then applying the Nyquist criterion to the respective source/load impedances ratio [5]. This approach simplified the stability studies, allowing to assess small-signal stability by measuring these impedan-

ces at the point of connection (PoC), without the need to know each specific element of the grid. Several studies have been developed following this approach, leading to new impedance-based small-signal stability criteria for both DC systems [6, 7, 8] and alternating current (AC) systems [9, 10, 11]. Despite the aforementioned progress, the main discussion has not been focused on droop-controlled microgrids.

As mentioned in [11], droop-controlled inverters are among the most widely employed power sources in microgrids. Unlike PQ inverters, droop-controlled inverters present dynamics affecting the fundamental frequency due to the impacts of the active power droop control. This affects both the small-signal impedance and the dynamic response of the inverters. As mentioned in [12, 13], this aspect has been rarely studied. Although an additional transfer function besides the small-signal impedance is needed to ensure small-signal stability (the one related to the frequency dynamics), the study of the effects of droop-controlled inverters in the microgrid impedance is of utmost importance.

The characterization of the small-signal impedance of these inverters could lead to a better understanding about the small-signal stability and its dependency to changes in the operating conditions of the microgrid and also to changes in the parameters of the inverter controls. This characterization could lead to self-tuning elements of a microgrid, achieving the concept of "plug & play" capability, facilitating the inclusion of renewable resources to microgrids and therefore to distribution systems.

1.2. Hypothesis

This work postulates that the general behavior of the small-signal impedance of droop-controlled inverters, when facing changes in the operation conditions, can be characterized through the analysis of the small-signal impedance of linearized, reduced-order inverter models obtained by the linearization of their multi-input multi-output (MIMO) transfer functions.

1.3. Objectives

1.3.1. General Objectives

The main objective of this thesis is to characterize the small-signal impedance of droop-controlled inverters in order to achieve a comprehensive understanding of its behavior.

1.3.2. Specific Objectives

1. Review the state of art involving power inverters in microgrids and the importance of their small-signal impedance in small-signal stability studies.

2. Obtain analytical expressions describing the behavior of the small-signal impedance of simplified models of droop-controlled inverters.
3. Understand the effects on the small-signal impedance of each control subsystem of the inverter.
4. Contrast the obtained analytical expressions of the reduced-order models with the resulting small-signal impedances of more complex models through a sensitivity analysis for each critical variable considering a real case study.

1.4. Scope

As this thesis aims to characterize the general behavior of the small-signal impedance by contrasting analytical expressions obtained from simplified models with the impedance of more complex models, the results are not expected to exactly match the small-signal impedance curves of a real, full featured converter, but to give an intuition about which operation parameters have more significant impact on the impedance.

Chapter 2

Theorical Background

2.1. Microgrids

2.1.1. Definition

The microgrid concept was first mentioned in 2001 by Lasseter [14] and introduced again in 2002 [15]. It was described as a cluster of loads and micro-sources operating as a single controllable system that provides both power and heat to its local area, being electrically isolated from the main system. Subsequently, the microgrid concept has evolved, according to several characteristics assigned to them.

The IEEE Std 1547.4-2011 Standart define microgrids as all intentional island systems that could include local and/or area electric power system (EPS). They are described as EPSs that: (1) have distributed resources and loads, (2) have the ability to disconnect from and parallel with the area EPS, (3) include the local EPS and may include portions of the area EPS, and (4) are intentionally planned [16].

For its part, the U.S Department of Energy has defined the microgrids as "group of interconnected loads and DER within clearly defined electrical boundaries that acts as a single controllable entity with respect to the grid, that can connect and disconnect from the grid to enable it to operate in both grid-connected or island-mode"[17].

Although definition of microgrid is not completely unified, it is generally recognized that a microgrid is a power electric system that satisfies the following aspects [18]:

1. It is made up of a variety of DER, distributed storage devices, loads, supervisory control, and protection systems.
2. It is flexible and dispatchable, namely, it could operate in grid-connected or stand-alone mode and could switch between the two modes seamlessly by using static switches.
3. It can provide both thermal and electrical energy to consumers via cooperation of related devices.

4. The capacity of a microgrid is generally between kilowatts and megawatts.
5. It is interconnected to low or middle level distribution networks.

Unique characteristics that differentiate microgrids with large-scale traditional grids are presented in [19] and listed below.

1. Smaller system size.
2. Higher penetration of renewable energy sources (RES).
3. Higher uncertainty in the system.
4. Lower system inertia.
5. Higher R/X ratio of the feeders (medium and low voltage systems is, respectively, 0.85 and 0.77 in medium and low voltage systems, respectively [20]).
6. Low short-circuit capacities.
7. Unbalanced three-phase loading.
8. Plug & play capability.

The main power supplies inside the microgrid are power electronic devices which are responsible for energy conversion and provide the necessary control [1]. A microgrid is mostly composed by locally controlled and low sized (<100 kW) energy sources, that are connected in the near of loads through power electronic interfaces such as inverters. Power electronics provide the control and flexibility required by the microgrids concept. Correctly designed power electronics and controls insure that the microgrid can meet its customers as well as the utilities needs [15]. Microgrid have also storage system in order to respond immediately to operation problems as blackouts and stability issues. Given the weak ability of microgrids to bear disturbances, storage systems are a key issue in order to maintain the stable operation of the system and stabilize the fluctuation of renewable energy. There are different storage technologies, but batteries are the best option for microgrids due to its easy installment and manufacture [1]. Batteries are typically connected to the grid through droop-controlled inverters, known as grid-supporting inverters, as will be specified in next section. As the main power supplies inside the microgrid are power electronic devices, the inertia of the system is less than traditional systems. The dynamics of the microgrid largely depends on these power electronics and their dynamical characteristics.

As stated previously, a microgrid can operate in both (1) grid-connected or (2) stand-alone mode [21]. In grid-connected mode, most of the system-level dynamics are dictated by the main grid due to the relatively small size of the sources. In the stand-alone mode, the microgrid operates disconnected from the utility grid. In this mode, the system dynamics are dictated by the main sources themselves, their power regulation control and, to an unusual degree, by the network itself [22].

Disconnection of the microgrid from the host grid, can be either intentional (scheduled) or unintentional. Intentional islanding can occur in situations such as scheduled maintenance, or when degraded power quality of the host grid can endanger microgrid operation. Unintentional islanding can occur due to faults and other unscheduled events that are unknown to the microgrid; proper detection of such a disconnection is imperative for safety of personnel, proper operation of the microgrid, and implementation of changes required in the control

strategy [23].

Microgrid can also be presented in AC and DC configurations. The most appropriate configuration will depend on the context and can be selected based on economic, technical, and environmental criteria [21].

2.2. Inverter Characterization

2.2.1. Classification of Power Converters in AC Microgrids

As stated in Section 1.1, the main elements that compose a microgrid are the power converters. In AC microgrids, there has been identified mainly 3 different types of inverters, from the viewpoint of the control loops system: (1) Grid-forming inverters, (2) grid-supporting inverters, and (3) grid-feeding inverters [24].

Grid forming converters can be represented as an ideal voltage source with small output impedance, where reference voltage E^* and frequency ω^* are fixed by the rated operation conditions of the grid.

On the other hand, grid-feeding inverters are designed to supply electric power to an already operating grid. These inverters can be represented by a current source with high output impedance. Output active power P^* and reactive power Q^* are fixed by an adequate controller, by synchronizing the current source appropriately using a phase-locked loop (PLL). Voltage measurement of the PoC is also required. It is important to remark that grid-feeding inverters cannot operate independently.

Finally, grid-supporting inverters can be represented by a voltage source in series with the output impedance, or by a current source in parallel with the output impedance. These inverters regulate both the output voltage and frequency, by controlling the active and reactive power delivered to the grid by a droop controller, thus helping to maintain the operation variables near their nominal value.

Figure 2.1 shows simplified representations of the above-mentioned inverter configurations, emphasizing the controlled variables in each case. Specific control details associated to each inverter configuration are discussed below in detail.

1. **Grid-forming Converters:** As grid-forming inverters fix the voltage and the frequency at the PoC, it is required a perfect synchronization to operate more than one grid-forming converter in parallel, considering its small output impedance. Its internal control scheme is displayed in Figure 2.2.

   Two cascaded PI loop controls, referenced in the rotating dq reference frames, compose the control of grid-forming converters. The first external loop corresponds to the voltage controller, which controls the output voltage in order to match the reference voltage E^*. The internal loop, on the other hand, corresponds to the current controller, which regulates the current supplied by the power electronics source. Thus, the current

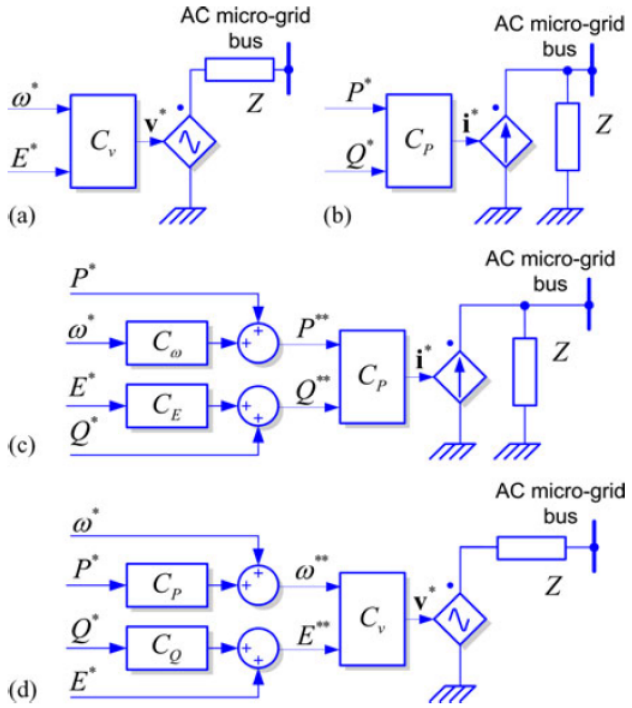

Figure 2.1: Simplified representation of grid-connected power inverters. (a) grid-forming, (b) grid-feeding, (c) grid-supporting as current source, and (d) grid-supporting as voltage source [24].

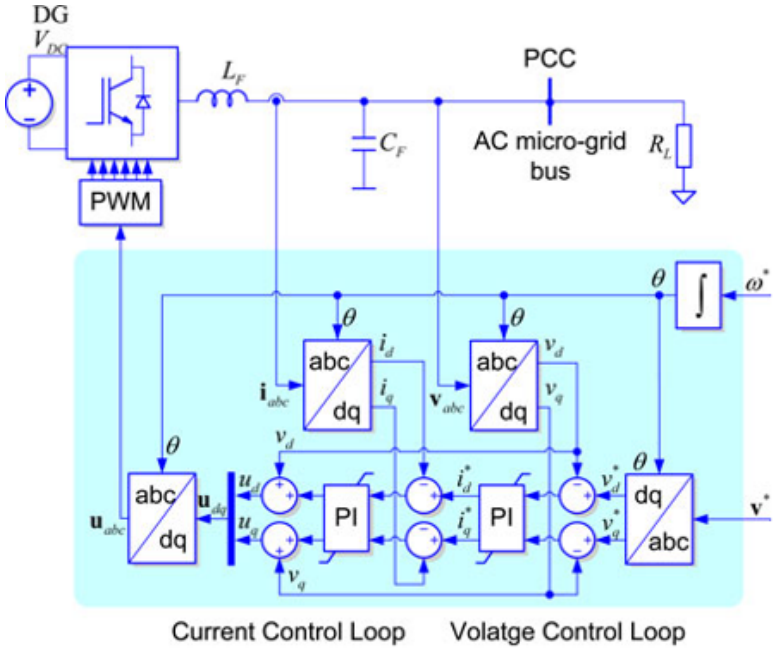

Figure 2.2: Internal control of the grid-forming converter [24].

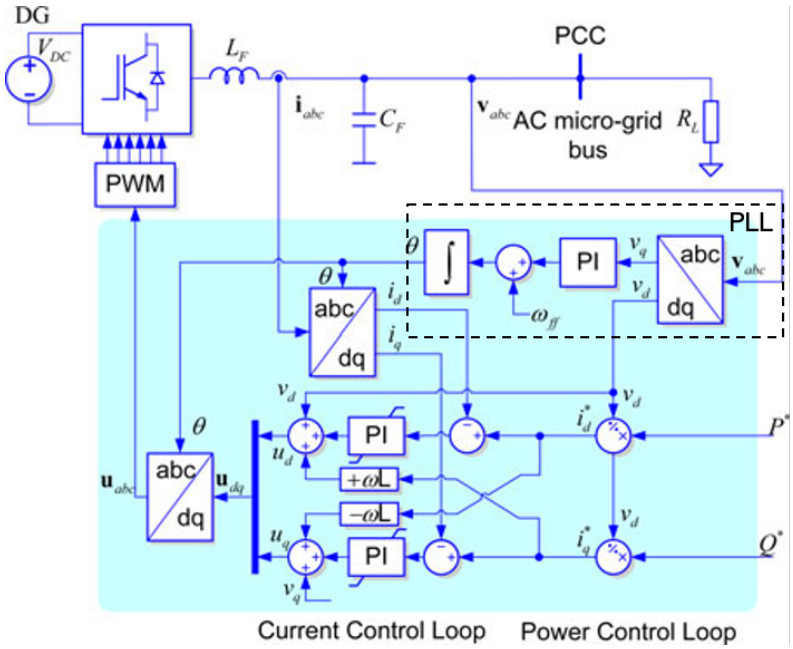

Figure 2.3: Internal Control of the Grid-Feeding Converter [24].

through L_F charges the C_F capacitor, maintaining the voltage in the PoC near the given reference.

2. **Grid-feeding Converters:** As stated previously, grid-feeding (or grid-following) converters are controlled as high impedance parallel current sources. Unlike grid-forming converters, they can operate in parallel multi-converter systems, injecting power to the grid according to specified references values. Although they can be controlled in order to participate in the voltage and frequency regulation of the microgrid, they are typically controlled by maximum power point tracking systems. The basic control scheme of these converters is shown in Figure 2.3.

   A PLL is used to obtain the rotating angle θ of the voltage in the PoC v_{abc}, used in the internal control loops. Two input power references P^* and Q^* are divided by the direct reference frame of the voltage in the PoC, obtaining a reference current for each dq channel. The internal current control loop regulates the current through the L_F inductance, charging the C_F capacitor, hence maintaining the voltage near the appropriate values.

3. **Grid-supporting Converters:** The main objective of these converters is the participation in the voltage and frequency regulation. Unlike grid-forming converters, and despite having similar closed control loops, grid-supporting converters are able to participate directly in the regulation through an adequate control, as shown in Figure 2.4.

   As mentioned earlier, two main types of power converters can be found within the grid-supporting group: (a) current-controlled inverters and (b) voltage-controlled inverters.

   (a) **Current-controlled Inverter:** The objective of the current source-controlled inverter is to not only supply the load connected to the grid, but also to additionally contribute in the voltage amplitude and frequency regulation of the microgrid. In this case, reference parameters are given as inputs, as shown in Figure 2.4 (a), whi-

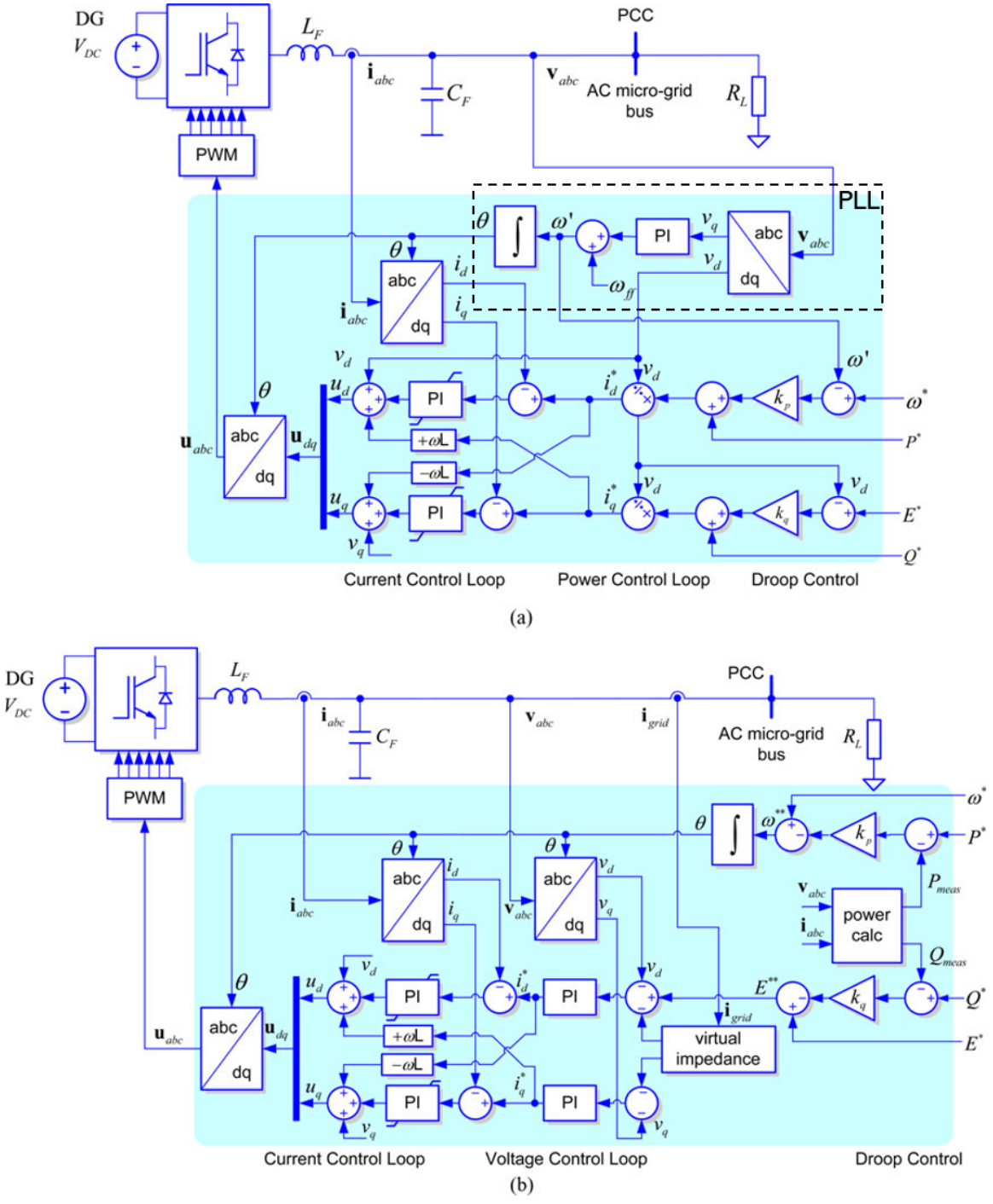

Figure 2.4: Basic control structure of three-phase grid-supporting power converters. (a) Grid-supporting power converter controlled as a current source. (b) Grid-supporting power converter controlled as a voltage source [24].

le a PLL is used to obtain the rotating angle θ and the frequency ω of the voltage in the PoC v_{abc}, used in the internal control loops. This droop control gives the input voltage to the power control block, where algebraic operations are performed and current set points are obtained. Finally, in the current control loop, two PI controllers, one for each dq axis, are used, in order to obtain the modulating voltage references [24].

(b) **Voltage-controlled Inverter:** The voltage source-controlled inverters presented in Figure 2.4 (b) emulate the behavior of AC voltage sources, connected through a coupling impedance. In this case, the traditional droop control, presented in Section 2.2.2 is used in order to obtain the input references of the voltage control loop. No measuring PLL is needed in this configuration, as the droop control gives the reference rotating angle θ to the voltage control loop. PI controllers for each dq axis set the current references given to the internal current control loop. Similar as in the current source-controlled inverter, the current control loop uses two PI controllers in order to obtain the modulating voltage references. This kind of converters can participate in the voltage and frequency regulation in both grid-connected and stand-alone modes, with no need of connecting any grid-forming converter to the microgrid [24].

2.2.2. Droop-controlled Inverter Modelling

In this section, a detailed model of a droop-controlled is presented, assuming a grid-supporting inverter. The full schematic model is presented in Figure 2.5 [25], where every block, including the actuator controller, is presented in dq reference frame.

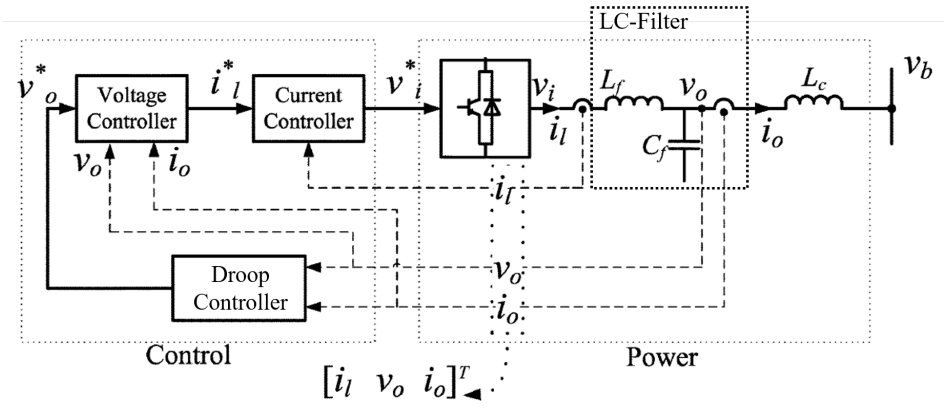

Figure 2.5: Droop-controlled Inverter Control Subsystems [26].

Droop Controller

The traditional droop control in microgrids, used to share the demanded electric power between parallel inverters in order to avoid instabilities, is graphically presented in Figure 2.6.

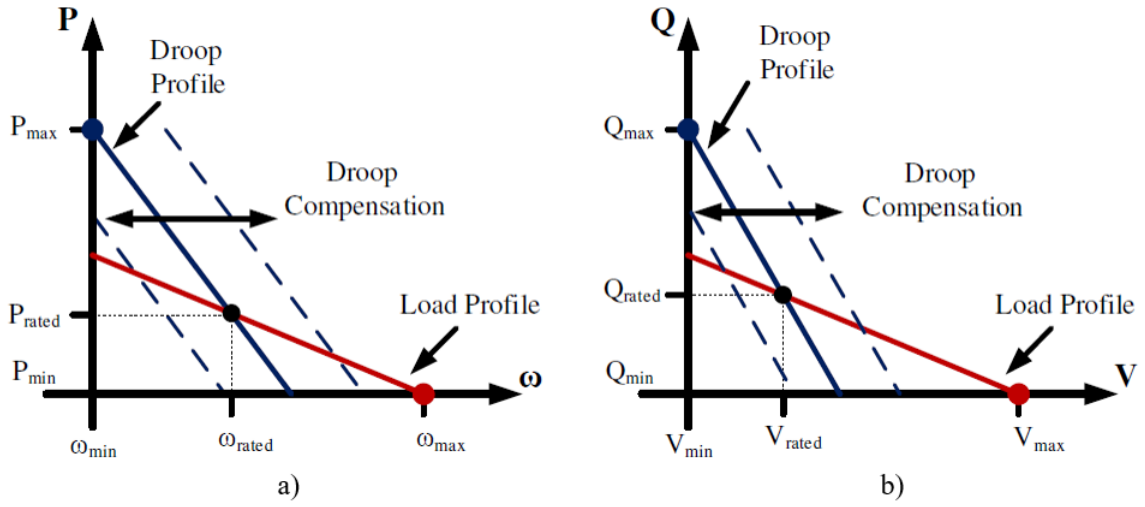

Figure 2.6: Conventional Droop Control Applied in Microgrids [27].

This control is based on the traditional synchronous machines droop control. Despite the assumption of small R/X ratio, which is not fully met in low voltage grids, it is still used in most microgrids due to its simplicity [28].

As stated in Section 2.2.1, droop-controlled inverters determine the frequency and voltage set point to ensure correct real and reactive power sharing between the parallel connected inverters, in response to load changes. The frequency set point is thus made to decrease with increasing real power supplied by the inverter, as described by the $P - \omega$ droop characteristic presented in Figure 2.6 a). In a similar manner, the set points for the voltages can be determined from the $Q - V$ droop characteristics, as described in Figure 2.6 b) [29].

The set points values are calculated as in (2.1) and (2.2). Note that the reference voltage is aligned with the direct axis of the coupling filter capacitor, in the local rotating reference frame dq, as stated in (2.2).

$$\omega^* = \omega_n - m_p \left(P - P_n\right), \quad \dot{\theta} = \omega \tag{2.1}$$

$$v_{od}^* = V_n - n_p Q, \quad v_{oq}^* = 0 \tag{2.2}$$

Where ω^* and v_{od}^* correspond to the calculated frequency and direct voltage set points. ω_n and V_n are the frequency and voltage nominal values. P and Q correspond to the measured active and reactive power. Finally, m_p and n_q are the droop slopes that determine the relative power sharing between the inverters. Note that no communication system is needed in order to define the set points values.

The droop gains m_p and n_q are tuned according to the expected frequency and voltage range of values, as shown in (2.3):

$$m_p = \frac{\omega_{max} - \omega_{min}}{P_{max}}, \quad n_q = \frac{V_{odmax} - V_{odmin}}{Q_{max}} \tag{2.3}$$

In order to obtain the output power, output currents and voltages are measured. Expressing the values in local dq rotating reference, considering a three-phase system, the output powers are obtained as follows:

$$p = v_{od} i_{od} + v_{oq} i_{oq}, \quad q = v_{od} i_{oq} + v_{oq} i_{od} \tag{2.4}$$

These measured powers are passed through a low-pass filter with low cut-off frequency, achieving a good attenuation of high distortion frequency components, thus avoiding any interaction with the internal current controls. Thus, by considering the typical low-pass filter equations, two state variables are introduced as inputs to the droop controller block.

$$\dot{P} = \omega_c \left(p - P\right) \tag{2.5}$$

$$\dot{Q} = \omega_c \left(q - Q\right) \tag{2.6}$$

Subsequently, the droop control is performed, obtaining the frequency and voltage reference set points. In order to be used in the rotating reference frame transformations, the reference frequency is integrated, obtaining a reference phase angle.

To sum up, the complete droop control scheme is shown in Figure 2.7.

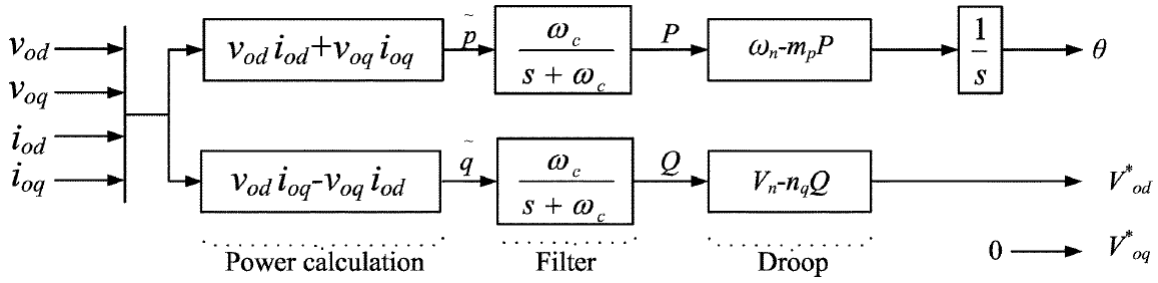

Figure 2.7: Droop Controller Structure [26].

Voltage Controller

Figure 2.8 shows the voltage controller block diagram including all feed-back and feed-forward terms. The control is achieved with a standard PI controller for each dq axis.

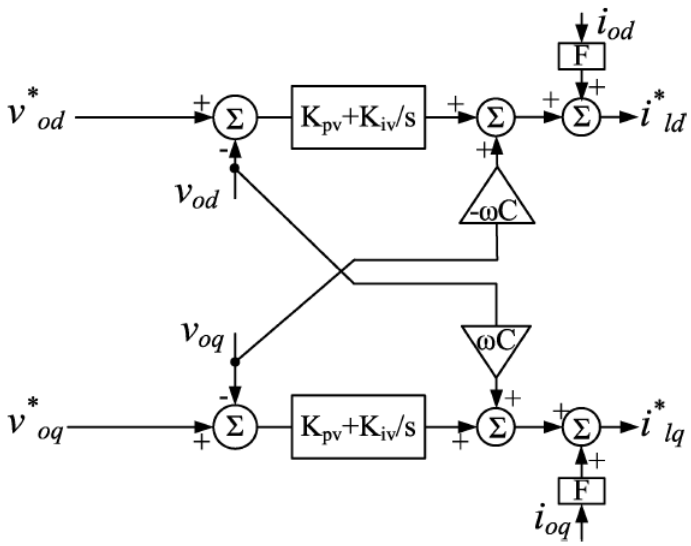

Figure 2.8: Voltage Controller Structure [26].

PI controllers maintain the LC filter output voltage in the reference value given by the droop controller, by setting the current set points of the internal current controller. Each PI controller introduces a differential equation, corresponding to two more state variables.

The mathematical model is presented in (2.7) and (2.8).

$$\frac{\phi_d}{dt} = v^*_{od} - v_{od}, \quad \frac{\phi_q}{dt} = v^*_{oq} - v_{oq} \tag{2.7}$$

$$\begin{aligned} i^*_{ld} &= Fi_{od} - \omega_n C_f v_{oq} + K_{pv}\left(v^*_{od} - v_{od}\right) + K_{iv}\phi_d \\ i^*_{lq} &= Fi_{oq} + \omega_n C_f v_{od} + K_{pv}\left(v^*_{oq} - v_{oq}\right) + K_{iv}\phi_q \end{aligned} \tag{2.8}$$

Current Controller

Figure 2.9 shows the current controller structure. As in the voltage controller, this controller is composed by a PI block for each dq axis.

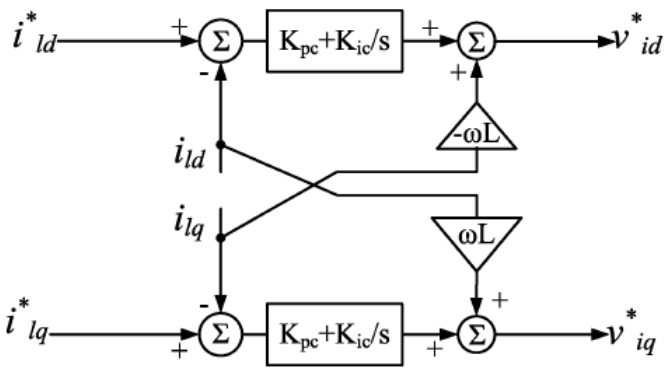

Figure 2.9: Current Controller Structure [26].

In this case, the PI controllers maintain the output current of the inductance L_f in the reference values given by the voltage controller. Thus, the reference voltage values are acquired, being modulated by the power electronics actuator.

The corresponding differential equations and algebraic expressions are presented in (2.9) and (2.10).

$$\frac{\gamma_d}{dt} = i_{ld}^* - i_{ld}, \quad \frac{\gamma_q}{dt} = i_{lq}^* - i_{lq} \tag{2.9}$$

$$\begin{aligned} v_{id}^* &= v_{od} - \omega_n L_f i_{lq} + K_{pc}\left(i_{ld}^* - i_{ld}\right) + K_{ic}\gamma_d \\ v_{iq}^* &= v_{oq} + \omega_n L_f i_{ld} + K_{pc}\left(i_{lq}^* - i_{lq}\right) + K_{ic}\gamma_q \end{aligned} \tag{2.10}$$

Output LC filter and Coupling Inductance

If $v_i = v_i^*$ is assumed, this is, assuming an ideal-modulated voltage source, the output LC filter and the coupling inductance models can be described with the following differential equations, representing the state-space equations of the physical inverter construction [26].

$$
\begin{aligned}
\frac{di_{ld}}{dt} &= \frac{-r_f}{L_f} i_{ld} + \omega i_{lq} + \frac{1}{L_f} v_{id} - \frac{1}{L_f} v_{od} \\
\frac{di_{lq}}{dt} &= \frac{-r_f}{L_f} i_{lq} - \omega i_{ld} + \frac{1}{L_f} v_{iq} - \frac{1}{L_f} v_{oq} \\
\frac{dv_{od}}{dt} &= \omega v_{oq} + \frac{1}{C_f} i_{ld} - \frac{1}{C_f} i_{od} \\
\frac{dv_{oq}}{dt} &= -\omega v_{od} + \frac{1}{C_f} i_{lq} - \frac{1}{C_f} i_{oq} \\
\frac{di_{od}}{dt} &= \frac{-r_c}{L_c} i_{od} + \omega i_{oq} + \frac{1}{L_c} v_{od} - \frac{1}{L_c} v_{bd} \\
\frac{di_{oq}}{dt} &= \frac{-r_c}{L_c} i_{oq} - \omega i_{od} + \frac{1}{L_c} v_{oq} - \frac{1}{L_c} v_{bq}
\end{aligned}
\tag{2.11}
$$

Reference Frame Transformation

The presented inverter model was modelled in a local dq reference frame. In order to connect the inverter to a whole system, the output variables need to be converted to a global DQ reference frame, as presented in Figure 2.10:

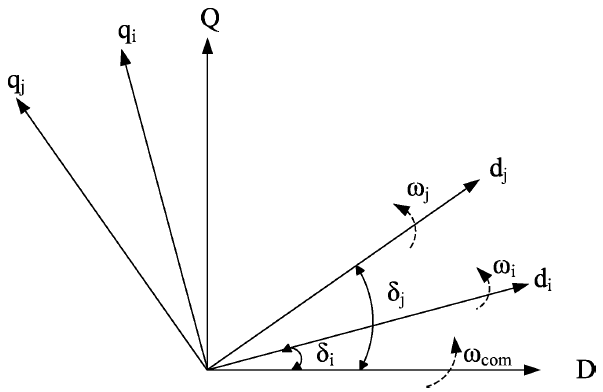

Figure 2.10: Reference Frame Transformation [25].

Three different rotating axes are presented. $(D-Q)$ is the global (or common) reference frame, $(d-q)_i$ is the reference frame of the ith inverter, rotating at ω_i and $(d-q)_j$ is the reference frame of the jth inverter, rotating at ω_j.

With the aim of translating the inverters to the common reference frame, the transformation technique defined in (2.12) is used [25].

$$
\begin{bmatrix} f_D \\ f_Q \end{bmatrix} = \begin{bmatrix} \cos(\delta_i) & -\sin(\delta_i) \\ \sin(\delta_i) & \cos(\delta_i) \end{bmatrix} \cdot \begin{bmatrix} f_d \\ f_q \end{bmatrix} \tag{2.12}
$$

Note that δ_i is the angle of the reference frame of ith inverter with respect to the common reference frame, as presented in (2.13),

$$\delta_i = \int (\omega_i - \omega_{com}) \, \mathrm{d}t \tag{2.13}$$

where ω_i and ω_{com} are the rotation frequency of the ith inverter reference frame and the common reference frame, respectively. If (2.13) is derived, the following differential equation can be obtained:

$$\dot{\delta} = \omega - \omega_{com} \tag{2.14}$$

Steady-State Operation

In steady-state operation, Kirchhoff algebraic relationships between the different electrical variables can be obtained by evaluating in a static operating point, as all the derivatives are zero:

$$\begin{aligned}
0 &= -\frac{r_f}{L_f} I_{ld} + \overline{\omega} I_{lq} + \frac{1}{L_f} V_{id} - \frac{1}{L_f} V_{od} \\
0 &= -\frac{r_f}{L_f} I_{lq} - \overline{\omega} I_{ld} + \frac{1}{L_f} V_{iq} - \frac{1}{L_f} V_{oq} \\
0 &= \overline{\omega} V_{oq} + \frac{1}{C_f} I_{ld} - \frac{1}{C_f} I_{od} \\
0 &= -\overline{\omega} V_{od} + \frac{1}{C_f} I_{lq} - \frac{1}{C_f} I_{oq} \\
0 &= -\frac{r_c}{L_c} I_{od} + \overline{\omega} I_{oq} + \frac{1}{L_c} V_{od} - \frac{1}{L_c} V_{bd} \\
0 &= -\frac{r_c}{L_c} I_{oq} - \overline{\omega} I_{od} + \frac{1}{L_c} V_{oq} - \frac{1}{L_c} V_{bq}
\end{aligned} \tag{2.15}$$

where the overlines and the capital letters represent variables evaluated in the operating point.

Additionally, in the rotating reference frames the d axis is typically aligned with the defined reference voltage. Considering this, in steady-state regime, the voltage phase corresponds to the angle of the reference frame with respect to the common reference frame.

If the global reference steady-state operating points values of the LCL electric system are known, then the global phase angle of the V_o voltage of the inverter can also be obtained.

Thus, as in the local reference frame the phase angle of the V_o voltage is defined as zero

by the droop control, then δ can be obtained as the global V_o phase angle, as presented in (2.16).

$$\begin{aligned} \overline{\delta} &= \underline{\angle V_o^g} - \underline{\angle V_o^l} \\ \Rightarrow \overline{\delta} &= \underline{\angle V_o^g} - 0 \\ \Rightarrow \overline{\delta} &= \underline{\angle V_o^g} \\ \Rightarrow \overline{\delta} &= \arctan\left(\frac{V_{oQ}}{V_{oD}}\right) \end{aligned} \tag{2.16}$$

2.3. Stability in Microgrids

As established in [30], stability of an EPS is defined as the capability of the system to remain in a certain operating equilibrium under normal operating conditions and to regain an acceptable operating point after being subjected to a disturbance. It represent a balance of opposing forces. The response of the system depends directly on the nature and magnitude of the perturbation.

Microgrids facilitate the effective integration of DER via power electronics interfaces (e.g. inverter or converter) [31], therefore the stability in a microgrid largely depends on the characteristics of the sources, as stated in Section 1.1.

Due to the aforementioned systemic differences between traditional power systems and microgrids, there is a need to redefine the categorization of power systems stability in order to be applied in microgrids, properly reflecting relevant stability issues in this type of systems. For example, maintaining frequency stability in microgrids is more challenging than in traditional power systems due to the low system inertia and high penetration of renewable energy sources. Moreover, transient and voltage stability are more common in larger grids than microgrids [19].

Stability problems in microgrids are classified in two categorizes by addressing the most recurrent issues: (1) Control System Stability and (2) Power Supply and Balance Stability, as indicated in Figure 2.11.

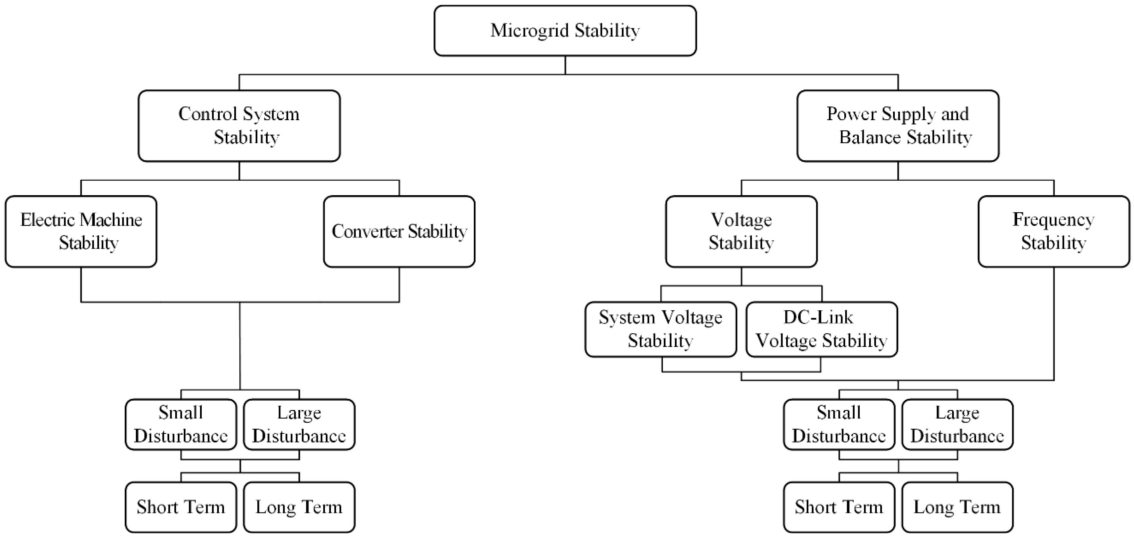

Figure 2.11: Stability in Microgrids [19].

2.3.1. Control System Stability [19]

Control system stability problems are related to inadequate control schemes or poor tuning of equipment controllers in both electric machines and inverters. Until the destabilizing element is disconnected or re-tuned, the whole system cannot be stabilized. This stability category can be subcategorized as follows:

1. **Electric Machine Stability** In the traditional systems, electric machines instability is caused by the lack of synchronizing torque or inadequate damping torque. Considering also that in resistive lines synchronous machines are likely to decelerate during short-circuits, it is concluded that this type of stability issues are associated mostly with poor tuning of the exciters and governors of the synchronous machines in the microgrid.

2. **Converter Stability** As microgrids are composed by large amount of inverters and power electronic devices, instability caused by inverters is an important issue to be considered. There are three main causes regarding this matter: (1) Inner Current and Voltage Control Loops, (2) LCL Output Filters and (3) PLL-based Synchronization Strategies. Inner control loops, contrary to low-frequency oscillations caused by outer power controls, may cause high harmonic-frequency oscillations, in the range of hundreds of Hz to several kHz. High-frequency instability can also be caused by the LCL filter resonance, triggered by the high-frequency switching, by the control of the inverter itself or by interactions with controllers nearby. Damping strategies can prevent these high-frequency instabilities. PLL-triggered instability is caused by the changes produced by the PLL in the impedance of the grid, and depends on the PLL bandwidth.

2.3.2. Power Supply and Balance Stability [19]

Stability issues in traditional grids are also presented in microgrids, but some essential system differences implies to redefine the mitigation strategies. Therefore specific descriptions for microgrids are presented next.

1. **Frequency Stability** As microgrids have low system inertia, due to the small number of rotating machines and high share of renewable energy sources, frequency stability is a major concern. Frequency regulation is complicated by the high R/X ratio of the distribution feeders, thus coupling voltage and frequency, invalidating traditional regulation techniques. There are several reasons for frequency instability in microgrids, as (1) large load increases, considering the low system inertia, (2) poor coordination of frequency and power controllers that may trigger undamped frequency oscillations and (3) insufficient generation reserve, activating under-frequency load tripping in the steady-state regime.
2. **Voltage Stability** As lines in microgrids are short, the transferred power between generation and loads is not limited as in traditional systems, resulting in relatively small voltage drops. Nevertheless, there are other factors that may imply unacceptable voltages. As feeders in microgrids are short, any change in DER are reflected in the rest of the system, yielding high circulating reactive power flows if not properly coordinated, and thus resulting in large voltage oscillations. Power droop control is frequently used to achieve a proper power sharing strategy, as will stated in Section 2.2. If not properly used, in some cases this strategy fails to achieve the desired reactive power sharing, causing severe voltage deviations and in worst cases, voltage instabilities. Another type of voltage stability pertains to the ability of DER based on voltage source converters to maintain the voltage across the dc-link capacitor. Situations may occur where the active power demand may result in undamped ripples in the dc-link voltage capacitor, resulting in large fluctuations on power injections of the source.

As illustrated in Figure 2.11, the period of interest in stability studies can be short or long, depending on the specific analyzed phenomenon. Also, a differentiation can be made between large and small perturbations. Small perturbations in particular are the ones involved in small-signal stability assessments. Small-signal stability is defined as the capability of the electric system to maintain a certain operating point before these perturbations. For more details see Section 2.4.

It is important to note that there is not a complete decoupling between the different types of stability, and a system can be unstable both by control system stability or power supply and balance stability. A voltage perturbation, for example, can unleash electric machine or frequency instabilities.

2.4. Small-Signal Stability

Besides the factors involved in microgrid instabilities presented in previous section, small-signal stability in microgrids is primarily affected by controllers feedback (it has been proved

that droop control affect significantly the microgrid stability [32]). Other factors as small load changes, the damping factor of the system and power limits in DER, are also important. In order to enhance the stability of the system, it is needed to control the critical parameters such as the droop gains, the connection impedance value, the X/R ratio, among others.

The small signal stability in a microgrid can be analyzed with a linearized model around the operating point [2], hence a representation of the grid as a state-space model can be developed considering small perturbations.

2.4.1. State-Space Representation

Systems can be represented as state-space models, expressing them as follows:

$$\dot{x} = f\left(x, u, t\right) \tag{2.17}$$

where $x = \begin{bmatrix} x_1 \dots x_n \end{bmatrix}^T$, $u = \begin{bmatrix} u_1 \dots u_n \end{bmatrix}^T$ and $f = \begin{bmatrix} f_1 \dots f_n \end{bmatrix}^T$.

Moreover, vector x represents every state variables x_i of the system and u corresponds to the entries vector with u_i being the ith-entry of the system.

An output vector is also defined, expressed as function of states and entries:

$$y = g(x, u) \tag{2.18}$$

where $y = \begin{bmatrix} y_1 \dots y_n \end{bmatrix}^T$ and $g = \begin{bmatrix} g_1 \dots g_n \end{bmatrix}^T$

2.4.2. State-Space Linearization

Considering a small deviation in states Δx and entries Δu, the system is linearized, resulting from (2.17) and (2.18) in:

$$\Delta\dot{x} = A\Delta x + B\Delta u \tag{2.19}$$

$$\Delta y = C\Delta x + D\Delta u \tag{2.20}$$

where

$$A = \begin{bmatrix} \frac{\partial f_1}{\partial x_1} & \cdots & \frac{\partial f_1}{\partial x_n} \\ \cdots & \cdots & \cdots \\ \frac{\partial f_n}{\partial x_1} & \cdots & \frac{\partial f_n}{\partial x_n} \end{bmatrix} \quad B = \begin{bmatrix} \frac{\partial f_1}{\partial u_1} & \cdots & \frac{\partial f_1}{\partial u_r} \\ \cdots & \cdots & \cdots \\ \frac{\partial f_n}{\partial u_1} & \cdots & \frac{\partial f_n}{\partial u_r} \end{bmatrix}$$
$$C = \begin{bmatrix} \frac{\partial g_1}{\partial x_1} & \cdots & \frac{\partial g_1}{\partial x_n} \\ \cdots & \cdots & \cdots \\ \frac{\partial g_m}{\partial x_1} & \cdots & \frac{\partial g_m}{\partial x_n} \end{bmatrix} \quad D = \begin{bmatrix} \frac{\partial g_1}{\partial u_1} & \cdots & \frac{\partial g_1}{\partial u_r} \\ \cdots & \cdots & \cdots \\ \frac{\partial g_m}{\partial u_1} & \cdots & \frac{\partial g_m}{\partial u_r} \end{bmatrix} \tag{2.21}$$

Partial derivatives in matrices A, B, C and D are evaluated in the operation point x_0.

In (2.19) and (2.20):

Δx is the state vector of the linearized system, of dimension n
Δy is the output vector of dimension m
Δu is the input vector of dimension r
A is the system matrix, of dimension $n \times n$
B is the control matrix, of dimension $n \times r$
C is the output matrix, of dimension $m \times n$
D is the feed-forward matrix, of dimension $m \times r$

It is important to notice that, in small-signal studies, some elements are not linearizable, e.g. tap-changing controllers in transformers, therefore their effects will not be reflected adequately in the results. In order to improve the representativeness in this cases, mixed small and large signal studies are carried out [30].

By applying Laplace transform to (2.19) and (2.20) and rearranging, the following pair of frequency-space linearized equations can be obtained:

$$\begin{aligned} \Delta x(s) &= (sI - A)^{-1} [\Delta x(0) + B\Delta u(s)] \\ \Delta y(s) &= C\Delta x(s) + D\Delta u(s) \end{aligned} \tag{2.22}$$

Starting with (2.22), the characteristic polynomial can be obtained, whose roots correspond to the poles of the system:

$$det|sI - A| = 0 \tag{2.23}$$

2.4.3. Small-Signal Analysis

The small-signal stability analysis of an equilibrium point is done studying the stability of the corresponding linearized system in the vicinity of the equilibrium point. The principal methods of analyzing linearized transfer function and ensuring small-signal stability in power electric systems are listed and described bellow.

1. **Bode Diagram Analysis:** A Bode diagram consist of two graphs: (1) A plot of the logarithm of the magnitude of a sinusoidal transfer function, where the unit used in this representation is the decibel and (2) a plot of the phase angle. Both are plotted against the frequency on a logarithmic scale [33]. These diagrams represent the frequency response. The main advantage of these diagrams is the availability of a simple method for sketching an approximate log-magnitude curve, based on asymptotic approximations.

   The construction of the approximated Bode diagrams depends basically of three parameters:

   (a) **Zero Frequency Value:** Corresponds to the transfer function value when $s = 0$. It determines the systems response when a DC perturbation is applied.

   (b) **Poles:** By solving (2.23), the poles of the system can be obtained, this is, the frequencies for which the value of the denominator of the transfer function becomes zero.

   (c) **Zeros:** Similar as poles, zeros correspond to the frequencies for which the value of the nominator of the transfer function becomes zero.

   Considering the transfer function presented in 2.24, the magnitude and phase angle asymptotic graphs construction are summarized below:

$$H(s) = A \prod \frac{(s - z_n)^{a_n}}{(s - p_n)^{b_n}} \tag{2.24}$$

   (a) **Magnitude Plot:**

      i. Although it is not possible to plot curves down to zero frequency because of the logarithmic frequency ($log(0) = -\infty$), this does not create a serious problem, as limit approximations can be made. Hence, the initial value of graph is approximately $\mid H(0) \mid_{dB}$.

      ii. At every zero z_n of the system, increase the slope of the line by $20 \cdot a_n$ dB per decade.

      iii. At every pole p_n of the system, decrease the slope of the line by $20 \cdot b_n$ dB per decade.

      iv. As complex conjugates zeros or poles equations can be written as $(s - \omega_R + j\sigma)(s - \omega_R - j\sigma) = s^2 - 2\omega_R s + \sigma^2 + \omega_R^2 = s^2 + 2\xi\omega_n s + \omega_n^2$, the critical slope-changing frequency corresponds to the natural frequency ω_n of the corresponding poles or zeros pair.

      v. The damping factor can be determined as $\xi = -\omega_R/\omega_n$, which determines the peak magnitude (in the case of poles) and negative peak magnitude (in the case of zeros), if $\xi < 0,707$, as presented in Figure 2.12.

   (b) **Phase Angle:** To draw the phase plot for each pole and zero, the following rules have been developed.

      i. The basis initial value of the graph is set to $0°$ if $A > 0$, and to $-180°$ if $A < 0$.

      ii. If the sum of the number of unstable (i.e. right half plane) poles and zeros is odd, add $180°$ to that basis.

      iii. At every zero z_n, increase (for stable zeros) or decrease (for unstable zeros) the slope by $45 \cdot a_n$ $^\circ$ per decade, beginning one decade before $\omega = \mid z_n \mid$

iv. At every pole p_n, increase (for stable poles) or decrease (for unstable poles) the slope by $45 \cdot b_n$ ° per decade, beginning one decade before $\omega =\mid p_n \mid$

v. When the phase has changed by $90 \cdot a_n^\circ$ (for a zero) or by $90 \cdot b_n^\circ$ (for a pole), flatten again the slope.

Once every poles and zeros have been graphed, the different lines are added together, obtaining a single final phase plot.

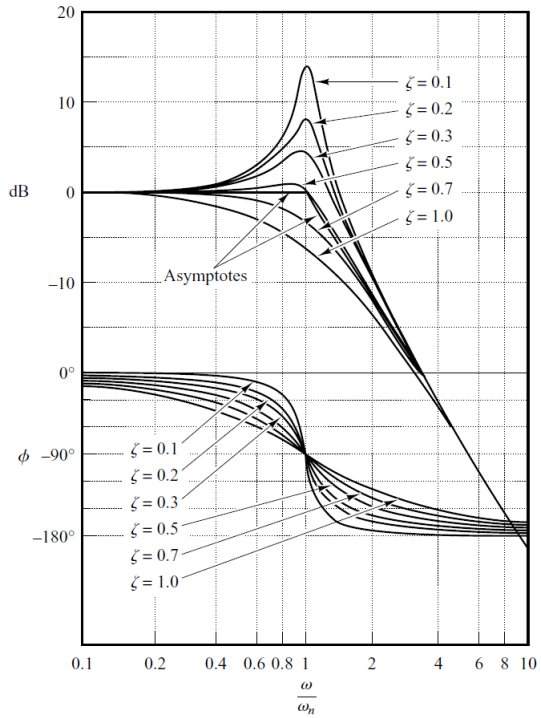

Figure 2.12: Log-magnitude curves, together with the asymptotes, and phase-angle curves of a quadratic transfer function [33].

2. **First Lyapunov Method:** The first Lyapunov method analyze the real part poles of the system, acquired from (2.23):
   (a) A linear system is asymptotically stable if and only if real parts of all poles (or eigenvalues of the system matrix) are negative.
   (b) If the real part of at least a single pole is positive, the system is unstable.
   (c) A linear system is marginally stable if and only if it has at least one simple pole (not repeated) with real part zero, and all other poles have negative real parts. Therefore, a system cannot be both asymptotically stable and marginally stable.
3. **Nyquist Stability Criteria:**

   The polar diagram, also known as Nyquist diagram, of a transfer function $G(j\omega)$ is a magnitude versus phase-angle plot of $G(j\omega)$, when ω varies from 0 to ∞. In other words, the Nyquist diagram is the locus of the vectors $|G(j\omega)|\underline{/G(j\omega)}$.

   $G(j\omega)$ axis projections are their real and imaginary components, as presented in Figure 2.13.

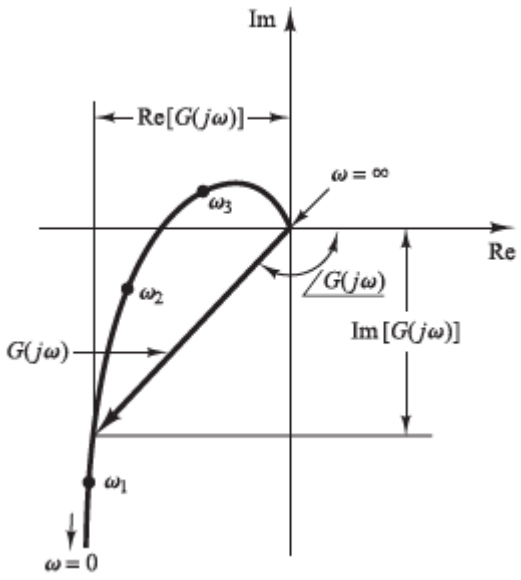

Figure 2.13: Nyquist Diagram [33].

Nyquist stability criterion determines the stability of a closed-loop system as from the open-loop frequency response and the respective system poles.

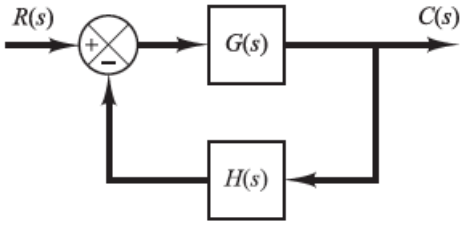

Figure 2.14: Closed-Loop System [33].

Equation (2.25) corresponds to the transfer function of the closed-loop system displayed in Figure 2.14, whereas that (2.26) represents the open-loop function.

$$F_{CL}(s) = \frac{G(s)}{1 + G(s)H(s)} \tag{2.25}$$

$$F_{OL}(s) = G(s)H(s) \tag{2.26}$$

Nyquist stability criterion, for the special case when $G(j\omega)H(j\omega)$ has neither poles nor zeros on the $j\omega$ axis, postulate that: *If the open-loop transfer function $G(j\omega)H(j\omega)$ has k poles in the right-half s plane and $\lim_{s\to\infty} G(s)H(s) = constant$, then for stability the $G(j\omega)H(j\omega)$ locus, as ω varies from $-\infty$ to ∞, must encircle the $-1+j0$ point k times in the counterclockwise direction* [33].

Remarks on the Nyquist Stability Criterion [33]:

(a) This criterion can be expressed as: $Z = N + P$, where

i. Z = number of zeros of $1 + G(s)H(s)$ in the right-half s plane.

ii. N = number of clockwise encirclements of the $-1 + j0$ point.

iii. P = number of poles of $G(s)H(s)$ in the right-half s plane.

For a stable control system, Z must be zero.

(b) For multiple-loop systems, Nyquist stability criterion is not sufficient to detect instability. Other methods, like Routh criterion can be applied in these cases.

(c) If the locus of $G(j\omega)H(j\omega)$ passes through the $-1 + j0$ point, then zeros of the characteristic equation, or closed-loop poles, are located on the $j\omega$ axis, which is not desirable for practical control systems.

For a general case when $G(j\omega)H(j\omega)$ has poles and/or zeros on the $j\omega$ axis, it is postulated that: *If the open-loop transfer function $G(j\omega)H(j\omega)$ has k poles in the right-half s plane, then for stability the $G(j\omega)H(j\omega)$ locus, as representative point s traces on the modified Nyquist path in the clockwise direction, must encircle the $-1+j0$ point k times in the counterclockwise direction* [33].

2.5. Small-Signal Stability in Microgrids

2.5.1. Small-Signal Impedance

Small-signal impedance corresponds to a transfer function that determines the output of a certain electric system, given each possible input. By defining inputs as currents and outputs as voltages, an impedance transfer function can be defined.

Considering a rotating dq reference frame, both direct and quadrature voltage and currents must be considered. Hence, a multi-input multi-output (MIMO) linearized system can be defined, as presented in (2.27)

$$\begin{bmatrix} \Delta v_d \\ \Delta v_q \end{bmatrix} = \begin{bmatrix} Z_{dd}(s) & Z_{dq}(s) \\ Z_{qd}(s) & Z_{qq}(s) \end{bmatrix} \cdot \begin{bmatrix} \Delta i_d \\ \Delta i_q \end{bmatrix} \tag{2.27}$$

where Z_{jk} is the linearized transfer function relating output v_k with perturbations in input i_j, with $j = d, q$ and $k = d, q$

As small-signal impedance can be seen as a transfer function, a bode plot can be graphed for each dq-channel, in order to characterize its frequency response shape.

2.5.2. Small-Signal Stability Criteria

Small-signal stability was previously defined as the capability to maintain an operating point when facing small perturbations. As stated in the previous section, the Nyquist criteria has been widely used to determine stability against small-signal perturbations in microgrids

connected to newly added sources. By splitting the system at the PoC, two subsystem can be defined, as presented in Figure 2.15.

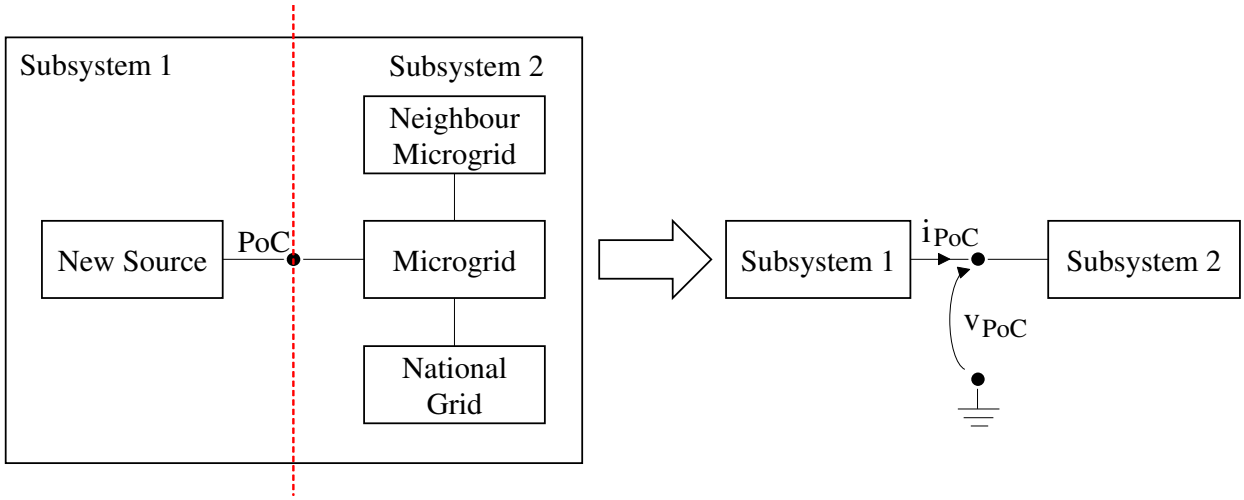

Figure 2.15: Conceptual Microgrid Split into Source and Load Subsystems [3].

Subsystem 1 (also known as the source subsystem) corresponds to the source itself. Furthermore, subsystem 2 (also known as the load subsystem) correspond to the rest of the system, involving the microgrid and other connected elements as for example a neighbour microgrid or the national grid. Both subsystems 1 and 2 can be arbitrarily treated as the following feedback state-space transfer functions $H_1(s)$ and $H_2(s)$, presented in (2.28):

$$\begin{aligned} v_1 &= H_1(s) \cdot i_1 \\ -i_2 &= H_2(s) \cdot v_2 \end{aligned} \tag{2.28}$$

Where $i_1 = -i_2 = i_{PoC}$ and $v_1 = v_2 = v_{PoC}$. Note that, by strategically defining these inputs and outputs, the transfer functions correspond to an impedance and to a negative admittance, respectively. Hence, $H_1(s) = Z_1$ and $H_2(s) = -Y_2$. Furthermore, both subsystems share input and output signals, as presented in Figure 2.16.

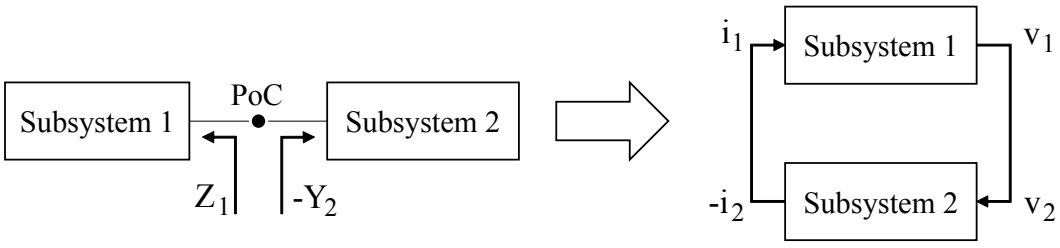

Figure 2.16: Source and Load Subsystems Impedances Feedback Loop [3].

By the feedback loop connection of these two subsystems, the Nyquist stability criteria can be applied and thus the small-signal stability can be studied.

As introduced in Section 1.1, in droop-controlled microgrids, impedances, i.e., transfer function between currents and voltages, are not enough to ensure stable operation. Unlike traditional PQ-inverters, droop-controlled inverters involve dynamics addressing the fundamental frequency, hence the analysis of the poles of the transfer functions relating voltages and currents are not enough. As a matter of fact, additional transfer functions relating the fundamental frequency should be considered in both subsystems, as shown in (2.29):

$$\begin{aligned} v_1 &= \begin{bmatrix} H_1(s) & H_1^{\omega}(s) \end{bmatrix} \cdot \begin{bmatrix} i_1 \\ \omega \end{bmatrix} \\ \begin{bmatrix} i_2 \\ \omega \end{bmatrix} &= \begin{bmatrix} H_2(s) \\ H_2^{\omega}(s) \end{bmatrix} \cdot v_2 \end{aligned} \tag{2.29}$$

A graphical generalized representation of the aforementioned feedback loops of droop-controlled microgrids is presented in Figure 2.17 [13].

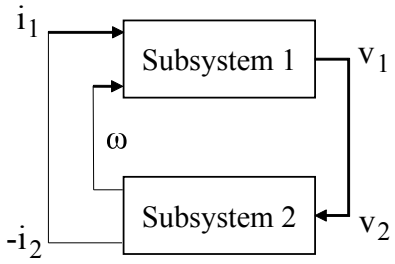

Figure 2.17: Source and Load Subsystems Transfer Functions Considering Frequency Channel

Despite the fact that small-signal impedance is just part of the necessary information in the case of the droop-controlled inverter, it is still a key issue for ensuring small-signal stability in the presence of a newly added power source of this type. This thesis production focuses on the *dq* impedance analysis in the synchronous reference frame, emphasizing in all four Z_{dd}, Z_{dq}, Z_{qd} and Z_{qq} transfer functions of this kind of inverter.

Chapter 3

Methodology

In this section, a description of the different stages of the proposed methodology to characterize the small-signal impedance of a droop-controlled inverter is presented. In Figure 3.1 is shown the methodological scheme as a flowchart.

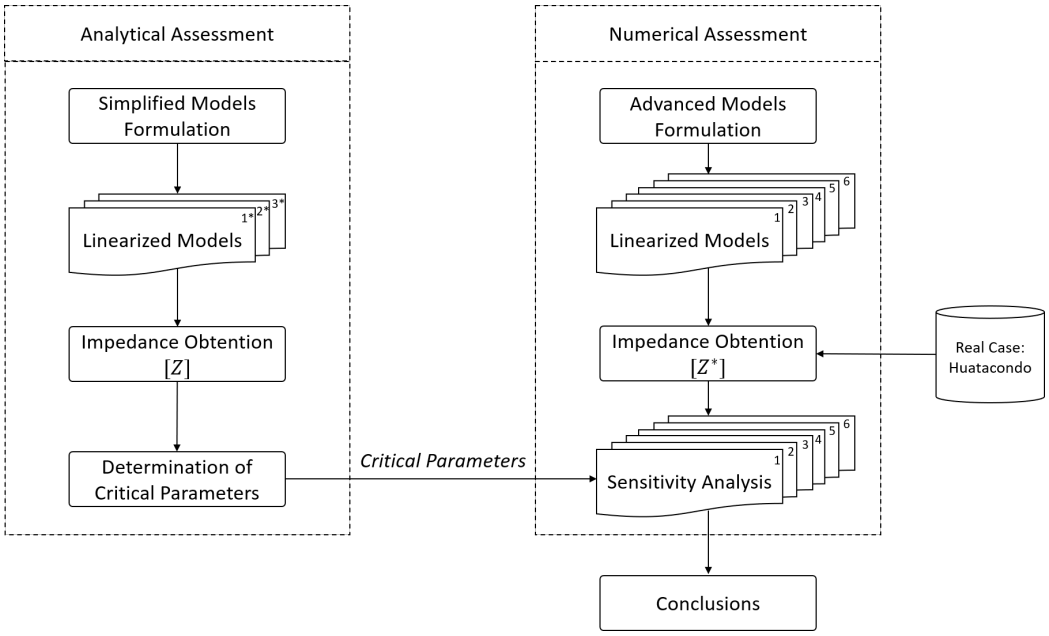

Figure 3.1: Methodological Framework

As stated in section 1.3.1, the main objective of this work is to understand how the small-signal impedance of the inverter is affected by both the internal parameters of the inverter and the operating point changes of the microgrid. The main idea to achieve this goal is divided in two main analysis:

1. **Analytical Assessment:** The main objective of this analysis is to obtain analytical expressions of the small-signal impedances of the inverter. With the formulation of these analytical expressions, the critical parameters of the inverter can be easily identified

(in this work, the critical parameters are referred to as the operational variables and inverter parameters whose changes directly affect the small-signal impedance of the inverter).

To achieve this goal, due to the complexity of the full-order model of the inverter and the impracticability to obtain its analytical small-signal impedance expressions, three different simplified low-order models (M1, M2 and M3) are developed. M1 corresponds to a simple ideal source. On the other hand, M2 corresponds to an active power droop-controlled source. Finally, M3 corresponds to a reactive power droop-controlled source. These three simplified models where specifically developed because they separately represent the main characteristics of a full-featured inverter, despite the simplifications.

This analysis is made by firstly linearizing the reduced-order systems and then obtaining analyzable mathematical expressions of the small-signal impedances of the inverter. Once these expressions are obtained, and considering that the small-signal impedances can be represented as multi-input multi-output transfer functions, an analytic bode plot characterization is developed. To do this, the poles, zeros and zero frequency values are obtained. Hence, the asymptotic limits of the Bode plots that describe the small-signal impedance shape are obtained.

Despite the fact that these models do not fully represent the real dynamics of an inverter, by analytically understanding the behavior of the small-signal impedances of these models, an intuition can be achieved about the impact that the operating point and the inverter parameters have on the small-signal impedance of the full-featured inverter.

2. **Numerical Assessment:** This analysis has two objectives. The main objective is to qualitatively analyze the small-signal impedance of the full-order model of the inverter presented in [25] through a sensitivity analysis with respect to the critical parameters identified in the analytical assessment, and then contrasting these results with the expected values from the analytical expressions of the low-order models.

   In addition, as presented in section 2.2.2, the full-order inverter model presents several subsystems, including the internal voltage and current controllers, the coupling inductance and the LC-filter, among others. It is desirable to identify the effects that these subsystems have on the small-signal impedance of the inverter. Therefore, additionally to the simplified models M1, M2, and M3, two partially complete models are developed by progressively adding the remaining subsystems. Specifically, M4 corresponds to a combination of both M2 and M3, having both droop controllers present. In M5, on the other hand, the LCL filter is completed by adding a series inductor and a parallel capacitor to the coupling inductor. Furthermore, the full-order model is also formalized as M6.

   In this case, the impedances cannot be analytically obtained, as explained previously, due to the complexity of the models, specially regarding models M5 and M6. Therefore, the small-signal impedances must be numerically computed for each model, by linearizing the models and then assessing the resulting small-signal impedances in previously defined operating points. In order to assess the small-signal impedances with a realistic operating point, the Huatacondo grid, a real microgrid located in the north of Chile, is studied. Once the study case is defined and the historical operating data of the microgrid is collected, a proper operating point (including currents, voltages and frequency) must be selected in order to assess the small-signal impedance expressions.

The centroid (the mean position of all the points in all of the coordinate directions) of these operating points is obtained and then the nearest point is selected as the base operating point. Additionally, the maximum and minimum values of these operating variables are obtained, in order to obtain the ranges of the sensitivity analysis.

Once the operating points are acquired, the small-signal impedances are numerically computed for each model. By varying, one at a time, each operating variable and inverter parameter of interest from the minimum to the maximum values, the sensitivity analysis can be performed.

Additionally, by assessing the small-signal impedance of all six inverter models in the base operating point, a comparison between them can be made. Considering that the models were developed by progressively adding the subsystems of the inverter, the effects that the subsystems have on the small-signal impedance can be successfully identified.

Once the analytical and numerical assessments are made, the critical parameters are tested on the full-order model, thus allowing us to conclude about the impedance characteristics. The main characteristics of the developed inverter models are presented below:

- **M1: Ideal Source** This model corresponds to a simple ideal source without control connected to an infinite busbar through a coupling inductor.
- **M2: Active Power Droop-Controlled Source** In this case, besides the ideal source and the coupling inductor, a single active power droop controller is added to the model, thus including a frequency dependency to the model.
- **M3: Reactive Power Droop-Controlled Source** Similar to M2, this model considers a single reactive power droop controller, in addition to the coupling inductor.
- **M4: Active and Reactive Power Droop-Controlled Source** This model corresponds to a combination of both M2 and M3, having both droop controllers present.
- **M5: Active and Reactive Power Droop-Controlled Source Considering LCL Filter** In this case, besides the aforementioned components, the LCL Filter is completed by coupling a series inductor and a parallel capacitor to the coupling inductor.
- **M6: Full Model** Finally, the inverter model is completed by considering the power measuring low-pass filter in the power control loop.

Chapter 4

Inverter Models Development

Once the equations that describe the grid-supporting inverter, presented in 2.2.2, are studied, simplified and linearized models can be obtained. Six different linearized models are developed and detailed in this chapter.

As stated previously, although the reduced-order models does not represent the real dynamics of the inverter, important insights can be obtained in order to be further compared with the full-order inverter analysis.

4.1. M1: Ideal Source

With the purpose of understanding the basic characteristics of the small-signal impedance of a voltage source inverter a non-controlled ideal source with a coupling inductance is modeled. The simplified inverter is presented in Figure 4.1.

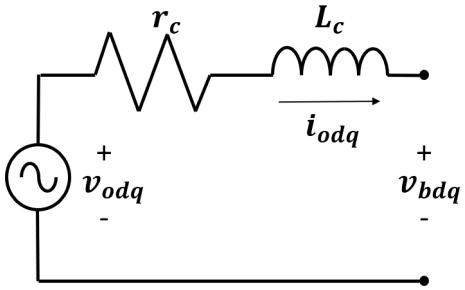

Figure 4.1: Ideal Source Inverter with Coupling Inductor

If neither control nor LC filter are present, this model only has three state-space equations, corresponding to the electrical equations of the coupling inductor and the local reference frame relative angle.

$$
\begin{aligned}
\dot{i_{od}} &= -\frac{r_c}{L_c} i_{od} + \omega i_{oq} + \frac{1}{L_c} v_{od} - \frac{1}{L_c} v_{bd} \\
\dot{i_{oq}} &= -\frac{r_c}{L_c} i_{oq} - \omega i_{od} + \frac{1}{L_c} v_{oq} - \frac{1}{L_c} v_{bq} \\
\dot{\delta} &= \omega - \omega_{com}
\end{aligned}
\tag{4.1}
$$

As no control is present, the ideal source is assumed to set the voltage and frequency in nominal values, as presented below:

$$
\begin{aligned}
v_{od} &= V_n \\
v_{oq} &= 0 \\
\omega &= \omega_n
\end{aligned}
\tag{4.2}
$$

In addition, from the reference frame transformation presented in (2.12), the following algebraic equations can be developed, making the connection of the inverter compatible with the global system:

$$
\begin{aligned}
v_{bd} &= v_{bD} \cdot \cos(\delta) + v_{bQ} \cdot \sin(\delta) \\
v_{bq} &= -v_{bD} \cdot \sin(\delta) + v_{bQ} \cdot \cos(\delta) \\
i_{oD} &= i_{od} \cdot \cos(\delta) - i_{oq} \cdot \sin(\delta) \\
i_{oD} &= i_{od} \cdot \sin(\delta) - i_{oq} \cdot \cos(\delta)
\end{aligned}
\tag{4.3}
$$

4.1.1. Linearization

The state, input, and output vectors are defined according to:

$$
\begin{aligned}
x_1 &= \begin{bmatrix} i_{od} & i_{oq} & \delta \end{bmatrix}^T \\
u_1 &= \begin{bmatrix} v_{bD} & v_{bQ} & \omega_{com} \end{bmatrix}^T \\
y_1 &= \begin{bmatrix} i_{oD} & i_{oQ} \end{bmatrix}^T
\end{aligned}
\tag{4.4}
$$

By evaluating (4.2) and (4.3) in (4.1) and linearizing, the following matrices are obtained, where capital letters and overlines denotes the variable evaluated in the operating point:

$$
A_1 = \begin{bmatrix} a^1_{1,1} & a^1_{1,2} & a^1_{1,3} \\ a^1_{2,1} & a^1_{2,2} & a^1_{2,3} \\ 0 & 0 & 0 \end{bmatrix}
\tag{4.5}
$$

where

$$
\begin{aligned}
a^1_{1,1} &= -\frac{r_c}{L_c} \\
a^1_{1,2} &= \omega_n \\
a^1_{1,3} &= -\frac{V_{bQ} \cdot \cos(\overline{\delta}) - V_{bD} \cdot \sin(\overline{\delta})}{L_c} \\
a^1_{2,1} &= -\omega_n \\
a^1_{2,2} &= -\frac{r_c}{L_c} \\
a^1_{2,3} &= \frac{V_{bD} \cdot cos(\overline{\delta}) + V_{bQ} \cdot \sin(\overline{\delta})}{L_c}
\end{aligned}
$$

$$
B_1 = \begin{bmatrix}
-\dfrac{\cos(\overline{\delta})}{L_c} & -\dfrac{\sin(\overline{\delta})}{L_c} & 0 \\
\dfrac{\sin(\overline{\delta})}{L_c} & -\dfrac{\cos(\overline{\delta})}{L_c} & 0 \\
0 & 0 & -1
\end{bmatrix} \tag{4.6}
$$

$$
C_1 = \begin{bmatrix}
\cos(\overline{\delta}) & -\sin(\overline{\delta}) & -I_{oq} \cdot \cos(\overline{\delta}) - I_{od} \cdot \sin(\overline{\delta}) \\
\sin(\overline{\delta}) & \cos(\overline{\delta}) & I_{od} \cdot \cos(\overline{\delta}) - I_{oq} \cdot \sin(\overline{\delta})
\end{bmatrix} \tag{4.7}
$$

$$
D_1 = 0 \tag{4.8}
$$

Evaluating in (2.19) and (2.20), it can be obtained the following linearized state-space system:

$$
\begin{aligned}
\Delta \dot{x_1} &= A_1 \Delta x_1 + B_1 \Delta u_1 \\
\Delta y_1 &= C_1 \Delta x_1
\end{aligned} \tag{4.9}
$$

4.2. M2: Active Power Droop-Controlled Source

To analyze the droop control effects on the linearized models, a purely active-power droop controlled inverter is modelled by adding the active droop control equations to M1, as shown in Figure 4.2

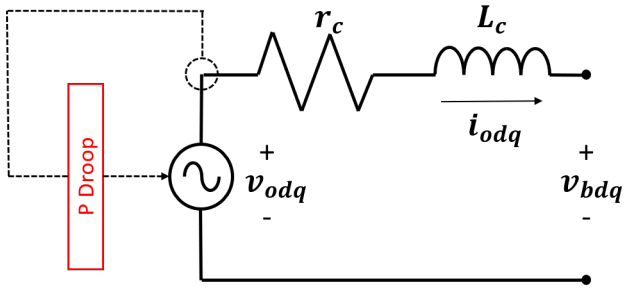

Figure 4.2: Ideal Source Inverter with Coupling Inductor and Active Power Droop Control

In this case, (4.1) are also valid. However, the expressions presented in (4.2) are replaced by the following droop-controlled frequency equation, assuming still an ideal voltage source:

$$\begin{aligned} v_{od} &= V_n \\ v_{oq} &= 0 \\ \omega &= \omega_n - m_p(P - P_n) \end{aligned} \tag{4.10}$$

As no low-pass filter is considered, measured power is instantly computed by the droop control equation as follows:

$$P = p = v_{od} i_{od} + v_{oq} i_{oq} \tag{4.11}$$

Thus, (4.10) can be rewritten as follows:

$$\begin{aligned} v_{od} &= V_n \\ v_{oq} &= 0 \\ \omega &= \omega_n - m_p \left(V_n i_{od} - P_n\right) \end{aligned} \tag{4.12}$$

4.2.1. Linearization

States, inputs, and outputs are the same as the previous case, as presented below:

$$\begin{aligned} x_2 &= \begin{bmatrix} i_{od} & i_{oq} & \delta \end{bmatrix}^T \\ u_2 &= \begin{bmatrix} v_{bD} & v_{bQ} & \omega_{com} \end{bmatrix}^T \\ y_2 &= \begin{bmatrix} i_{oD} & i_{oQ} \end{bmatrix}^T \end{aligned} \tag{4.13}$$

,

Considering the reference frame transformations presented in (4.3) and evaluating (4.1) in the corresponding (4.12), the linearized matrices are obtained:

$$A_2 = \begin{bmatrix} a_{1,1}^2 & a_{1,2}^2 & a_{1,3}^2 \\ a_{2,1}^2 & a_{2,2}^2 & a_{2,3}^2 \\ a_{3,1}^2 & 0 & 0 \end{bmatrix} \tag{4.14}$$

where

$$\begin{aligned} a_{1,1}^2 &= -\frac{r_c}{L_c} - V_n I_{oq} m_p \\ a_{1,2}^2 &= \omega_n - m_p(V_n I_{od} - P_n) \\ a_{1,3}^2 &= -\frac{V_{bQ} \cdot \cos(\bar{\delta}) - V_{bD} \cdot \sin(\bar{\delta})}{L_c} \\ a_{2,1}^2 &= V_n I_{od} m_p - (\omega_n - m_p(V_n I_{od} - P_n)) \\ a_{2,2}^2 &= -\frac{r_c}{L_c} \\ a_{2,3}^2 &= \frac{V_{bD} \cdot cos(\bar{\delta}) + V_{bQ} \cdot \sin(\bar{\delta})}{L_c} \\ a_{3,1}^2 &= -V_n m_p \end{aligned}$$

$$B_2 = \begin{bmatrix} -\frac{\cos(\bar{\delta})}{L_c} & -\frac{\sin(\bar{\delta})}{L_c} & 0 \\ \frac{\sin(\bar{\delta})}{L_c} & -\frac{\cos(\bar{\delta})}{L_c} & 0 \\ 0 & 0 & -1 \end{bmatrix} \tag{4.15}$$

$$C_2 = \begin{bmatrix} cos(\bar{\delta}) & -\sin(\bar{\delta}) & -I_{oq} \cdot \cos(\bar{\delta}) - I_{od} \cdot sin(\bar{\delta}) \\ sin(\bar{\delta}) & \cos(\bar{\delta}) & I_{od} \cdot \cos(\bar{\delta}) - I_{oq} \cdot sin(\bar{\delta}) \end{bmatrix} \tag{4.16}$$

$$D_2 = 0 \tag{4.17}$$

Thus, the following system is obtained:

$$\begin{aligned} \Delta \dot{x_2} &= A_2 \Delta x_2 + B_2 \Delta u_2 \\ \Delta y_2 &= C_2 \Delta x_2 \end{aligned} \tag{4.18}$$

4.3. M3: Reactive Power Droop-Controlled Source

In this case, a reactive-power droop controlled inverter is modelled. Similar to the previous case, the reactive droop control equations are added to M1, as shown in Figure 4.3

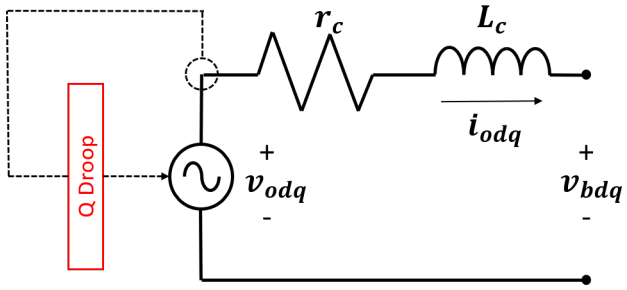

Figure 4.3: Ideal Source Inverter with Coupling Inductor and Reactive Power Droop Control

Same as previous model, coupling inductor dynamics represented in (4.1) are used. However, it is the voltage expression presented in (4.2) that needs to be changed. Considering the alignment with the d axis, the v_{od} reference voltage is presented next, as v_{oq} is still zero.

$$\begin{aligned} v_{od} &= V_n - n_q Q \\ v_{oq} &= 0 \end{aligned} \tag{4.19}$$

As the voltage source is considered ideal, and considering that measured power is instantly computed by the droop control equation, d axis source voltage v_{od} can be solved as follows:

$$\begin{aligned} Q = q &= v_{od} i_{oq} - v_{oq} i_{od} \\ \Rightarrow Q &= v_{od} i_{oq} \\ \Rightarrow v_{od} &= V_n - n_q \left(v_{od} i_{oq} \right) \\ \Rightarrow v_{od} &= \frac{V_n}{1 + n_q i_{oq}} \end{aligned} \tag{4.20}$$

Thus, the obtained equations set is presented below:

$$\begin{aligned} v_{od} &= \frac{V_n}{1 + n_q i_{oq}} \\ v_{oq} &= 0 \\ \omega &= \omega_n \end{aligned} \tag{4.21}$$

4.3.1. Linearization

As no state is added by the reactive droop controller, the state, input, and output vectors remain the same as previous cases:

$$\begin{aligned} x_3 &= \begin{bmatrix} i_{od} & i_{oq} & \delta \end{bmatrix}^T \\ u_3 &= \begin{bmatrix} v_{bD} & v_{bQ} & \omega_{com} \end{bmatrix}^T \\ y_3 &= \begin{bmatrix} i_{oD} & i_{oQ} \end{bmatrix}^T \end{aligned} \tag{4.22}$$

After evaluating (4.1) with (4.21) and considering (4.3), the system is linearized, obtaining the following matrices:

$$A_3 = \begin{bmatrix} a^3_{1,1} & a^3_{1,2} & a^3_{1,3} \\ a^3_{2,1} & a^3_{2,2} & a^3_{2,3} \\ 0 & 0 & 0 \end{bmatrix} \tag{4.23}$$

where

$$\begin{aligned} a^3_{1,1} &= -\frac{r_c}{L_c} \\ a^3_{1,2} &= \omega_n + \frac{V_n n_q}{L_c \left(n_q i_{oq}\right)^2} \\ a^3_{1,3} &= -\frac{V_{bQ} \cdot \cos(\overline{\delta}) - V_{bD} \cdot \sin(\overline{\delta})}{L_c} \\ a^3_{2,1} &= -\omega_n \\ a^3_{2,2} &= -\frac{r_c}{L_c} \\ a^3_{2,3} &= \frac{V_{bD} \cdot \cos(\overline{\delta}) + V_{bQ} \cdot \sin(\overline{\delta})}{L_c} \end{aligned}$$

$$B_3 = \begin{bmatrix} -\dfrac{\cos(\overline{\delta})}{L_c} & -\dfrac{\sin(\overline{\delta})}{L_c} & 0 \\ \dfrac{\sin(\overline{\delta})}{L_c} & -\dfrac{\cos(\overline{\delta})}{L_c} & 0 \\ 0 & 0 & -1 \end{bmatrix} \tag{4.24}$$

$$C_3 = \begin{bmatrix} \cos(\overline{\delta}) & -\sin(\overline{\delta}) & -I_{oq} \cdot \cos(\overline{\delta}) - I_{od} \cdot \sin(\overline{\delta}) \\ \sin(\overline{\delta}) & \cos(\overline{\delta}) & I_{od} \cdot \cos(\overline{\delta}) - I_{oq} \cdot \sin(\overline{\delta}) \end{bmatrix} \tag{4.25}$$

$$D_3 = 0 \tag{4.26}$$

Thus, the next system is obtained:

$$\begin{aligned} \Delta \dot{x_3} &= A_3 \Delta x_3 + B_3 \Delta u_3 \\ \Delta y_3 &= C_3 \Delta x_3 \end{aligned} \tag{4.27}$$

4.4. M4: Active and Reactive Power Droop-Controlled Source

In order to analyze the combined effect of both active and reactive power droop controllers, the model presented in Figure 4.4 is developed.

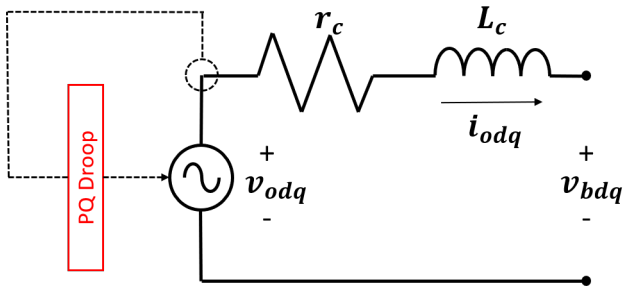

Figure 4.4: Ideal Source Inverter with Coupling Inductor and Complete Droop Control

In this case, both voltage and frequency reference values are modified as follows:

$$\begin{aligned} v_{od} &= V_n - n_q Q \\ v_{oq} &= 0 \\ \omega &= \omega_n - m_p \left(P - P_n \right) \end{aligned} \tag{4.28}$$

Same as in M2 and M3, measured powers are instantly operated in the droop equations, as follows:

$$\begin{aligned} P = p &= v_{od} i_{od} + v_{oq} i_{oq} \\ Q = q &= v_{od} i_{oq} - v_{oq} i_{od} \end{aligned} \tag{4.29}$$

Controlled voltage v_{od} can be solved as in (4.20). Thus, (4.30) obtained.

$$
\begin{aligned}
v_{od} &= \frac{V_n}{1 + n_q i_{oq}} \\
v_{oq} &= 0 \\
\omega &= \omega_n - m_p \left(\frac{V_n}{1 + n_q i_{oq}} i_{od} - P_n \right)
\end{aligned}
\tag{4.30}
$$

4.4.1. Linearization

Once again, no states variables are added by the reactive droop controller, thus the state, input, and output vectors remain the same as the previous cases:

$$
\begin{aligned}
x_4 &= \begin{bmatrix} i_{od} & i_{oq} & \delta \end{bmatrix}^T \\
u_4 &= \begin{bmatrix} v_{bD} & v_{bQ} & \omega_{com} \end{bmatrix}^T \\
y_4 &= \begin{bmatrix} i_{oD} & i_{oQ} \end{bmatrix}^T
\end{aligned}
\tag{4.31}
$$

As no electrical component has been added, by evaluating (4.1) with (4.3) and (4.30) are obtained and linearized, resulting in the following matrices:

$$
A_4 = \begin{bmatrix} a^4_{1,1} & a^4_{1,2} & a^4_{1,3} \\ a^4_{2,1} & a^4_{2,2} & a^4_{2,3} \\ a^4_{3,1} & a^4_{3,2} & 0 \end{bmatrix}
\tag{4.32}
$$

where

$$
\begin{aligned}
a^4_{1,1} &= \frac{V_n I_{oq} m_p}{n_q I_{oq} - 1} - \frac{r_c}{L_c} \\
a^4_{1,2} &= \left(\omega_n - m_p \left(\frac{V_n}{1 + n_q I_{oq}} I_{od} - P_n \right) \right) + \frac{V_n n_q}{L_c \left(n_q I_{oq} \right)^2} - \frac{V_n I_{od} I_{oq} m_p n_q}{\left(n_q I_{oq} \right)^2} \\
a^4_{1,3} &= -\frac{V_{bQ} \cdot \cos(\overline{\delta}) - V_{bD} \cdot \sin(\overline{\delta})}{L_c} \\
a^4_{2,1} &= -\left(\omega_n - m_p \left(\frac{V_n}{1 + n_q I_{oq}} I_{od} - P_n \right) \right) - \frac{V_n I_{od} m_p}{n_q I_{oq} - 1} \\
a^4_{2,2} &= \frac{V_n i^2_{od} m_p n_q}{\left(n_q I_{oq} - 1 \right)^2} - \frac{r_c}{L_c} \\
a^4_{2,3} &= \frac{V_{bD} \cdot \cos(\overline{\delta}) + V_{bQ} \cdot \sin(\overline{\delta})}{L_c} \\
a^4_{3,1} &= \frac{V_n m_p}{n_q I_{oq} - 1} \\
a^4_{3,2} &= -\frac{V_n I_{od} m_p n_q}{\left(n_q I_{oq} - 1 \right)^2}
\end{aligned}
$$

$$B_4 = \begin{bmatrix} -\frac{\cos(\bar{\delta})}{L_c} & -\frac{\sin(\bar{\delta})}{L_c} & 0 \\ \frac{\sin(\bar{\delta})}{L_c} & -\frac{\cos(\bar{\delta})}{L_c} & 0 \\ 0 & 0 & -1 \end{bmatrix} \tag{4.33}$$

$$C_4 = \begin{bmatrix} \cos(\bar{\delta}) & -\sin(\bar{\delta}) & -I_{oq} \cdot \cos(\bar{\delta}) - I_{od} \cdot \sin(\bar{\delta}) \\ \sin(\bar{\delta}) & \cos(\bar{\delta}) & I_{od} \cdot \cos(\bar{\delta}) - I_{oq} \cdot \sin(\bar{\delta}) \end{bmatrix} \tag{4.34}$$

$$D_4 = 0 \tag{4.35}$$

Hence, the linearized system presented in (4.36) is obtained:

$$\begin{aligned} \Delta\dot{x}_4 &= A_4\Delta x_4 + B_4\Delta u_4 \\ \Delta y_4 &= C_4\Delta x_4 \end{aligned} \tag{4.36}$$

4.5. M5: Active and Reactive Power Droop-Controlled Source Considering LCL Filter

In this model, an LC filter is added. As the droop controller is not expected to control power in terminals of the ideal voltage source, but in the capacitor, the internal control loops are also included, as shown in Figure 4.5.

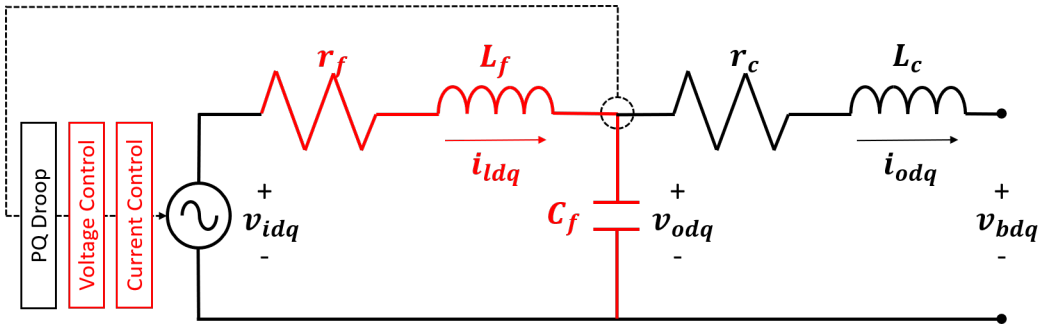

Figure 4.5: Ideal Source Inverter with Coupling Inductor, Complete Droop Control and LC Filter

This case considers both the differential equations of the ideal source connected to the LCL system, presented in (2.11) and the reference frame rotation angle equation in (2.14).

Additionally, both differential and algebraic voltage and current control equations, presented in (2.7)-(2.10), are used.

Same as previous model, as still no measuring filter is considered, (4.29) can be used to evaluate the model. Then, the voltage reference and droop-controlled frequency equations are obtained. Note that unlike previous cases, reference voltages are not instantly applied in the capacitor.

$$\begin{aligned} v_{od}^{*} &= V_n - n_q \left(v_{od} i_{oq} - v_{oq} i_{od}\right) \\ v_{oq}^{*} &= 0 \\ \omega &= \omega_n - m_p \left(v_{od} i_{od} + v_{oq} i_{oq} - P_n\right) \end{aligned} \tag{4.37}$$

4.5.1. Linearization

Four states were introduced by the LC filter, in addition to four states corresponding to the PI controllers of the voltage and current loops, totaling an *11*th order system. Hence, the state, input and output vectors are, respectively:

$$\begin{aligned} x_5 &= \begin{bmatrix} v_{od} & v_{oq} & i_{od} & i_{oq} & i_{ld} & i_{lq} & \delta & \phi_d & \phi_q & \gamma_d & \gamma_q \end{bmatrix}^T \\ u_5 &= \begin{bmatrix} v_{bD} & v_{bQ} & \omega_{com} \end{bmatrix}^T \\ y_5 &= \begin{bmatrix} i_{oD} & i_{oQ} \end{bmatrix}^T \end{aligned} \tag{4.38}$$

By evaluating the corresponding differential equations with (2.8), (2.10) and (4.3), considering also the output current globally-referred equations, the linearization is made and the obtained matrices are presented in (4.39).

$$A_5 = \begin{bmatrix} a_{1,1}^5 & a_{1,2}^5 & a_{1,3}^5 & a_{1,4}^5 & a_{1,5}^5 & 0 & 0 & 0 & 0 & 0 & 0 \\ a_{2,1}^5 & a_{2,2}^5 & a_{2,3}^5 & a_{2,4}^5 & 0 & a_{2,6}^5 & 0 & 0 & 0 & 0 & 0 \\ a_{3,1}^5 & a_{3,2}^5 & a_{3,3}^5 & a_{3,4}^5 & 0 & 0 & a_{3,7}^5 & 0 & 0 & 0 & 0 \\ a_{4,1}^5 & a_{4,2}^5 & a_{4,3}^5 & a_{4,4}^5 & 0 & 0 & a_{4,7}^5 & 0 & 0 & 0 & 0 \\ a_{5,1}^5 & a_{5,2}^5 & a_{5,3}^5 & a_{5,4}^5 & a_{5,5}^5 & a_{5,6}^5 & 0 & a_{5,8}^5 & 0 & a_{5,10}^5 & 0 \\ a_{6,1}^5 & a_{6,2}^5 & a_{6,3}^5 & a_{6,4}^5 & a_{6,5}^5 & a_{6,6}^5 & 0 & 0 & a_{6,9}^5 & 0 & a_{6,11}^5 \\ a_{7,1}^5 & a_{7,2}^5 & a_{7,3}^5 & a_{7,4}^5 & 0 & 0 & 0 & 0 & 0 & 0 & 0 \\ a_{8,1}^5 & a_{8,2}^5 & a_{8,3}^5 & a_{8,4}^5 & 0 & 0 & 0 & 0 & 0 & 0 & 0 \\ 0 & -1 & 0 & 0 & 0 & 0 & 0 & 0 & 0 & 0 & 0 \\ a_{10,1}^5 & a_{10,2}^5 & a_{10,3}^5 & a_{10,4}^5 & -1 & 0 & 0 & a_{10,8}^5 & 0 & 0 & 0 \\ a_{11,1}^5 & a_{11,2}^5 & 0 & 1 & 0 & -1 & 0 & 0 & a_{11,9}^5 & 0 & 0 \end{bmatrix} \tag{4.39}$$

where

$$a^5_{1,1} = -V_{oq} I_{od} m_p$$
$$a^5_{1,2} = \overline{\omega} - V_{oq} I_{oq} m_p$$
$$a^5_{1,3} = -\frac{1}{C_f} - V_{od} V_{oq} m_p$$
$$a^5_{1,4} = -V^2_{oq} m_p$$
$$a^5_{1,5} = \frac{1}{C_f}$$
$$a^5_{2,1} = V_{od} I_{od} m_p - \overline{\omega}$$
$$a^5_{2,2} = V_{od} I_{oq} m_p$$
$$a^5_{2,3} = V^2_{od} m_p$$
$$a^5_{2,4} = -\frac{1}{C_f} + V_{od} V_{oq} m_p$$
$$a^5_{2,6} = \frac{1}{C_f}$$
$$a^5_{3,1} = \frac{1}{L_C} - I_{od} I_{oq} m_p$$
$$a^5_{3,2} = -I^2_{oq} m_p$$
$$a^5_{3,3} = -\frac{r_C}{L_C} - V_{od} I_{oq} m_p$$
$$a^5_{3,4} = \overline{\omega} - V_{oq} I_{oq} m_p$$
$$a^5_{3,7} = -\frac{V_{bQ} \cdot \cos(\overline{\delta}) - V_{bD} \cdot \sin(\overline{\delta})}{L_C}$$
$$a^5_{4,1} = I^2_{od} m_p$$
$$a^5_{4,2} = \frac{1}{L_C} + I_{od} I_{oq} m_p$$
$$a^5_{4,3} = -\overline{\omega} + V_{od} I_{od} m_p$$
$$a^5_{4,4} = \overline{\omega} - V_{oq} I_{oq} m_p$$
$$a^5_{4,7} = \frac{V_{bD} \cdot \cos(\overline{\delta}) + V_{bQ} \cdot \sin(\overline{\delta})}{L_C}$$
$$a^5_{5,1} = -\frac{K_{pc} K_{pv} \left(I_{oq} n_q + 1\right) + 1}{L_f} - I_{lq} I_{od} m_p$$
$$a^5_{5,2} = -\frac{K_{pc} \left(C_f \omega_n - I_{od} K_{pv} n_q\right)}{L_f} - I_{lq} I_{oq} m_p$$
$$a^5_{5,3} = \frac{K_{pc} \left(V_{oq} K_{pv} n_q + 1\right)}{Lf} - V_{od} I_{lq} m_p$$
$$a^5_{5,4} = -\frac{V_{od} K_{pc} K_{pv} n_q}{L_f} - V_{oq} I_{lq} m_p$$
$$a^5_{5,5} = -\frac{K_{pc}}{L_f} - \frac{r_f}{L_f}$$
$$a^5_{5,6} = \overline{\omega} - \omega_n$$
$$a^5_{5,8} = \frac{K_{iv} K_{pc}}{L_f}$$
$$a^5_{5,10} = \frac{K_{ic}}{L_f}$$
$$a^5_{6,1} = \frac{C_f K_{pc} \omega_n}{L_f} + I_{ld} I_{od} m_p$$
$$a^5_{6,2} = -\frac{K_{pc} K_{pv} + 1}{L_f} + I_{ld} I_{oq} m_p$$
$$a^5_{6,3} = V_{od} I_{ld} m_p$$
$$a^5_{6,4} = \frac{K_{pc}}{L_f} + V_{oq} I_{lq} m_p$$
$$a^5_{6,5} = \omega_n - \overline{\omega}$$
$$a^5_{6,6} = -\frac{K_{pc}}{L_f} - \frac{r_f}{L_f}$$
$$a^5_{6,9} = \frac{K_{iv} K_{pc}}{L_f}$$
$$a^5_{6,11} = \frac{K_{ic}}{L_f}$$
$$a^5_{7,1} = -I_{od} m_p$$
$$a^5_{7,2} = -I_{oq} m_p$$
$$a^5_{7,3} = -V_{od} m_p$$
$$a^5_{7,4} = -V_{oq} m_p$$
$$a^5_{8,1} = -I_{oq} n_q - 1$$
$$a^5_{8,2} = I_{od} n_q$$
$$a^5_{8,3} = V_{oq} n_q$$
$$a^5_{8,4} = -V_{od} n_q$$
$$a^5_{10,1} = -K_{pv} \left(I_{oq} n_q + 1\right)$$
$$a^5_{10,2} = I_{od} K_{pv} n_q - C_f \omega_n$$
$$a^5_{10,3} = V_{oq} K_{pv} n_q + 1$$
$$a^5_{10,4} = -V_{od} K_{pv} n_q$$
$$a^5_{10,8} = K_{iv}$$
$$a^5_{11,1} = C_f \omega_n$$
$$a^5_{11,2} = -K_{pv}$$
$$a^5_{11,3} = K_{iv}$$

$$B_5 = \begin{bmatrix} 0 & 0 & 0 \\ 0 & 0 & 0 \\ -\frac{\cos(\bar{\delta})}{L_c} & -\frac{\sin(\bar{\delta})}{L_c} & 0 \\ \frac{\sin(\bar{\delta})}{L_c} & -\frac{\cos(\bar{\delta})}{L_c} & 0 \\ 0 & 0 & 0 \\ 0 & 0 & 0 \\ 0 & 0 & -1 \\ 0 & 0 & 0 \\ 0 & 0 & 0 \\ 0 & 0 & 0 \\ 0 & 0 & 0 \end{bmatrix} \tag{4.40}$$

$$C_5 = \begin{bmatrix} 0 & 0 & \cos(\bar{\delta}) & -\sin(\bar{\delta}) & 0 & 0 & -I_{oq} \cdot \cos(\bar{\delta}) - I_{od} \cdot \sin(\bar{\delta}) & 0 & 0 & 0 & 0 \\ 0 & 0 & \sin(\bar{\delta}) & \cos(\bar{\delta}) & 0 & 0 & I_{od} \cdot \cos(\bar{\delta}) - I_{oq} \cdot \sin(\bar{\delta}) & 0 & 0 & 0 & 0 \end{bmatrix} \tag{4.41}$$

$$D_5 = 0 \tag{4.42}$$

The obtained system is presented below:

$$\begin{aligned} \Delta \dot{x_5} &= A_5 \Delta x_5 + B_5 \Delta u_5 \\ \Delta y_5 &= C_5 \Delta x_5 \end{aligned} \tag{4.43}$$

4.6. M6: Full Model

Finally, the full-order inverter is presented in Figure 4.6. The main difference with the previous model is the inclusion of the power measuring low-pass filter.

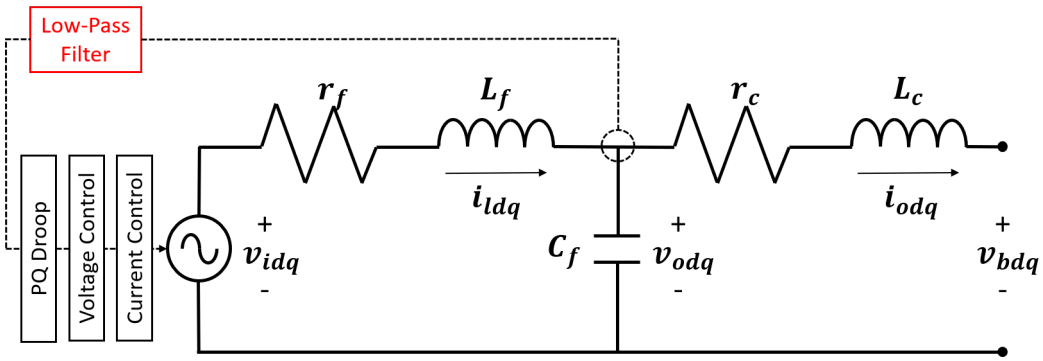

Figure 4.6: Full-order modelled inverter

As this model corresponds to the full model, equations presented in Section 2.2.2 are used.

4.6.1. Linearization

Two states are introduced by the low-pass filter, corresponding to the measured active and reactive power, completing the *13*th order model. The corresponding vectors are listed below:

$$\begin{aligned} x_6 &= \begin{bmatrix} v_{od} & v_{oq} & i_{od} & i_{oq} & i_{ld} & i_{lq} & \delta & \phi_d & \phi_q & \gamma_d & \gamma_q & P & Q \end{bmatrix}^T \\ u_6 &= \begin{bmatrix} v_{bD} & v_{bQ} & \omega_{com} \end{bmatrix}^T \\ y_6 &= \begin{bmatrix} i_{oD} & i_{oQ} \end{bmatrix}^T \end{aligned} \tag{4.44}$$

The resulting linearized matrices are obtained, as presented below:

$$A_6 = \begin{bmatrix} 0 & a^6_{1,2} & a^6_{1,3} & 0 & a^6_{1,5} & 0 & 0 & 0 & 0 & 0 & 0 & a^6_{1,12} & 0 \\ a^6_{2,1} & 0 & 0 & a^6_{2,4} & 0 & a^6_{2,6} & 0 & 0 & 0 & 0 & 0 & a^6_{2,12} & 0 \\ a^6_{3,1} & 0 & a^6_{3,3} & a^6_{3,4} & 0 & 0 & a^6_{3,7} & 0 & 0 & 0 & 0 & a^6_{3,12} & 0 \\ 0 & a^6_{4,2} & a^6_{4,3} & a^6_{4,4} & 0 & 0 & a^6_{4,7} & 0 & 0 & 0 & 0 & a^6_{4,12} & 0 \\ a^6_{5,1} & a^6_{5,2} & a^6_{5,3} & 0 & a^6_{5,5} & a^6_{5,6} & 0 & a^6_{5,8} & 0 & a^6_{5,10} & 0 & a^6_{5,12} & a^6_{5,13} \\ a^6_{6,1} & a^6_{6,2} & 0 & a^6_{6,4} & a^6_{6,5} & a^6_{6,6} & 0 & 0 & a^6_{6,9} & 0 & a^6_{6,11} & a^6_{6,12} & 0 \\ 0 & 0 & 0 & 0 & 0 & 0 & 0 & 0 & 0 & 0 & 0 & a^6_{7,12} & 0 \\ -1 & 0 & 0 & 0 & 0 & 0 & 0 & 0 & 0 & 0 & 0 & 0 & a^6_{8,13} \\ 0 & -1 & 0 & 0 & 0 & 0 & 0 & 0 & 0 & 0 & 0 & 0 & 0 \\ a^6_{10,1} & a^6_{10,2} & 1 & 0 & -1 & 0 & 0 & a^6_{10,8} & 0 & 0 & 0 & 0 & a^6_{10,13} \\ a^6_{11,1} & a^6_{11,2} & 0 & 1 & 0 & -1 & 0 & 0 & a^6_{11,9} & 0 & 0 & 0 & \\ a^6_{12,1} & a^6_{12,2} & a^6_{12,3} & a^6_{12,4} & 0 & 0 & 0 & 0 & 0 & 0 & 0 & a^6_{12,12} & 0 \\ a^6_{13,1} & a^6_{13,2} & a^6_{13,3} & a^6_{13,4} & 0 & 0 & 0 & 0 & 0 & 0 & 0 & 0 & a^6_{13,13} \end{bmatrix} \tag{4.45}$$

where

$$a^6_{1,2} = \overline{\omega}$$
$$a^6_{1,3} = -\frac{1}{C_f}$$
$$a^6_{1,5} = \frac{1}{C_f}$$
$$a^6_{1,12} = -V_{oq} m_p$$
$$a^6_{2,1} = -\overline{\omega}$$
$$a^6_{2,4} = -\frac{1}{C_f}$$
$$a^6_{2,6} = \frac{1}{C_f}$$
$$a^6_{2,12} = -V_{od} m_p$$
$$a^6_{3,1} = \frac{1}{L_C}$$
$$a^6_{3,2} = 0$$
$$a^6_{3,3} = -\frac{r_C}{L_C}$$
$$a^6_{3,4} = \overline{\omega}$$
$$a^6_{3,7} = -\frac{V_{bQ} \cdot \cos(\overline{\delta}) - V_{bD} \cdot \sin(\overline{\delta})}{L_C}$$
$$a^6_{3,12} = -I_{oq} m_p$$
$$a^6_{4,2} = \frac{1}{L_C}$$
$$a^6_{4,3} = -\overline{\omega}$$
$$a^6_{4,4} = -\frac{r_C}{L_C}$$
$$a^6_{4,7} = \frac{V_{bD} \cdot \cos(\overline{\delta}) + V_{bQ} \cdot \sin(\overline{\delta})}{L_C}$$
$$a^6_{4,12} = I_{od} m_p$$
$$a^6_{5,1} = -\frac{K_{pc} K_{pv} + 1}{L_f}$$
$$a^6_{5,2} = -\frac{K_{pc} C_f \omega_n}{L_f}$$
$$a^6_{5,3} = \frac{K_{pc}}{Lf}$$
$$a^6_{5,5} = -\frac{K_{pc}}{L_f} - \frac{r_f}{L_f}$$
$$a^6_{5,6} = \overline{\omega} - \omega_n$$
$$a^6_{5,8} = \frac{K_{iv} K_{pc}}{L_f}$$
$$a^6_{5,10} = \frac{K_{ic}}{L_f}$$
$$a^6_{5,12} = -I_{lq} m_p$$
$$a^6_{5,13} = -\frac{K_{pc} K_{pv} n_q}{L_f}$$
$$a^6_{6,1} = \frac{C_f K_{pc} \omega_n}{L_f}$$
$$a^6_{6,2} = -\frac{K_{pc} K_{pv} + 1}{L_f}$$
$$a^6_{6,4} = -\frac{K_{pc}}{L_f}$$
$$a^6_{6,5} = \omega_n - \overline{\omega}$$
$$a^6_{6,6} = -\frac{K_{pc}}{L_f} - \frac{r_f}{L_f}$$
$$a^6_{6,9} = \frac{K_{iv} K_{pc}}{L_f}$$
$$a^6_{6,11} = \frac{K_{ic}}{L_f}$$
$$a^6_{6,12} = I_{ld} m_p$$
$$a^6_{7,12} = -m_p$$
$$a^6_{8,13} = -n_q$$
$$a^6_{10,1} = -K_{pv}$$
$$a^6_{10,2} = -C_f \omega_n$$
$$a^6_{10,8} = K_{iv}$$
$$a^6_{10,13} = -K_{pv} n_q$$
$$a^6_{11,1} = C_f \omega_n$$
$$a^6_{11,2} = -K_{pv}$$
$$a^6_{11,9} = K_{iv}$$
$$a^6_{12,1} = I_{od} \omega_c$$
$$a^6_{12,2} = I_{oq} \omega_c$$
$$a^6_{12,3} = V_{od} \omega_c$$
$$a^6_{12,4} = V_{oq} \omega_c$$
$$a^6_{12,12} = -\omega_c$$
$$a^6_{13,1} = I_{oq} \omega_c$$
$$a^6_{13,2} = -I_{od} \omega_c$$
$$a^6_{13,3} = -V_{oq} \omega_c$$
$$a^6_{13,4} = V_{od} \omega_c$$
$$a^6_{13,13} = -\omega_c$$

$$B_6 = \begin{bmatrix} 0 & 0 & 0 \\ 0 & 0 & 0 \\ -\dfrac{\cos(\overline{\delta})}{L_c} & -\dfrac{\sin(\overline{\delta})}{L_c} & 0 \\ \dfrac{\sin(\overline{\delta})}{L_c} & -\dfrac{\cos(\overline{\delta})}{L_c} & 0 \\ 0 & 0 & 0 \\ 0 & 0 & 0 \\ 0 & 0 & -1 \\ 0 & 0 & 0 \\ 0 & 0 & 0 \\ 0 & 0 & 0 \\ 0 & 0 & 0 \\ 0 & 0 & 0 \\ 0 & 0 & 0 \end{bmatrix} \tag{4.46}$$

$$C_6 = \begin{bmatrix} 0 & 0 & \cos(\overline{\delta}) & -\sin(\overline{\delta}) & 0 & 0 & -I_{oq} \cdot \cos(\overline{\delta}) - I_{od} \cdot \sin(\overline{\delta}) & 0 & 0 & 0 & 0 & 0 & 0 \\ 0 & 0 & \sin(\overline{\delta}) & \cos(\overline{\delta}) & 0 & 0 & I_{od} \cdot \cos(\overline{\delta}) - I_{oq} \cdot \sin(\overline{\delta}) & 0 & 0 & 0 & 0 & 0 & 0 \end{bmatrix} \tag{4.47}$$

$$D_6 = 0 \tag{4.48}$$

The obtained system is presented below:

$$\begin{aligned} \Delta \dot{x_6} &= A_6 \Delta x_6 + B_6 \Delta u_6 \\ \Delta y_6 &= C_6 \Delta x_6 \end{aligned} \tag{4.49}$$

Chapter 5

Analytical Assessment

The main objective of this chapter is to provide analytic expressions of the small-signal impedances for the simplified inverter models presented in previous section, specifically for the ideal source and single droop-controlled models. Understanding the small-signal behavior of these simplified reduced order models can provide important insights about the small-signal impedance of the full-order inverter model.

In order to simplify the analysis and to provide more understandable algebraic conclusions, the reference frame angle δ is approximated to zero in the models of this analytical assessment, as specified later in this chapter.

5.1. M1: Ideal Source

5.1.1. Small-Signal Impedance Obtainment

In first place, the small-signal impedance must be obtained from the corresponding linearized matrices presented from (4.5) to (4.8). Firstly, the transfer function H_1 is obtained, by rearranging (2.22) as follows:

$$\Delta y_1 = H_1 \cdot \Delta u_1 \tag{5.1}$$

where

$$H_1 = C_1 \left(sI - A_1\right)^{-1} B_1 + D_1 \tag{5.2}$$

Considering (4.4), the result can be rewritten as:

$$\begin{bmatrix}\Delta i_{oD}\\ \Delta i_{oQ}\end{bmatrix} = \begin{bmatrix}H_{11}(s) & H_{12}(s) & H_{13}(s)\\ H_{21}(s) & H_{22}(s) & H_{23}(s)\end{bmatrix} \cdot \begin{bmatrix}\Delta v_{bD}\\ \Delta v_{bQ}\\ \Delta w_{com}\end{bmatrix} \tag{5.3}$$

As defined in Section 2.5.1, only the channels relating currents and voltages are of interest. Hence, the following small-signal admittance transfer function can be defined by fixing the common reference frequency input:

$$\begin{bmatrix}\Delta i_{oD}\\ \Delta i_{oQ}\end{bmatrix} = \begin{bmatrix}Y_{DD}(s) & Y_{DQ}(s)\\ Y_{QD}(s) & Y_{QQ}(s)\end{bmatrix} \cdot \begin{bmatrix}\Delta v_{bD}\\ \Delta v_{bQ}\end{bmatrix} \tag{5.4}$$

where

$$\begin{aligned} Y_{DD} &= H_{11}(s) \quad Y_{DQ} = H_{12}(s)\\ Y_{QD} &= H_{21}(s) \quad Y_{QQ} = H_{22}(s)\end{aligned} \tag{5.5}$$

By evaluating (5.4) with (4.5)-(4.8) and then computing the inverse, the following small-signal impedance is obtained:

$$\begin{bmatrix}\Delta v_{oD}\\ \Delta v_{oQ}\end{bmatrix} = \begin{bmatrix}Z_{DD}(s) & Z_{DQ}(s)\\ Z_{QD}(s) & Z_{QQ}(s)\end{bmatrix} \cdot \begin{bmatrix}\Delta i_{bD}\\ \Delta i_{bQ}\end{bmatrix} \tag{5.6}$$

where

$$\begin{aligned} Z_{DD}(s) &= -\left(r_C + s \cdot L_C\right)\\ Z_{DQ}(s) &= L_c\omega_n\\ Z_{QD}(s) &= -L_c\omega_n\\ Z_{QQ}(s) &= -\left(r_C + s \cdot L_C\right)\end{aligned} \tag{5.7}$$

5.1.2. Bode Plot Analytic Characterization

As stated in section 2.4.3, in order to characterize the asymptotic limits of the small-signal impedance plot, if seen as a transfer function, a Bode plot analysis is made.

1. Z_{DD} **Impedance:** Firstly, the impedance value is obtained by replacing the corresponding equation in (5.7), when the frequency is set to zero, as follows:

$$\begin{aligned} Z_{DD}^{M1}(0) &= -\left(r_C + 0 \cdot L_C\right) \\ &\Rightarrow Z_{DD}^{M1}(0) = -r_C \end{aligned} \tag{5.8}$$

In second place, the set of poles p_{DD}^{M1} is obtained similarly as in Section 2.4.3. It can be noted that, in this case, there are no poles, as it has no denominator:

$$p_{DD}^{M1} = \{\varnothing\} \tag{5.9}$$

At last, the set of zeros of the system is obtained. As this case is a *1*st order transfer function with no poles, only one zero is obtained, as follows:

$$\begin{aligned} Z_{DD}(s) &= 0 \\ \Rightarrow -\left(r_C + s \cdot L_C\right) &= 0 \\ \Rightarrow z_{DD}^{M1} &= \{-\frac{r_C}{L_C}\} \end{aligned} \tag{5.10}$$

2. Z_{DQ} **Impedance:** As no frequency dependency is present, the small-signal transfer function is a constant value. Thus, the zero frequency value corresponds to:

$$Z_{DQ}^{M1}(0) = L_c\omega_n \tag{5.11}$$

In this case, as the transfer function is constant, neither poles nor zeros are present. Thus, the set of poles and zeros for this model are empty, as presented below:

$$p_{DQ}^{M1} = \{\varnothing\} \tag{5.12}$$

$$z_{DQ}^{M1} = \{\varnothing\} \tag{5.13}$$

3. Z_{QD} **Impedance:** Similarly to previous case, the QD impedance is a constant. In this case, the resulting zero frequency value, and the set of poles and zeros, are listed below:

$$Z_{QD}^{M1}(0) = -L_c\omega_n \tag{5.14}$$

$$p_{QD}^{M1} = \{\varnothing\} \tag{5.15}$$

$$z_{QD}^{M1} = \{\varnothing\} \tag{5.16}$$

4. Z_{QQ} **Impedance:** Finally, the QQ-channel impedance is analyzed. As $Z_{QQ} = Z_{DD}$, then the same zero frequency values and set of poles and zeros are obtained and listed below:

$$Z_{QQ}^{M1}(0) = -r_C \tag{5.17}$$

$$p_{QQ}^{M1} = \{\varnothing\} \tag{5.18}$$

$$z_{QQ}^{M1} = \{-\frac{r_C}{L_C}\} \tag{5.19}$$

5.1.3. Critical Parameters Determination

In Table 5.1, the main values of the characterization of the transfer function plot are summarized, this is, the parameters that describe the asymptotic limits of the small-signal impedances plots.

Table 5.1: M1 Summarized Impedances Critical Values

	Z_{DD}	Z_{DQ}	Z_{QD}	Z_{QQ}
Zero Frequency Value	$Z_{DD}^{M1}(0) = -r_C$	$Z_{DQ}^{M1}(0) = L_c\omega_n$	$Z_{QD}^{M1}(0) = -L_c\omega_n$	$Z_{QQ}^{M1}(0) = -r_C$
Poles	$p_{DD}^{M1} = \{\varnothing\}$	$p_{DQ}^{M1} = \{\varnothing\}$	$p_{QD}^{M1} = \{\varnothing\}$	$p_{QQ}^{M1} = \{\varnothing\}$
Zeros	$z_{DD}^{M1} = \{-\frac{r_C}{L_C}\}$	$z_{DQ}^{M1} = \{\varnothing\}$	$z_{QD}^{M1} = \{\varnothing\}$	$z_{QQ}^{M1} = \{-\frac{r_C}{L_C}\}$

As the modeled inverter corresponds to an ideal voltage source with an output impedance, the impedances plot depend purely of the coupling inductor values. How these impedances affect the Bode diagram are graphically displayed in Figures 5.1-5.4.

1. Z_{DD} **&** Z_{QQ} **Diagrams:** As both DD-channel and QQ-channel diagrams behave equally, they are both analyzed in this item.
   (a) **Magnitude Plot:** The initial value of the magnitude plot is defined purely by $|Z_{DD}^0| = \left|Z_{QQ}^0\right| = r_C$, as shown in Table 5.1. As explained in Section 2.4.3, slope changes occur due to poles and zeros. In this particular case, as there is only one zero and as no poles are present, the entire slope changes are determined by the frequency value of $z_{DD}^{M1} = z_{QQ}^{M1}$, this is, $\omega_{DD}^{z1} = \omega_{QQ}^{z1} = \frac{r_C}{L_C}$.
   (b) **Phase Plot:** As zero frequency value is always negative and no unstable poles nor zeros are present, the initial phase value is always $\phi_{DD}^0 = \phi_{QQ}^0 = 180°$. Same as in the magnitude plot, the frequency slope changes are determined by $\omega_{DD}^{z1} = \omega_{QQ}^{z1}$.

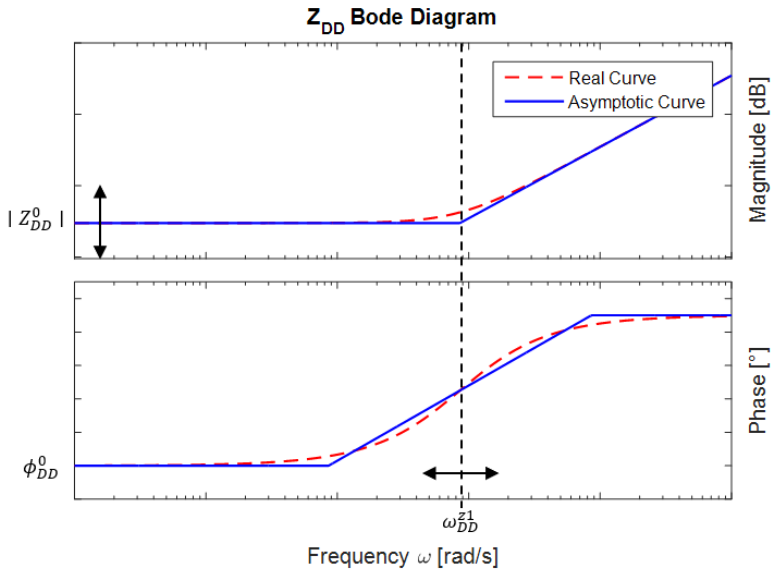

Figure 5.1: Ideal Source Z_{DD} Impedance Bode Diagrams

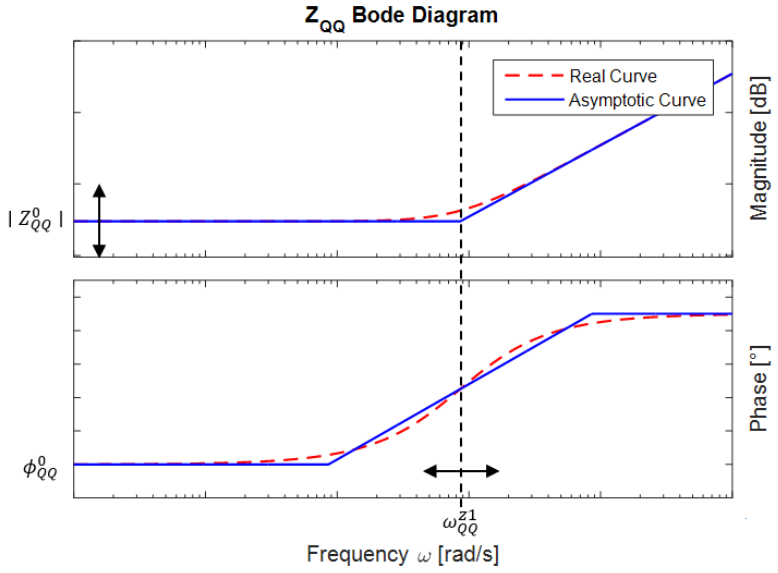

Figure 5.2: Ideal Source Z_{QQ} Impedance Bode Diagrams

2. Z_{DQ} **Diagram:**
   (a) **Magnitude Plot:** In this case, the initial value of the magnitude plot is directly defined by $\left|Z^0_{DQ}\right| = L_c\omega_n$. As neither poles nor zeros are present, no slope changes occurs, i.e. the Bode diagram remains constant.
   (b) **Phase Plot:** The zero frequency value is in this case always positive, hence the phase diagram is represented by a constant line $\phi^0_{DQ} = 0°$.

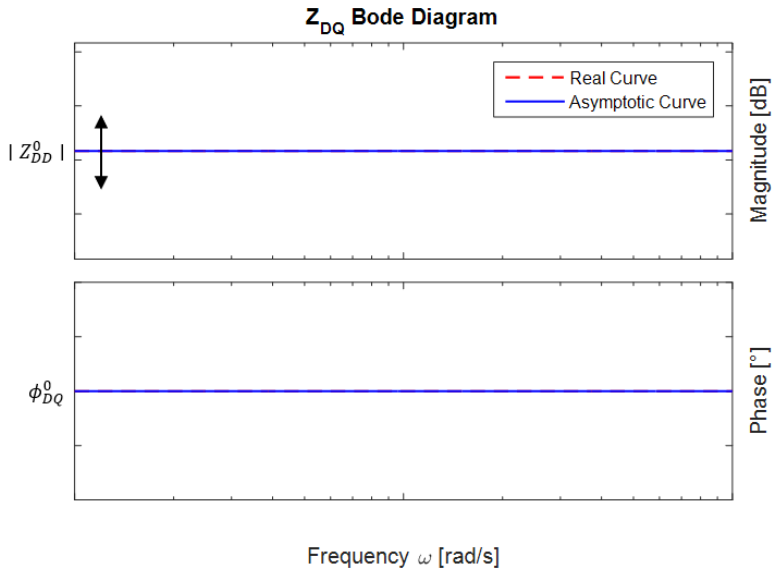

Figure 5.3: Ideal Source Z_{DQ} Impedance Bode Diagrams

3. Z_{QD} **Diagram:**
   (a) **Magnitude Plot:** Same as previous case, the initial value of the magnitude plot is directly defined by $\left|Z^0_{QD}\right| = L_c\omega_n$, remaining constant.
   (b) **Phase Plot:** The only difference between DQ-channel and QD-channel is the sign of the zero frequency value. In consequence, the phase diagram is displaced, resulting in $\phi^0_{QD} = 180°$.

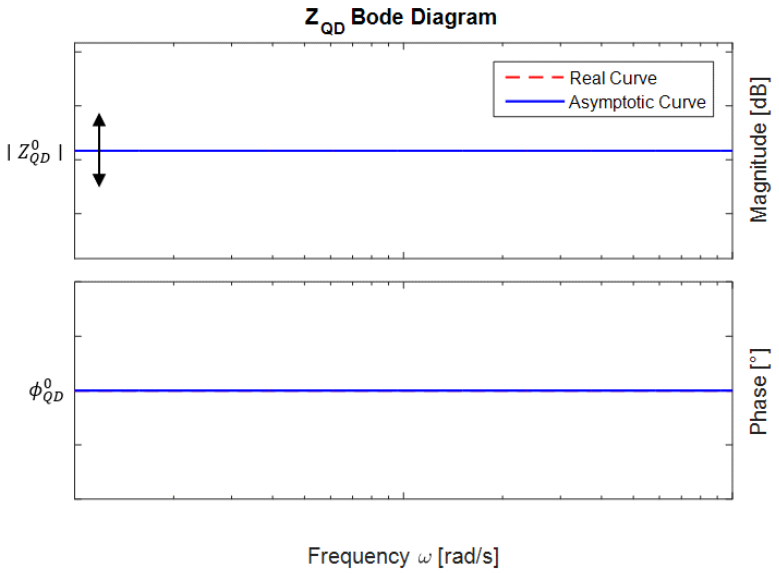

Figure 5.4: Ideal Source Z_{QD} Impedance Bode Diagrams

5.2. M2: Active Power Droop-Controlled Source

5.2.1. Small-Signal Impedance Obtainment

Same as previous case, the small-signal impedance expression is obtained, by considering (4.14)-(4.17). In this case, where (5.5) is also valid, the resulting impedance values are listed in (5.20).

$$
\begin{aligned}
Z_{DD}(s) &= \frac{1}{s + m_p V_n I_{oq}}(-L_C \cdot s^2 - (r_C + L_c V_n I_{oq} m_p) \cdot s + m_p V_n (V_{bQ} \cdot \cos(\overline{\delta}) \\
&+ (I_{od} \cdot \cos(\overline{\delta}) - I_{oq} \cdot \sin(\overline{\delta})) \cdot (r_C \cdot \sin(\overline{\delta}) + L_C(\omega_n - m_p(V_n I_{od} - P_n)) \cdot \cos(\overline{\delta}))) \\
Z_{DQ}(s) &= \frac{1}{s + m_p V_n I_{oq}}(L_C(\omega_n - m_p(V_n I_{od} - P_n)) \cdot s + m_p V_n (V_{bQ} \cdot \sin(\overline{\delta}) \\
&+ (I_{od} \cdot \sin(\overline{\delta}) + I_{oq} \cdot \cos(\overline{\delta})) \cdot (r_C \cdot \sin(\overline{\delta}) + L_C(\omega_n - m_p(V_n I_{od} - P_n)) \cdot \cos(\overline{\delta}))) \\
Z_{QD}(s) &= \frac{1}{s + m_p V_n I_{oq}}(-L_C(\omega_n - m_p(V_n I_{od} - P_n)) \cdot s - m_p V_n (V_{bD} \cdot \cos(\overline{\delta}) \\
&- (I_{od} \cdot \cos(\overline{\delta}) - I_{oq} \cdot \sin(\overline{\delta}))(-r_C \cdot \cos(\overline{\delta}) + L_C \cdot (\omega_n - m_p(V_n I_{od} - P_n)) \cdot \sin(\overline{\delta}))) \\
Z_{QQ}(s) &= \frac{1}{s + m_p V_n I_{oq}}(-L_C \cdot s^2 - (r_C + L_C V_n I_{oq} m_p) \cdot s - m_p V_n (V_{bD} \cdot \sin(\overline{\delta}) \\
&- (I_{od} \cdot \sin(\overline{\delta}) + I_{oq} \cdot \cos(\overline{\delta}))(-r_C \cdot \cos(\overline{\delta}) + L_C(\omega_n - m_p(V_n I_{od} - P_n)) \cdot \sin(\overline{\delta})))
\end{aligned}
\tag{5.20}
$$

In this case, impedance results have algebraically greater complexity, such that the asymptotic Bode limits solving is unpractical. Hence, the small-signal impedance when $\overline{\delta} \approx 0$, considering also (4.10) and (4.11), is presented in (5.21). This corresponds to analyzing the locally-referred small-signal impedance. The validity of this assumption, in order to characterize the globally-referred small-signal impedance of the converter, will be analyzed in next chapter.

$$
\begin{aligned}
Z_{DD}(s) &= \frac{-L_C \cdot s^2 - (r_C + L_c V_n I_{oq} m_p) \cdot s + m_p V_n \left(V_{bQ} + I_{od} L_C \overline{\omega}\right)}{s + m_p V_n I_{oq}} \\
Z_{DQ}(s) &= L_c \overline{\omega} \\
Z_{QD}(s) &= \frac{-L_C \overline{\omega} \cdot s - m_p V_n \left(V_{bD} - I_{od} r_C\right)}{s + m_p V_n I_{oq}} \\
Z_{QQ}(s) &= -\left(r_C + s \cdot L_C\right)
\end{aligned}
\tag{5.21}
$$

where $\overline{\omega}$ corresponds to the operating frequency, resulting from the droop-controlled source.

5.2.2. Bode Plot Analytic Characterization

Similarly to previous models, the critical Bode plot parameters for each DQ-channel are computed.

1. Z_{DD} **Impedance:** Evaluating the corresponding DD-channel equation in (5.21) with $s = 0$, the following result is obtained:

$$
Z_{DD}^{M2}(0) = \frac{V_{bQ} + I_{od} L_C \overline{\omega}}{I_{oq}} \tag{5.22}
$$

In second place, the poles of the transfer function are obtained by solving the equation presented in (5.23).

$$
\begin{aligned}
s + V_n I_{oq} m_p &= 0 \\
\Rightarrow p_{DD}^{M2} &= \{-V_n I_{oq} m_p\}
\end{aligned}
\tag{5.23}
$$

At last, the zeros of the system are obtained, by solving the quadratic equation presented below:

$$
\begin{aligned}
s^2 + \left(\frac{r_C}{L_C} + V_n I_{oq} m_p\right) \cdot s - m_p V_n \left(\frac{V_{bQ}}{L_C} + I_{od} \overline{\omega}\right) &= 0 \\
\Rightarrow z_{DD1,2}^{M2} = \left\{ \frac{-\left(\frac{r_C}{L_C} + V_n I_{oq} m_p\right) \pm \sqrt{\left(\frac{r_C}{L_C} + V_n I_{oq} m_p\right)^2 + 4\left(V_n I_{od} m_p \overline{\omega} + \frac{V_{bQ} V_n m_p}{L_C}\right)}}{2} \right\}
\end{aligned}
\tag{5.24}
$$

2. Z_{DQ} **Impedance:** As no complex frequency s dependency is present, the small-signal transfer function is a constant value. Thus, the zero frequency value corresponds to:

$$Z_{DQ}^{M2}(0) = L_c\overline{\omega} \tag{5.25}$$

As neither poles nor zeros are present, the following empty sets are obtained:

$$p_{DQ}^{M2} = \{\varnothing\} \tag{5.26}$$

$$z_{DQ}^{M2} = \{\varnothing\} \tag{5.27}$$

3. Z_{QD} **Impedance:** First, s is replaced by 0 in order to obtain the zero frequency value of the QD-channel, as follows:

$$Z_{QD}^{M2}(0) = -\frac{V_{bD} - I_{od}r_C}{I_{oq}} \tag{5.28}$$

The set of poles of the transfer function is also obtained by solving the equation below:

$$\begin{aligned} s + V_n I_{oq} m_p &= 0 \\ \Rightarrow p_{QD}^{M2} &= \{-V_n I_{oq} m_p\} \end{aligned} \tag{5.29}$$

Finally, (5.30) is solved, obtaining the zeros of the system.

$$\begin{aligned} -L_C\overline{\omega} \cdot s - m_p V_n (V_{bD} + I_{od} r_C) &= 0 \\ \Rightarrow z_{QD}^{M2} &= \{-\frac{m_p V_n (V_{bD} + I_{od} r_C)}{L_C\overline{\omega}}\} \end{aligned} \tag{5.30}$$

4. Z_{QQ} **Impedance:** As the QQ-channel impedance in this case is the same as in M1, the same critical parameters are obtained, as shown below:

$$Z_{QQ}^{M2}(0) = -r_C \tag{5.31}$$

$$p_{QQ}^{M2} = \{\varnothing\} \tag{5.32}$$

$$z_{QQ}^{M2} = \{-\frac{r_C}{L_C}\} \tag{5.33}$$

Table 5.2: M2 Summarized Impedances Critical Values

	Z_{DD}	Z_{DQ}	Z_{QD}	Z_{DD}
Zero Frequency Value	$Z_{DD}^{M2}(0) = \frac{V_{bQ} + I_{od}L_C\overline{\omega}}{I_{oq}}$	$Z_{DQ}^{M2}(0) = L_c\overline{\omega}$	$Z_{QD}^{M2}(0) = -\frac{V_{bD} - I_{od}r_C}{I_{oq}}$	$Z_{QQ}^{M2}(0) = -r_C$
Poles	$p_{DD}^{M2} = -V_n I_{oq} m_p$	$p_{DQ}^{M2} = \varnothing$	$p_{QD}^{M2} = -V_n I_{oq} m_p$	$p_{QQ}^{M2} = \varnothing$
Zeros	$z_{DD1,2}^{M2} = \frac{-\left(\frac{r_C}{L_C} + V_n I_{oq} m_p\right) \pm \sqrt{\left(\frac{r_C}{L_C} + V_n I_{oq} m_p\right)^2 + 4\left(V_n I_{od} m_p \overline{\omega} + \frac{V_{bQ} V_n m_p}{L_C}\right)}}{2}$	$z_{DQ}^{M2} = \varnothing$	$z_{QD}^{M2} = -\frac{m_p V_n (V_{bD} + I_{od} r_C)}{L_C \overline{\omega}}$	$z_{QQ}^{M2} = -\frac{r_C}{L_C}$

5.2.3. Critical Parameters Determination

In Table 5.2 are summarized the parameters that describe the asymptotic limits of the small-signal impedances plots for this case in particular.

In Figures 5.5-5.8 are displayed the Bode diagrams that describe the transfer functions of the active power droop-controlled inverter. Considering that the active power droop control impacts the frequency dynamics of power inverters, the influence of the active droop control is specially important in the QD-channel, as shown in Figure 5.6. Further details are analyzed below.

1. Z_{DD} **Diagrams:** Firstly, the complexity condition of the corresponding pair of zeros presented in Table 5.2 is determined, by analyzing the discriminant presented in (5.34)

$$\Delta = \left(\frac{r_C}{L_C} + V_n I_{oq} m_p\right)^2 + 4 V_n m_p \left(I_{od}\overline{\omega} + \frac{V_{bQ}}{L_C}\right) \tag{5.34}$$

The critical value of active power P^c that determine the zeros complexity, in terms of the other parameters and operation point, can be obtained. Considering from (4.10) and (4.11) that $P = V_n I_{od}$ and $Q = V_n I_{oq}$, P^c is obtained, as follows:

$$\begin{aligned} \left(\frac{r_C}{L_C} + Q m_p\right)^2 + 4\left(P^c m_p \overline{\omega} + \frac{m_p V_n V_{bQ}}{L_C}\right) = 0 \\ \Rightarrow P^c = -\frac{1}{m_p \overline{\omega}}\left(\frac{1}{4}\left(\frac{r_C}{L_C} + Q m_p\right)^2 + \frac{m_p V_n V_{bQ}}{L_C}\right) \end{aligned} \tag{5.35}$$

Hence, $P > P^c$, this is, $\Delta > 0$, yields to a pair of real zeros. Otherwise, the zeros of the transfer function are complex conjugates. Finally, in the case when $P = P^c$ ($\Delta = 0$), a zero of multiplicity 2 is obtained.

Note that P^c is always negative as $V_{bQ} \approx 0$, thus only when the inverter is acting as a sink, complex poles can appear. In that case, as stated in Section 2.4.3, a resonance peak might show up, depending on the value of ξ, as analyzed further below.

- **Real Zeros** As stated before, a pair of real poles is obtained when $P > P^c$. If the stated condition is held, then $z_{DD1,2}^{M2}$ can be rewritten as follows:

$$z_{DD1,2}^{M2} = \left\{ -\frac{1}{2}\left(\frac{r_C}{L_C} + V_n I_{oq} m_p\right) \pm \frac{1}{2}\sqrt{\left|\left(\frac{r_C}{L_C} + V_n I_{oq} m_p\right)^2 + 4V_n m_p\left(I_{od}\overline{\omega} + \frac{V_{bQ}}{L_C}\right)\right|}\right\}$$
$$= \left\{ -\frac{1}{2}\left(\frac{r_C}{L_C} + Q m_p\right) \pm \frac{1}{2}\sqrt{\left(\frac{r_C}{L_C} + Q m_p\right)^2 + 4m_p\left(P\overline{\omega} + \frac{V_n V_{bQ}}{L_C}\right)}\right\} \tag{5.36}$$

Hence, a critical active power P_+^c can be defined to study the existence of a positive zero. From (5.36), it is clear that:

$$\begin{aligned} P_+^c\overline{\omega} + \frac{V_n V_{bQ}}{L_C} &= 0 \\ \Rightarrow P_+^c &= -\frac{V_n V_{bQ}}{\overline{\omega} L_C} \end{aligned} \tag{5.37}$$

Therefore, considering that this case assumes $P > P^c$, when $P > P_+^c$ a pair of positive and negative zero is obtained. Otherwise, when $P < P_+^c$, a pair of negative zeros (if $\left(\frac{r_C}{L_C} + Q m_p\right) > 0$) or a pair of positive zeros (if $\left(\frac{r_C}{L_C} + Q m_p\right) < 0$) is obtained. On the other hand, if $P = P_+^c$, a negative zero and a zero in the origin are present.

- **Complex Conjugates Zeros** Assuming that $P < P^c$, $z_{DD1,2}^{M2}$ can be rewritten as follows:

$$z_{DD1,2}^{M2} = \left\{ -\frac{1}{2}\left(\frac{r_C}{L_C} + V_n I_{oq} m_p\right) \pm j \cdot \frac{1}{2}\sqrt{\left|\left(\frac{r_C}{L_C} + V_n I_{oq} m_p\right)^2 + 4V_n m_p\left(I_{od}\overline{\omega} + \frac{V_{bQ}}{L_C}\right)\right|}\right\} \tag{5.38}$$

As $\xi = -\omega_R/\omega_n'$, and considering that $\omega_n' = \sqrt{\omega_R^2 + \sigma^2}$, expressions for ω_R and σ are obtained and presented below. Note that, in this case, ω_n' corresponds to the natural frequency of the oscillations associated to the zeros of the system and must not be confused with the rated frequency of the inverter.

$$\omega_R = -\frac{1}{2}\left(\frac{r_C}{L_C} + Q m_p\right) \tag{5.39}$$

$$\sigma = \sqrt{\frac{1}{4}\left|\left(\frac{r_C}{L_C} + Q m_p\right)^2 + m_p P\overline{\omega} + \frac{V_n V_{bQ}}{L_C}\right|} \tag{5.40}$$

Hence,

$$\omega_n' = \sqrt{\frac{1}{4}\left(\frac{r_C}{L_C} + Qm_p\right)^2 + \frac{1}{4}\left|\left(\frac{r_C}{L_C} + Qm_p\right)^2 + m_p P\overline{\omega} + \frac{V_n V_{bQ}}{L_C}\right|} \tag{5.41}$$

As complex zeros are being analyzed, (5.41) can be rewritten as follows:

$$\begin{aligned}\omega_n' = \sqrt{\frac{1}{4}\left(\frac{r_C}{L_C} + Qm_p\right)^2 - \frac{1}{4}\left(\left(\frac{r_C}{L_C} + Qm_p\right)^2 + m_p P\overline{\omega} + \frac{V_n V_{bQ}}{L_C}\right)} \\ \Rightarrow \omega_n' = \sqrt{-(m_p P\overline{\omega} + \frac{V_n V_{bQ}}{L_C})}\end{aligned} \tag{5.42}$$

Note that, when $P < P^c$, it is always true that $(m_p P\overline{\omega} + \frac{m_p V_n V_{bQ}}{L_C}) \leq 0$. Hence, the calculated frequency ω_n' is always a real positive.

Then, the damping factor ξ can be obtained as follows.

$$\xi = -\frac{(\frac{r_C}{L_C} + Qm_p)}{2(m_p P\overline{\omega} + \frac{m_p V_n V_{bQ}}{L_C})} \tag{5.43}$$

In Figure 5.5 is firstly summarized the critical parameters sensibility, describing how they affect the Bode diagram of the *DD*-channel small-signal impedance.

(a) **Magnitude Plot:** As presented in previous sections, the initial value of the magnitude plot depends on the magnitude of the zero frequency value presented in (5.22), such that $|Z_{DD}^0| = \left|\frac{(V_{bQ} + I_{od} L_C \overline{\omega})}{I_{oq}}\right|$. This value increases as V_{bQ}, I_{od}, L_C or $\overline{\omega}$ increase. On the other hand, this value decreases as I_{oq} increases.

The break points, as stated previously, dictates the slope changes. In this case, an increase in the curve slope is presented in $\omega_{DD}^{p1} = V_n I_{oq} m_p$. Decreases in the slope are determined by the zeros. If the zeros are real, then from (5.36):

$$\begin{aligned}\omega_{DD}^{z1} &= -\frac{1}{2}(\frac{r_C}{L_C} + Qm_p) + \frac{1}{2}\sqrt{(\frac{r_C}{L_C} + Qm_p)^2 + 4m_p(P\overline{\omega} + \frac{V_n V_{bQ}}{L_C})} \\ \omega_{DD}^{z2} &= -\frac{1}{2}(\frac{r_C}{L_C} + Qm_p) - \frac{1}{2}\sqrt{(\frac{r_C}{L_C} + Qm_p)^2 + 4m_p(P\overline{\omega} + \frac{V_n V_{bQ}}{L_C})}\end{aligned} \tag{5.44}$$

If the zeros are otherwise complex, then from Equation 5.42:

$$\omega_{DD}^{z1} = \omega_{DD}^{z2} = \sqrt{-(m_p P\overline{\omega} + \frac{V_n V_{bQ}}{L_C})} \tag{5.45}$$

A resonance peak might appear in this case and depends purely on the damping factor ξ, as presented in Figure 2.12.

(b) **Phase Plot:** In this case, considering instructions presented in Section 2.4.3, two phase initial values are possible, depending on sign of the zero frequency value and the number of unstable poles and zeros. Below are the conditions of the possible unstable poles and zeros.

i. **Poles:**

A. Single Positive Pole:

- $Q < 0$

ii. **Zeros:**

A. Single Positive Zero:

- $P < P^c$ & $(\frac{r_C}{L_C} + Qm_p) < 0$
- $P > P^c$ & $P > P^c_+$

B. Double Positive Zero:

- $P^c < P < P^c_+$ & $(\frac{r_C}{L_C} + Qm_p) < 0$

Therefore, if n_z and n_p are the number of unstable zeros and poles, respectively, then:

(a) If $n_z + n_p$ is an even number, then the initial phase value corresponds to $\phi^0_{DD} = 0°$ if $Z^{M2}_{DD}(0) > 0$ and 180° if $Z^{M2}_{DD}(0) < 0$.

(b) On the other hand, if $n_z + n_p$ is an odd number, then the initial phase value corresponds to $\phi^0_{DD} = 180°$ if $Z^{M2}_{DD}(0) > 0$ and 0° if $Z^{M2}_{DD}(0) < 0$.

Similarly as in the magnitude plot, the slope changes depending on the values of ω^{p1}_{DD}, ω^{z1}_{DD} and ω^{z2}_{DD}. When complex zeros are present, ξ determines the transition real slope between the initial and final phase values, as presented in Figure 2.12.

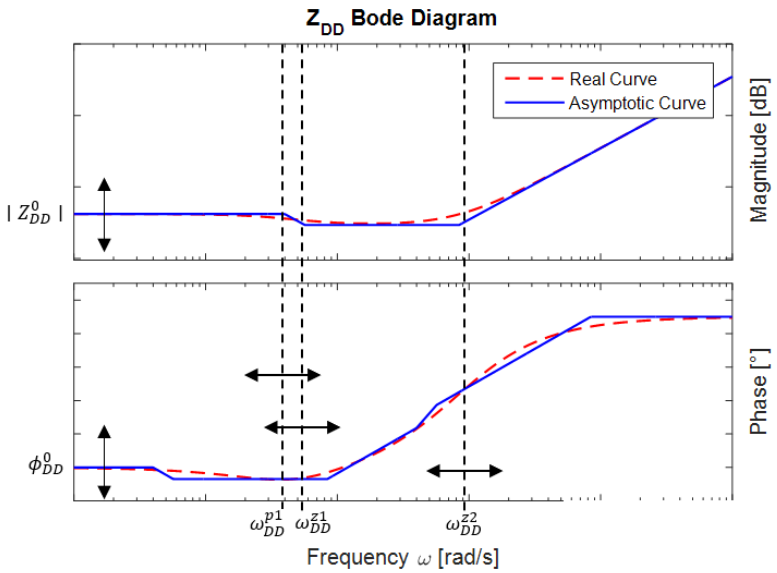

Figure 5.5: Active Power Droop Controlled Inverter Z_{DD} Impedance Bode Diagrams

2. Z_{DQ} **Diagram:**

(a) **Magnitude Plot:** In this case, as displayed in 5.6 and similarly to the DQ-channel impedance of the ideal source model, neither zeros nor poles are present. The initial value of the magnitude plot depends directly on $\left|Z^0_{DQ}\right| = L_c\overline{\omega}$.

(b) **Phase Plot:** The phase angle is always $\phi^0_{DQ} = 0°$, as $L_c\overline{\omega}$ is always positive.

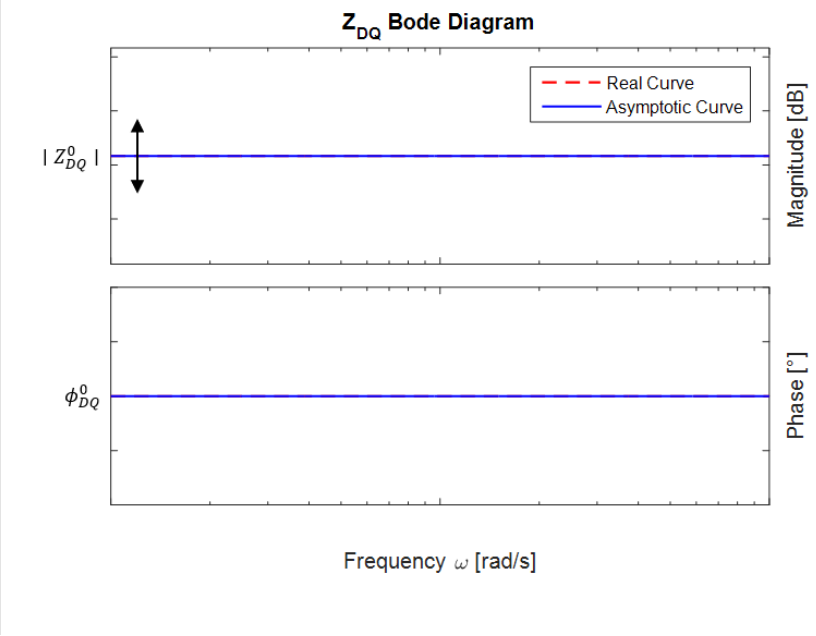

Figure 5.6: Active Power Droop Controlled Inverter Z_{DQ} Impedance Bode Diagrams

3. Z_{QD} **Diagram:**

(a) **Magnitude Plot:** The initial value is determined in this channel by the absolute value $\left|Z^0_{QD}\right| = \frac{V_{bD} - I_{od}r_C}{I_{oq}}$, as shown in Figure 5.7. The decrease in the slope occurs in frequency $\omega^{p1}_{QD} = |V_n I_{oq} m_p|$ and the increase occurs in $\omega^{z1}_{QD} = \left|m_p V_n \frac{V_{bQ} + I_{od}r_C}{L_C\overline{\omega}}\right|$.

(b) **Phase Plot:** Similar as presented in DD-channel, from (5.29) and (5.30) the conditions of the possible positive poles and zeros are obtained and listed below:

i. **Poles:**

A. Single Positive Pole:

- $Q < 0$

ii. **Zeros:**

A. Single Positive Zero:

- $(V_n V_{bD} + Pr_c) < 0$

Then, same as in DD-Channel, considering n_z and n_p as the number of unstable zeros and poles, respectively:

i. If $n_z + n_p$ is an even number, then the initial phase value is $\phi^0_{QD} = 0°$ if $Z^{M2}_{QD}(0) > 0$ and $\phi^0_{QD} = 180°$ if $Z^{M2}_{QD}(0) < 0$.

ii. If $n_z + n_p$ is an odd number, then the initial phase value is $\phi^0_{QD} = 180°$ if $Z^{M2}_{QD}(0) > 0$ and $\phi^0_{QD} = 0°$ if $Z^{M2}_{QD}(0) < 0$.

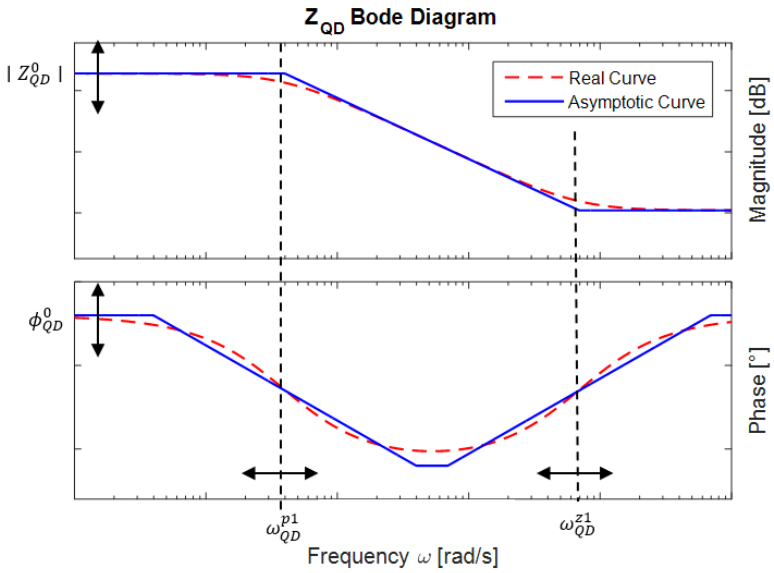

Figure 5.7: Active Power Droop Controlled Inverter Z_{QD} Impedance Bode Diagrams

4. Z_{QQ} **Diagram:** Finally, as here the QQ-channel impedance behaves the same as in the ideal source model, the same conclusions are made.

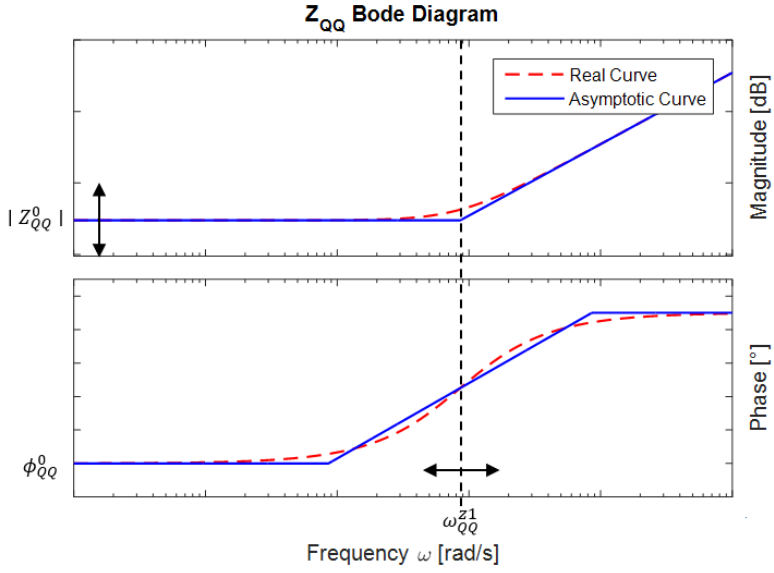

Figure 5.8: Active Power Droop Controlled Inverter Z_{QQ} Impedance Bode Diagrams

5.3. M3: Reactive Power Droop-Controlled Source

5.3.1. Small-Signal Impedance Obtainment

Finally, M3 is analyzed. In the first place and similar to previous case, the small-signal impedances are obtained, computing (4.23)-(4.26), and presented below:

$$Z_{DD}(s) = -L_C \cdot s - r_C - \frac{n_q V_n \cdot \sin(\overline{\delta}) \cdot \cos(\overline{\delta})}{(I_{oq} n_q - 1)^2} \tag{5.46}$$

$$Z_{DQ}(s) = L_C \omega_n + \frac{n_q V_n \cdot \cos^2(\overline{\delta})}{(I_{oq} n_q - 1)^2} \tag{5.47}$$

$$Z_{QD}(s) = -L_C \omega_n + \frac{n_q V_n \cdot \sin^2(\overline{\delta})}{(I_{oq} n_q - 1)^2} \tag{5.48}$$

$$Z_{QQ}(s) = -L_C \cdot s - rc + \frac{n_q V_n \cdot \sin(\overline{\delta}) \cdot \cos(\overline{\delta})}{(I_{oq} n_q - 1)^2} \tag{5.49}$$

With the intention of analogically analyze the reactive power droop-controlled with the active power droop-controlled inverter, $\overline{\delta}$ is again assumed to be zero, this is, the locally-referred small-signal impedances are computed and presented in (5.50).

$$\begin{aligned} Z_{DD}(s) &= -(r_C + s \cdot L_C) \\ Z_{DQ}(s) &= L_c \omega_n + \frac{n_q V_n}{(I_{oq} n_q - 1)^2} \\ Z_{QD}(s) &= -L_c \omega_n \\ Z_{QQ}(s) &= -(r_C + s \cdot L_C) \end{aligned} \tag{5.50}$$

5.3.2. Bode Plot Analytic Characterization

Same as before, the critical Bode plot parameters are obtained.

1. Z_{DD} **Impedance:** In this case, Z_{DD} impedance is the same as in M1. Hence, for DD-channel, the same critical values are obtained, as presented in (5.51)-(5.53).

$$Z_{DD}^{M3}(0) = -r_C \tag{5.51}$$

$$p_{DD}^{M3} = \{\varnothing\} \tag{5.52}$$

$$z_{DD}^{M3} = \{-\frac{r_C}{L_C}\} \tag{5.53}$$

2. Z_{DQ} **Impedance:** Same as in M1, no complex frequency s dependency is present. Hence the zero frequency value corresponds to:

$$Z_{DQ}^{M3}(0) = L_c\omega_n + \frac{n_q V_n}{(I_{oq} n_q - 1)^2} \tag{5.54}$$

In consequence, neither poles or zeros are present, as shown in (5.55) and (5.56)

$$p_{DQ}^{M3} = \{\varnothing\} \tag{5.55}$$

$$z_{DQ}^{M3} = \{\varnothing\} \tag{5.56}$$

3. Z_{QD} **Impedance:** Considering that QD-channel impedance is the same as in M1, the computed zero frequency value, poles and zeros are listed below:

$$Z_{QD}^{M3}(0) = L_c\omega_n \tag{5.57}$$

$$p_{QD}^{M3} = \{\varnothing\} \tag{5.58}$$

$$z_{QD}^{M3} = \{\varnothing\} \tag{5.59}$$

Table 5.3: M3 Summarized Impedances Critical Values

	Z_{DD}	Z_{DQ}	Z_{QD}	Z_{QQ}
Zero Frequency Value	$Z_{DD}^{M3}(0) = -r_C$	$Z_{DQ}^{M3}(0) = L_c\omega_n + \frac{n_q V_n}{(I_{oq} n_q - 1)^2}$	$Z_{QD}^{M3}(0) = -L_c\omega_n$	$Z_{QQ}^{M3}(0) = -r_C$
Poles	$p_{DD}^{M3} = \varnothing$	$p_{DQ}^{M3} = \varnothing$	$p_{QD}^{M3} = \varnothing$	$p_{QQ}^{M3} = \varnothing$
Zeros	$z_{DD}^{M3} = -\frac{r_C}{L_C}$	$z_{DQ}^{M3} = \varnothing$	$z_{QD}^{M3} = \varnothing$	$z_{QQ}^{M3} = -\frac{r_C}{L_C}$

4. Z_{QQ} **Impedance:** As the DD-channel and QQ-channel small-signal impedances are the same in this model, then the critical parameters are the same as in (5.51)-(5.53), as follows:

$$Z_{QQ}^{M3}(0) = -r_C \tag{5.60}$$

$$p_{QQ}^{M3} = \{\varnothing\} \tag{5.61}$$

$$z_{QQ}^{M3} = \{-\frac{r_C}{L_C}\} \tag{5.62}$$

5.3.3. Critical Parameters Determination

In Table 5.3 are summarized the computed critical values of M3.

In Figures 5.9-5.12 are displayed the Bode diagrams of the transfer functions of the reactive power droop-controlled inverter.

1. Z_{DD}**,** Z_{QD} **&** Z_{QQ} **Diagrams:** As only the DQ-channel impedance behaves differently than the presented in the ideal source model, the conclusions for these channels are the same.
2. Z_{DQ} **Diagram:** In this case, only a small change is presented in the magnitude Bode diagram initial value, in comparison with the ideal source model, as displayed in Figure 5.12.
   (a) **Magnitude Plot:** In this case, besides $L_c\omega_n$, the term $\frac{n_q V_n}{(I_{oq} n_q - 1)^2}$ must be taken into account when computing the initial magnitude value, as $\left|Z_{DQ}^0\right| = L_c\omega_n + \frac{n_q V_n}{(I_{oq} n_q - 1)^2}$. As neither poles nor zeros are present, the curve remains constant.
   (b) **Phase Plot:** In this case, as both $L_c\omega_n$ and $\frac{n_q V_n}{(I_{oq} n_q - 1)^2}$ expressions are positive, the frequency response phase angle is always $\phi_{DQ}^0 = 0$.

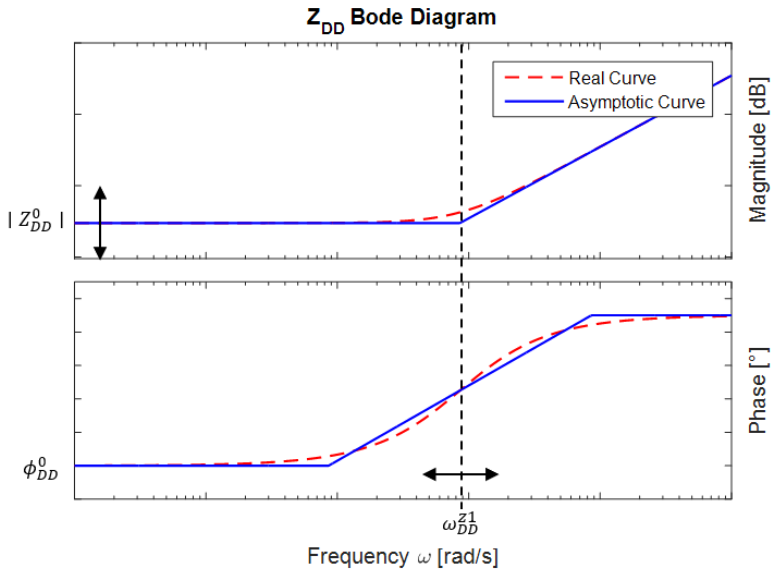

Figure 5.9: Reactive Power Droop Controlled Inverter Z_{DD} Impedance Bode Diagrams

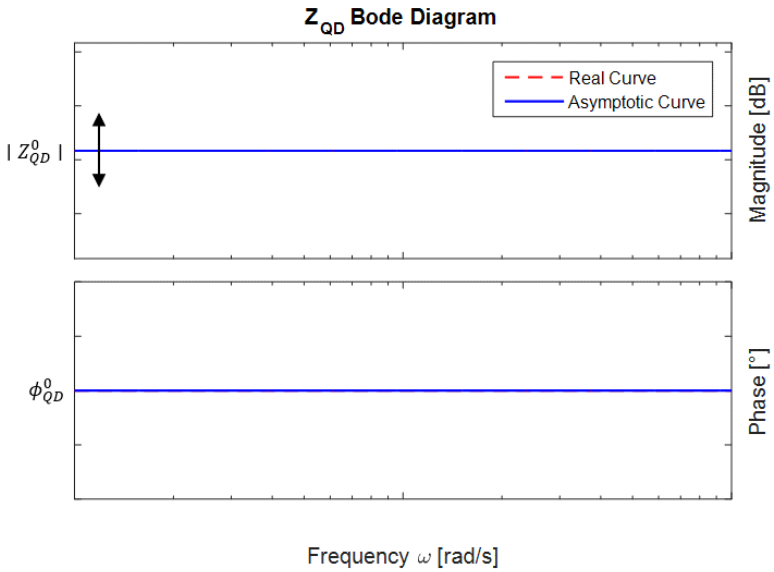

Figure 5.10: Active Power Droop Controlled Inverter Z_{QD} Impedance Bode Diagrams

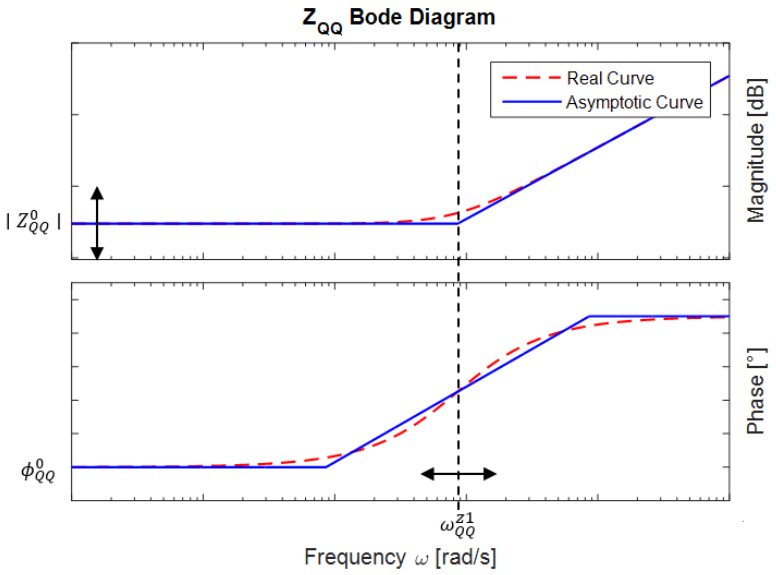

Figure 5.11: Reactive Power Droop Controlled Inverter Z_{QQ} Impedance Bode Diagrams

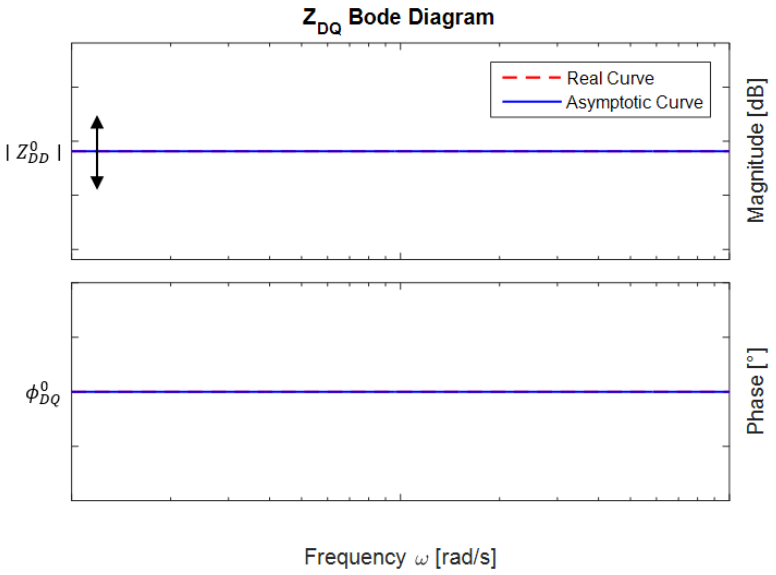

Figure 5.12: Reactive Power Droop Controlled Inverter Z_{DQ} Impedance Bode Diagrams

5.4. Summary

In Table 5.4 are summarized the critical parameters that defines the asymptotic limits of the small-signal impedances of the simplified models.

Table 5.4: Critical Parameters Summary

Channel	Asymptotic Limits Definition	M1	M2	M3
DD-Channel	$\|Z^0_{DD}\|$	r_C	$\left\|\frac{(V_{bQ}+I_{od}L_C\overline{\omega})}{I_{oq}}\right\|$	r_C
	ϕ^0_{DD}	180^o	even n_z+n_p: $0^o(Z^{M2}_{DD}(0)>0)$; $180^o(Z^{M2}_{DD}(0)<0)$ odd n_z+n_p: $180^o(Z^{M2}_{DD}(0)>0)$; $0^o(Z^{M2}_{DD}(0)<0)$	180^o
	ω^{zi}_{DD}	$\frac{r_C}{L_C}$	$\frac{1}{2}(\frac{r_C}{L_C}+V_nI_{oq}m_p)\pm\frac{1}{2}\sqrt{(\frac{r_C}{L_C}+V_nI_{oq}m_p)^2+4m_p(V_nI_{od}\overline{\omega}+\frac{V_nV_{bQ}}{L_C})}$ $(P>P^C)$ $\sqrt{-(m_pV_nI_{od}\overline{\omega}+\frac{V_nV_{bQ}}{L_C})}$ $(P<P^C)$	$\frac{r_C}{L_C}$
	ω^{pi}_{DD}	-	$V_nI_{oq}m_p$	-
	ξ	-	$-\frac{(\frac{r_C}{L_C}+V_nI_{oq}m_p)}{2(m_pV_nI_{od}\overline{\omega}+\frac{m_pV_nV_{bQ}}{L_C})}$ $(P<P^C)$	-
DQ-Channel	$\|Z^0_{DQ}\|$	$L_C\omega_n$	$L_C\omega_n$	$L_C\overline{\omega}$
	ϕ^0_{DQ}	0^o	0^o	0^o
	ω^{zi}_{DQ}	-	-	-
	ω^{pi}_{DQ}	-	-	-
QD-Channel	$\|Z^0_{QD}\|$	$L_C\omega_n$	$\left\|\frac{V_{bD}-I_{od}r_C}{I_{oq}}\right\|$	$L_C\omega_n$
	ϕ^0_{QD}	180^o	even n_z+n_p: 0^o $(Z^{M2}_{QD}(0)>0)$; 180^o $(Z^{M2}_{QD}(0)<0)$ odd n_z+n_p: 180^o $(Z^{M2}_{QD}(0)>0)$; 0^o $(Z^{M2}_{QD}(0)<0)$	180^o
	ω^{zi}_{QD}	-	$m_pV_n\frac{V_{bQ}+I_{od}r_C}{L_C\overline{\omega}}$	-
	ω^{pi}_{QD}	-	$V_nI_{oq}m_p$	-
QQ-Channel	$\|Z^0_{QQ}\|$	r_C	r_C	r_C
	ϕ^0_{QQ}	180^o	180^o	180^o
	ω^{zi}_{QQ}	$\frac{r_C}{L_C}$	$\frac{r_C}{L_C}$	$\frac{r_C}{L_C}$
	ω^{pi}_{QQ}	-	-	-

Chapter 6

Numerical Assessment

In this chapter, a numerical assessment is carried through, in order to graphically contrast the different models and to test the validity of the previous determined critical parameters, as stated in Chapter 3.

6.1. Study Case Definition

As presented in Chapter 3, the study case is defined in order to select a proper operating point to assess the developed models. For this purpose, real operating points from a field microgrid will be used. This microgrid is described below.

The 'Huatacondo' project is a renewable energy-based AC microgrid conceived for an isolated small village in the Atacama Desert in the North of Chile. Currently, it provides 24 hours service. For most of the day, the energy is provided by a photovoltaic (PV) array and a battery energy storage system (BESS). Its structure is presented in Figure 6.1. It is formed by 11 busbars, predominantly resistive lines and the aforementioned PV and BESS arrays, besides a diesel generation unit.

The PV converter is built as a Current Source Converter (CSC) and the BESS corresponds to a Voltage Source Converter (VSC), with 40 kVA and 30 kVA capacity, respectively. The PV array is controlled as a grid-feeding converter and the BESS array as a grid-supporting converter. The latter is the element under study and its internal structure corresponds to the one presented in Section 2.2.2.

As the real parameters of the BESS components are not available, the same parameters of [22] are assumed. Furthermore, the droop control parameters are selected based on (2.3), as presented in Table 6.1.

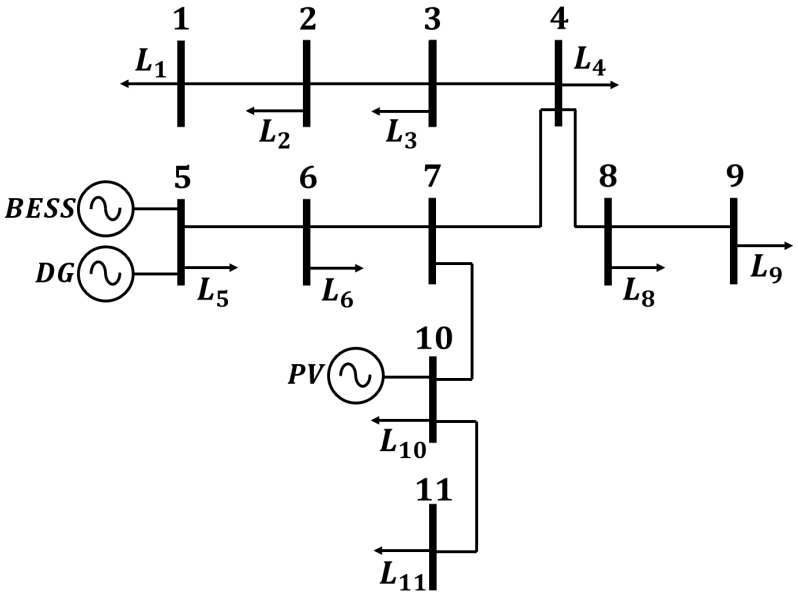

Figure 6.1: Huatacondo Grid

Table 6.1: Droop-Controlled Inverter Internal Parameters

Parameter	**Value**	**Parameter**	**Value**
m_p	$9e-4$	n_q	$1{,}3e-4$
L_F	1,35 mH	ω_c	31,41 rad/s
r_F	0,1 Ω	K_{pv}	0,05
C_F	50 μF	K_{iv}	390
L_C	0,35 mH	K_{pc}	10,5
r_C	0,03 Ω	K_{ic}	$16e3$

The Huatacondo microgrid has several measurement units. In particular, a Schneider PM750 equipment is located between the BESS and busbar 5, measuring line-to-line voltage magnitude, active and reactive power, and frequency. The measurements are uploaded instantly to an online server. The available data covers from 13-6-2017 to 17-12-2018, with minute resolution.

Firstly, the corrupted data are removed, this is, periods where no data was measured due to communication problems or technical issues, leaving 518000 available operating points.

Once the final points are selected, the centroid of the operating point is obtained, by performing a k-means clustering with $k = 1$ and then selecting the operating point with minimum distance to the single cluster centroid. Furthermore, the minima and maxima of all the measured variables are obtained. These results are summarized in Table 6.2.

Note that, as the diesel generator is selected as the slack machine and it is located in the same busbar, the Q-axis voltage on the inverter is always zero. Furthermore, currents are referred to the local reference frame and voltages to the global reference frame, as required

Table 6.2: Study Case Operating Points

Variable	Symbol	Units	Centroid	Minimum	Maximum
D-axis Voltage	V_{bD}	[V]	384.6918	364.5932	445.2113
Q-axis Voltage	V_{bQ}	[V]	0	0	0
d-axis Current	I_{od}	[A]	-4.4336	-44.9347	65.4753
q-axis Current	I_{oq}	[A]	11.6271	-4.684	37.4849
Frequency	f	[Hz]	49.9709	47.0312	51.9954

by the models.

6.2. Sensitivity Analysis

In order to realize the sensitivity analysis, the small-signal impedances of both simplified and advanced models are needed. As analytically obtaining the small-signal impedances of M5 and M6 would demand excessive computational resources (their linearized models have 11 and 13 states respectively), the linearized matrices are first assessed in the desired operating point and then the small-signal impedances are computed as shown in (5.1)-(5.6).

The absence of the LC-filter in models M1 to M4 generates an electrical dependency between the variables I_{odq} and V_{bdq}. Therefore, with the objective of contrasting all the models under equal conditions, this dependency is obviated when evaluating the models in the study case operating points and when performing the sensitivity analysis. Furthermore, in this case δ is again assumed to be 0. The validity of this assumption will be studied later, by sweeping the value of δ in order to analyze the impact of the changes in the small-signal impedance of the final full model.

As stated before, sensitivity analysis is performed on the critical parameters obtained in Chapter 5, based on the values presented in Table 6.2. Furthermore, output inductor values r_C and L_C, as well as droop parameters m_p and n_q, are also swept. The reason for the latter is that the small-signal impedance also depends on those values. The sweep ranges of these parameters are selected based on the rated values, defining an arbitrary range from 50 % to 150 % of the rated value for the sweep.

Thus, the sensitivity parameters are introduced in (6.1). The centroid of the operating points shown in Table 6.2 will be used as the base operating point.

$$v = \begin{bmatrix} m_p & n_q & I_{od} & I_{oq} & V_{bD} & \overline{\omega} & r_C & L_C \end{bmatrix} \tag{6.1}$$

6.2.1. Comparison of Models

In this section, each model is evaluated at the base operating point and then compared to each other in Figures 6.2-6.5, in order to progressively analyze the effects of each additional element incorporated in the models.

Asymptotic Limits

For M1, M2, and M3, based on the results from Chapter 5, the expected asymptotic curves are obtained. Only the asymptotic boundaries of M2 and M3 are graphed, as both incorporate the effects of M1. The black continuous line corresponds to the asymptotic boundaries determined by M2 and the dashed black line corresponds to the boundaries determined by M3.

Note that in this case, $P^c = -7{,}119 \cdot 10^3\ W$. Furthermore, $P^c_+ = -0{,}2002\ W$. As in this case, computing for M2, $P = V_n I_{od} = -1{,}6894 \cdot 10^3\ W$, then $P^c < P < P^c_+$. Considering also that, for M2, $(\frac{r_C}{L_C} + Qm_p) = 89{,}7018 > 0$ then a pair of negative zeros besides a single pole are present in DD-channel asymptotic curve of M2, as expected from Section 5.2.

M1, M2 and M3

M1, M2, and M3 follows their corresponding asymptotic line, as expected. Note that the curves of M1 and M3 overlap in both DD, QD and QQ-channels. Furthermore, the curves of M1 and M2 overlap in DQ-channel.

M4

By considering both active and reactive droop controls with neither LC-filter nor current and voltage control, major deviations in the DD and QQ-channels, specially in low frequencies, are present. In channels DQ and QD, the resulting small-signal impedance tend to follow the M3 and M2 asymptotic curves, respectively.

M5

The addition of the LC filter with the internal voltage and current controls generates a resonance peak in every channel near the frequency $\omega = \frac{1}{2\pi\sqrt{r_C L_C}}$, affecting both magnitude and angle curves. Furthermore, in this particular case the low-frequency effects of the active-power droop controller are present in both DD and QQ-channels magnitudes, but highly attenuated. A deviation is also presented in the DQ-channel magnitude, converging to the asymptotic curves only past the LCL-filter resonance peak. A major deviation in the phase angle graph is induced by the resonance peak.

M6

Finally, by considering the power measuring filter, only DQ and QD-channel impedances are affected in comparison to the previous model. In the DQ-channel, the magnitude curve converges at lower frequency to the active droop-driven asymptotic line. In the QD-channel by the other hand, a resonance peak near $\omega = 2\pi \cdot 10$ is presented, altering the slope in the magnitude graph.

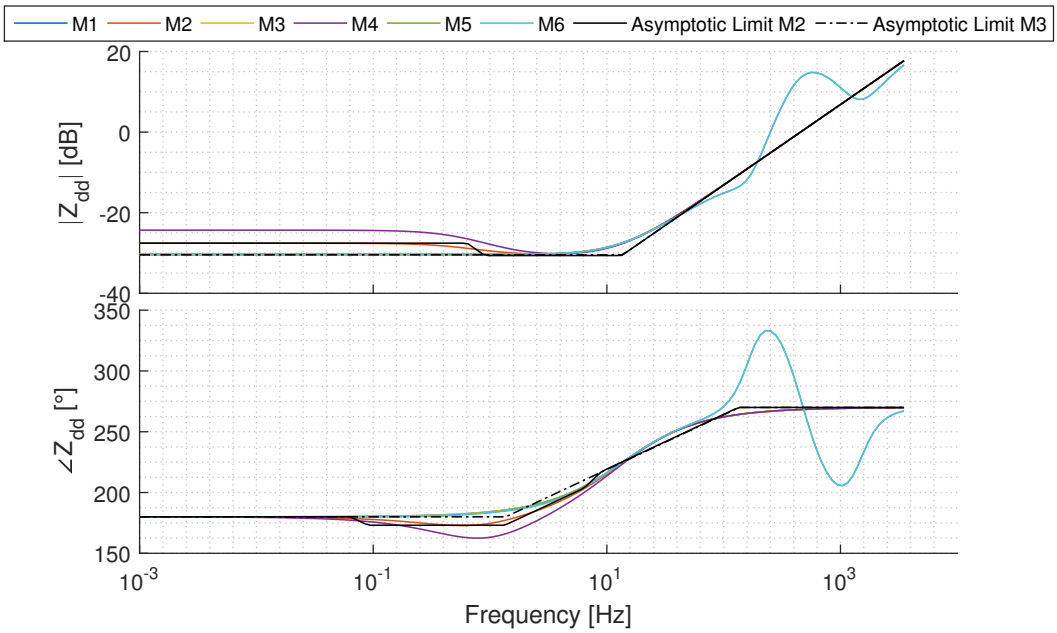

Figure 6.2: DD-Channel Impedances: Base Case.

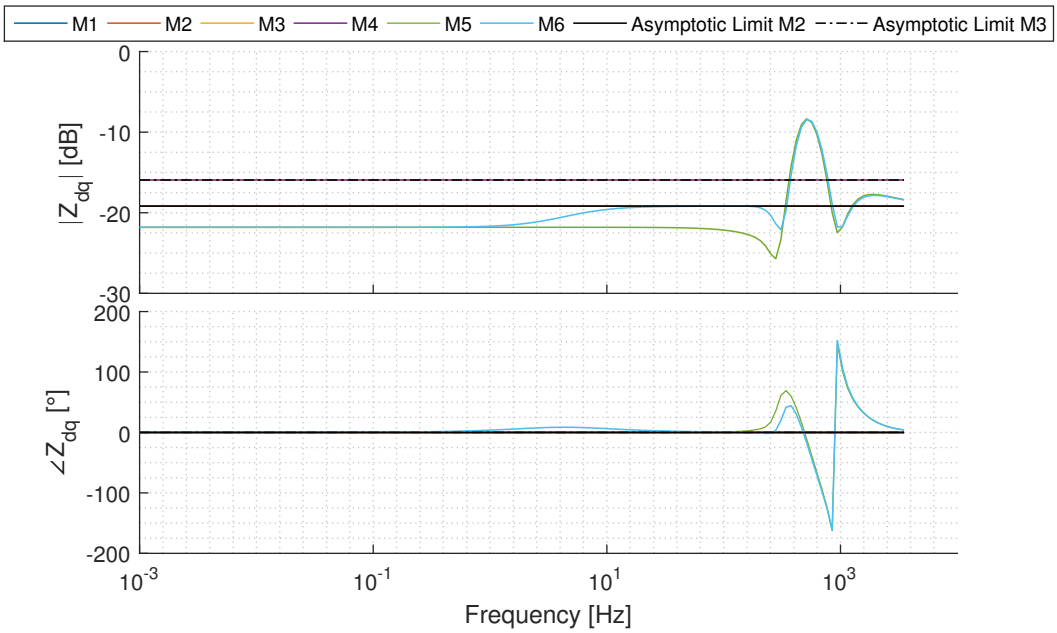

Figure 6.3: DQ-Channel Impedances: Base Case.

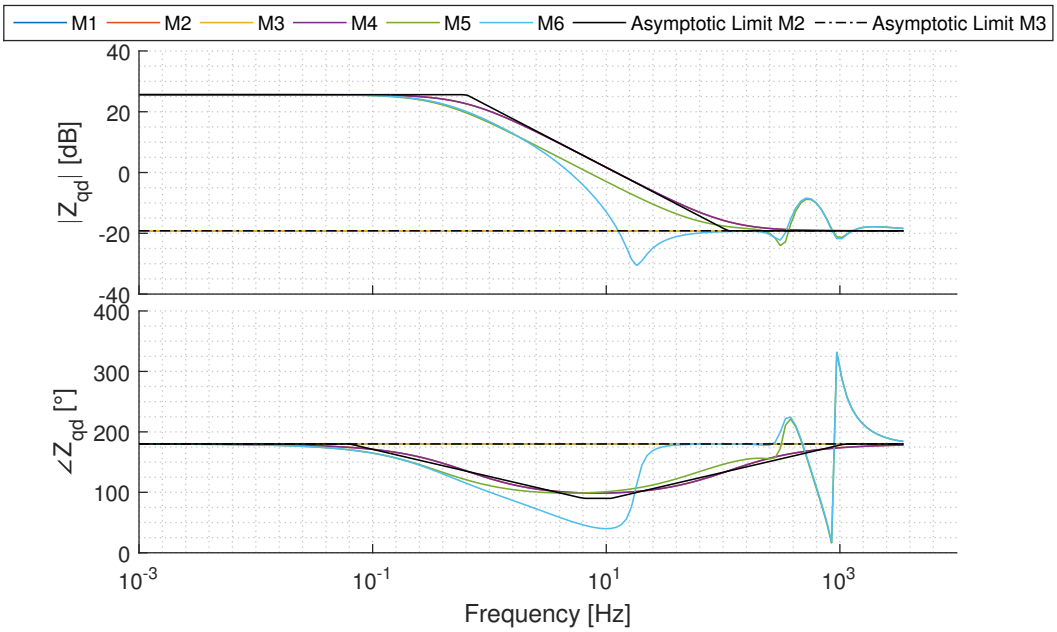

Figure 6.4: QD-Channel Impedances: Base Case.

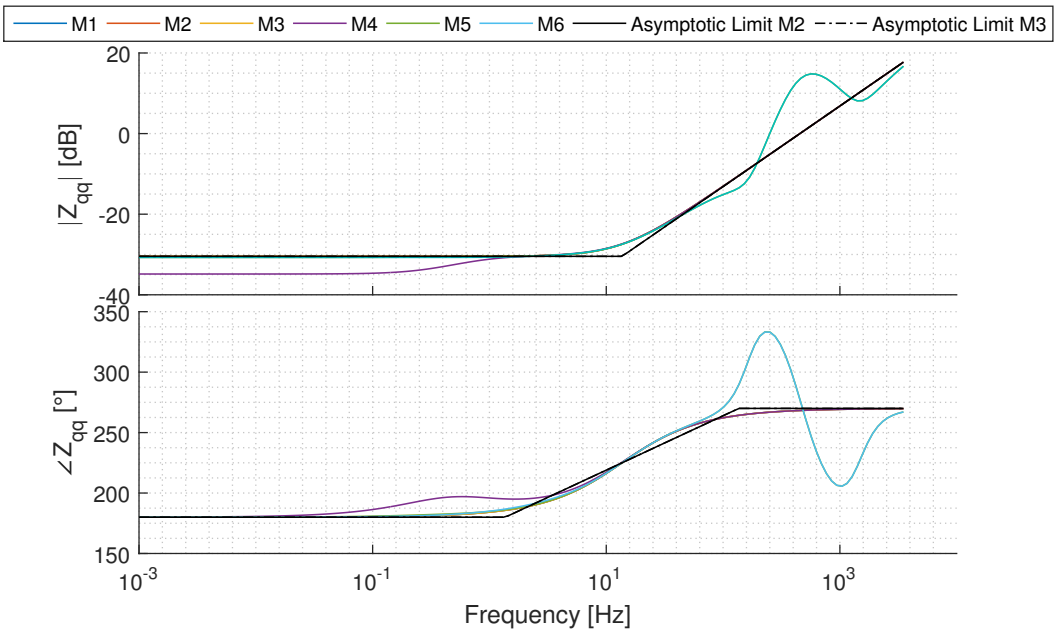

Figure 6.5: QQ-Channel Impedances: Base Case.

6.2.2. M6: Full Model Numerical Assessment

For the sake of simplicity, only the sensitivities of the full-order model are studied. For further details of the sensitivity curves of the other models, check Appendix A.

In order to numerically evaluate the precision of the simplified models, two different indexes are developed. The first index corresponds to the mean deviation of the mid-lines between the full-model curves and the asymptotic curves in a specific range of frequencies, this is,

the difference between the lines drawn in the center of the superior and inferior limits of the sensitivity curves of the full-model and the expected asymptotic curves, averaged over a specific frequency range. Hence, Index 1 (I_1) can be mathematically formulated as presented in (6.2).

$$I_f^1(f) = \left| \frac{Z_{asym}^2(f) + Z_{asym}^1(f)}{2} - \frac{Z_{M6}^2(f) + Z_{M6}^1(f)}{2} \right| \\ \Rightarrow I_1 = \int_{f_1}^{f_2} I_f^1(f) df \tag{6.2}$$

Z_{asym}^i corresponds to the magnitude (in decibels) or the phase of the asymptotic curves (depending on whether the magnitude curves or the phase curves are studied) of M1, M2, or M3, studied in Chapter 5. Analytically, Z_{M6}^i corresponds to the magnitude or phase of the small-signal impedance of the full-order model. $i = 1$ corresponds to the impedance expression assessed in the minimum value of the sensitivity variable, and $i = 2$ to the impedance assessed in the maximum value of the sensitivity variable.

Index 2, as presented in (6.3), corresponds to the difference, at each frequency, between the impedance magnitude or phase sensitivity range of M6 and the impedance magnitude or phase range of the asymptotic curves, averaged over a specific range of frequencies.

$$I_f^2(f) = \left| \left(Z_{asym}^2(f) - Z_{asym}^1(f) \right) - \left(Z_{M6}^2(f) - Z_{M6}^1(f) \right) \right| \\ \Rightarrow I_2 = \int_{f_1}^{f_2} I_f^2(f) df \tag{6.3}$$

Index 1 basically represents the accuracy of the results of Chapter 5, whilst index 2 represents the precision of the obtained expressions of the analytical assessment, regarding the sensitivity ranges of the models. Graphically, this is presented in Figure 6.6, where U corresponds to decibels, when the magnitude graphs are analyzed or to grades, when the phase graphs are analyzed. Note that $I_f^2(f) = |\Delta Z_{asym}(f) - \Delta Z_{M6}(f)|$. By averaging both $I_f^1(f)$ and $I_f^2(f)$ in a specific frequency range, I_1 and I_2 are obtained.

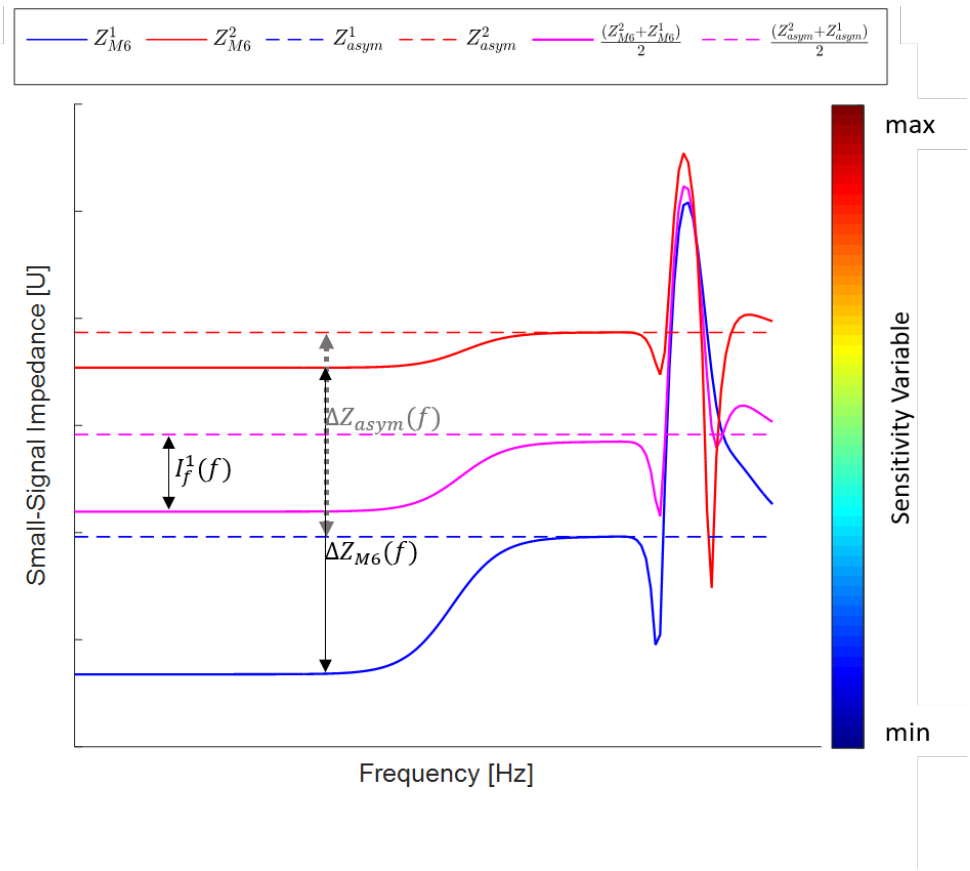

Figure 6.6: Index 1 and Index 2 Explanation.

In order to properly analyze the results through the developed indexes, three frequency ranges are defined: (1) Range 1, corresponding to low frequencies ($< 10^{-1}$ Hz), (2) range 2, corresponding to medium frequencies ($10^{-1} - 10^{2}$ Hz) and (3) range 3, corresponding to high frequencies ($> 10^{2}$ Hz).

The resulting graphs of the numerical assessment are presented in Figures 6.7-6.14.

In the graphs, similarly to Section 6.2.1, the black continuous line corresponds to the asymptotic boundaries determined by M2 and the dashed black line corresponds to the boundaries determined by M3. It would be expected that the small-signal impedance of the actual full-order model was bounded by these limits. Note that, when no variation is presented by the asymptotic limits of M2 and M3, only one overlapped line is present for each case. For the sake of simplicity, it is not explicitly shown which line is the boundary corresponding to the sensitivity variable assessed in the minimum and to the sensitivity variable assessed in the maximum.

Sensitivity Variable: m_p

In Tables 6.3 and 6.4 are presented the index analysis of the numerical assessment of the m_p variable.

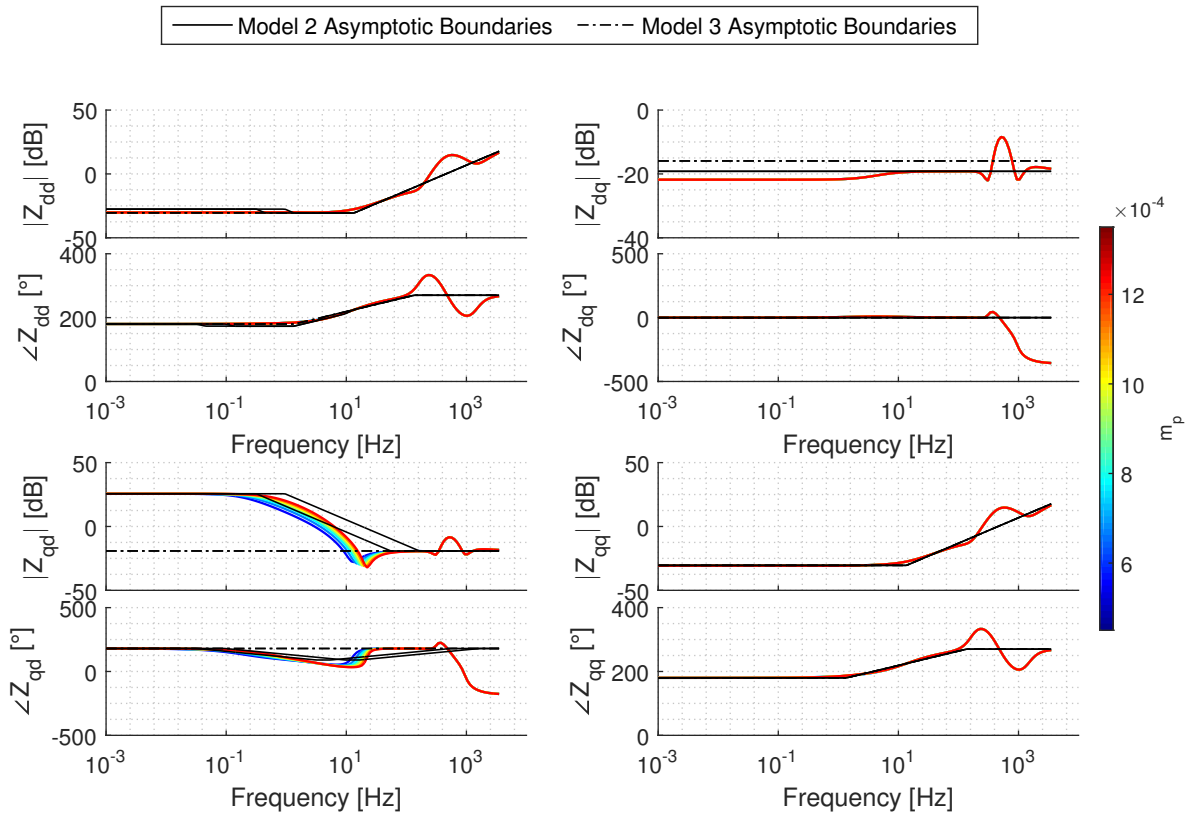

Figure 6.7: M6 Small-Signal Impedance Sensitivity: m_p

- DD**-Channel**
  - **Range 1** As presented, both M1 and M3 have a better performance with respect to index 1 than M2 in this frequency range, showing that the mentioned models are highly accurate. On the other hand, as none of the models is sensitive to m_p, index 2 is the same and almost null in all three models, showing effectively that, in this range, $|Z_{dd}|$ does not vary when m_p changes.
  - **Range 2** In this frequencies, same as in range 1, M1 and M3 have a better performance with respect to index 1 than M2. On the other hand, index 2 shows that the variation presented in M2 is not precise, as in the reality almost zero variation is presented when m_p is changed, demonstrated by the results of M1 and M3.
  - **Range 3** It can be seen that in high frequencies all models have almost the same indexes values, as they all converge to the same curve. Despite that the models follow relatively good the real curve, index 1 presents a relatively high value in the magnitude analysis, due to the resonance produced by the LCL filter, as presented in Section 6.2.1. In the phase analysis, on the other hand, a major deviation is presented, specially in higher frequencies, where the phase considerably decreases. On the other hand, index 2 represents with precision the non-dependence of the inverter with the m_p parameter.
- DQ**-Channel**

– **Ranges 1, 2 and 3** In this cases, M1 and M2 present almost the same index 1 in each case (magnitude and phase), showing a better performance than M3. With respect to index 2, all three models have the same result, showing that this channel is practically non-sensitive to m_p in the whole frequency spectrum.

- QD**-Channel**

  – **Range 1** In the low frequencies, M2 accurately represents the behavior of the full model.

  – **Range 2** Considering the major distortion of the curves by the peak resonance produced by the low-pass filter, M2 is the model that represents considerably better the actual behavior of the small-signal impedance for both accuracy and precision. Note that, in this particular case, a combination of the effects of the low-pass filter

  – **Range 3** As expected from the previous results, M1, M2, and M3 converge to the real magnitude value, while the phase angle decreases considerably in higher frequencies.

- QQ**-Channel**

  – **Range 1, 2 and 3** M1, M2, and M3 behave the same in this channel. With the exception of the resonance in higher frequencies, the models represent precisely the behavior of the full-order model, specially with respect to index 2.

From this analysis it is clear that the m_p parameter mainly affects the small-signal impedance only in the $QD - channel$, specially regarding the values obtained for index 2, as stated by M2, representing with precision the dependency of the inverter with respect to m_p in all four channels.

Table 6.3: Magnitude Graphs Indexes Results: m_p

Channel	Frequency Range	Asymptotic Limits	Index 1 [dB]	Index 2 [dB]	Channel	Frequency Range	Asymptotic Limits	Index 1 [dB]	Index 2 [dB]
$DD - Channel$	**Range 1**	**M1**	0.2758	0.0052	$DQ - Channel$	**Range 1**	**M1**	2.6283	5.5433e-08
		M2	2.6257	0.0052			**M2**	2.6232	5.5433e-08
		M3	0.2758	0.0052			**M3**	5.8669	5.5433e-08
	Range 2	**M1**	0.6780	0.0893		**Range 2**	**M1**	1.4028	5.4958e-06
		M2	1.3030	0.5209			**M2**	1.3977	5.4958e-06
		M3	0.6780	0.0893			**M3**	4.6414	5.4958e-06
	Range 3	**M1**	5.3199	3.3740e-05		**Range 3**	**M1**	2.5044	2.1082e-05
		M2	5.3199	3.3740e-05			**M2**	2.5057	2.1082e-05
		M3	5.3199	3.3740e-05			**M3**	3.6402	2.1082e-05
$QD - Channel$	**Range 1**	**M1**	44.7146	0.1269	$QQ - Channel$	**Range 1**	**M1**	0.2846	0.0058
		M2	0.0774	0.1269			**M2**	0.2846	0.0058
		M3	44.7146	0.1269			**M3**	0.2846	0.0058
	Range 2	**M1**	21.3607	6.8131		**Range 2**	**M1**	0.6711	0.0932
		M2	7.6200	4.4811			**M2**	0.6711	0.0932
		M3	21.3607	6.8131			**M3**	0.6711	0.0932
	Range 3	**M1**	2.5463	0.0386		**Range 3**	**M1**	5.3199	1.0067e-04
		M2	2.6631	0.2713			**M2**	5.3199	1.0067e-04
		M3	2.5463	0.0386			**M3**	5.3199	1.0067e-04

Table 6.4: Phase Graphs Indexes Results: m_p

Channel	Frequency Range	Asymptotic Limits	Index 1 [^{o}]	Index 2 [^{o}]	Channel	Frequency Range	Asymptotic Limits	Index 1 [^{o}]	Index 2 [^{o}]
$DD-Channel$	**Range 1**	**M1**	0.0440	0.1358	$DQ-Channel$	**Range 1**	**M1**	0.0927	2.7684e-06
		M2	0.8214	1.4242			**M2**	0.0927	2.7684e-06
		M3	0.0440	0.1358			**M3**	0.0927	2.7684e-06
	Range 2	**M1**	3.1832	0.4217		**Range 2**	**M1**	3.7980	3.4764e-05
		M2	5.3774	1.5269			**M2**	3.7980	3.4764e-05
		M3	3.1832	0.4217			**M3**	3.7980	3.4764e-05
	Range 3	**M1**	34.9287	1.9298e-04		**Range 3**	**M1**	146.8813	1.5201e-04
		M2	34.9059	0.0244			**M2**	146.8813	1.5201e-04
		M3	34.9287	1.9298e-04			**M3**	146.8813	1.5201e-04
$QD-Channel$	**Range 1**	**M1**	4.6304	4.5261	$QQ-Channel$	**Range 1**	**M1**	0.1550	0.1470
		M2	3.0176	2.0163			**M2**	0.1550	0.1470
		M3	4.6304	4.5261			**M3**	0.1550	0.1470
	Range 2	**M1**	64.2857	23.7421		**Range 2**	**M1**	3.2531	0.4398
		M2	30.8558	19.2326			**M2**	3.2531	0.4398
		M3	64.2857	23.7421			**M3**	3.2531	0.4398
	Range 3	**M1**	146.9302	0.0350		**Range 3**	**M1**	34.9292	8.0873e-04
		M2	156.3923	13.3089			**M2**	34.9292	8.0873e-04
		M3	146.9302	0.0350			**M3**	34.9292	8.0873e-04

Sensitivity Variable: n_q

Tables 6.5 and 6.6 present the index analysis of the numerical assessment of the n_q variable.

- DD-**Channel**
  - **Range 1** Similarly to m_p, for n_q both M1 and M3 have a better performance with respect to index 1 than M2, but presents a slightly higher index 2 value than the previous case.
  - **Range 2** In this frequencies, same as in range 1, M1 and M3 have a better performance with respect to both indexes than M2. Nevertheless, the performance of M2 is still acceptable, as $I^1 = 1{,}4027$ dB in the case of the magnitude analysis and $I^1 = 5{,}5264\ ^o$ in the case of the phase.
  - **Range 3** As expected, all models have almost the same indexes values, as in the previous case. The resonance produced by the LCL filter produces higher deviations, increasing index 1. Nevertheless, the value of index 2 is small, demonstrating a non-dependency of the DD-channel of the inverter with the n_q parameter. In general, this non-dependence is well demonstrated in all frequencies.
- DQ-**Channel**
  - **Ranges 1, 2 and 3** In this case, similar to the analysis of m_p, M1 and M2 present almost the same index 1 and index 2, having a better performance than M3. Note that, despite M3 appears to perform better according to Figure 6.8, it has a higher index 2. This is explained as follows: In the case of the full-order model, the impedance magnitude decreases as n_q increases, but in the case of the asymptotic boundaries, it increases as n_q increases. For the sake of simplicity, this behavior is not explicitly detailed in the graphs, as expressed previously in this Section.
- QD-**Channel**

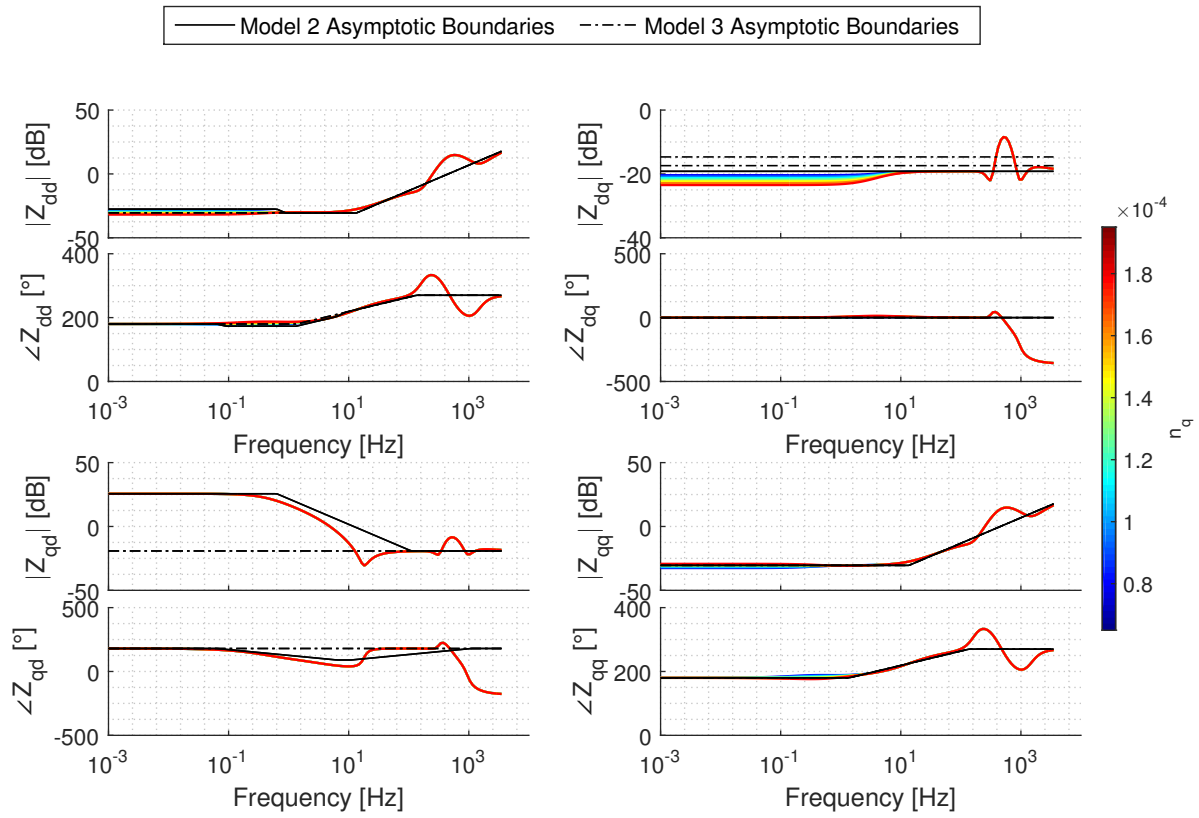

Figure 6.8: M6 Small-Signal Impedance Sensitivity: n_q

– **Range 1, 2 and 3** In this channel, the resulting indexes 1 are similar to the presented for m_p, hence the analysis is analog. In the case of index 2, a better result is obtained, showing that the small-signal impedance of both the asymptotic models and the full-order model is not sensitive to changes in the value of n_q

- QQ**-Channel**

– **Range 1, 2 and 3** As M1, M2, and M3 behave the same in this channel and the resulting indexes are also similar to the presented for the QQ-channel in the analysis of m_p, the results are also analogized.

Obviating the major deviations due to the resonances, it can be noticed that, specially by M2, the behavior of the full-order inverter with respect to changes in n_q is in general accurately and precisely represented. The main sensitivity is presented in the DQ-channel. Despite not being quite precisely represented, it can be noted from the values of index 2 that there does not exist a major dependency with respect to n_q.

Table 6.5: Magnitude Graphs Indexes Results: n_q

Channel	Frequency Range	Asymptotic Limits	Index 1 [dB]	Index 2 [dB]	Channel	Frequency Range	Asymptotic Limits	Index 1 [dB]	Index 2 [dB]
$DD-Channel$	**Range 1**	**M1**	0.1464	3.0598	$DQ-Channel$	**Range 1**	**M1**	2.7636	3.0895
		M2	2.7551	3.0598			**M2**	2.7585	3.0895
		M3	0.1464	3.0598			**M3**	5.8972	5.8228
	Range 2	**M1**	0.6819	0.5324		**Range 2**	**M1**	1.4521	1.5723
		M2	1.4027	0.5324			**M2**	1.4470	1.5723
		M3	0.6819	0.5324			**M3**	4.5857	4.3055
	Range 3	**M1**	5.3199	1.1884e-04		**Range 3**	**M1**	2.5044	0.0119
		M2	5.3199	1.1884e-04			**M2**	2.5057	0.0119
		M3	5.3199	1.1884e-04			**M3**	3.5832	2.7221
$QD-Channel$	**Range 1**	**M1**	44.7578	0.0019	$QQ-Channel$	**Range 1**	**M1**	0.4396	3.2705
		M2	0.0342	0.0019			**M2**	0.4396	3.2705
		M3	44.7578	0.0019			**M3**	0.4396	3.2705
	Range 2	**M1**	22.4707	3.3293e-04		**Range 2**	**M1**	0.6818	0.5623
		M2	7.8872	3.3293e-04			**M2**	0.6818	0.5623
		M3	22.4707	3.3293e-04			**M3**	0.6818	0.5623
	Range 3	**M1**	2.5463	3.7026e-05		**Range 3**	**M1**	5.3199	3.4011e-05
		M2	2.5467	3.7026e-05			**M2**	5.3199	3.4011e-05
		M3	2.5463	3.7026e-05			**M3**	5.3199	3.4011e-05

Table 6.6: Phase Graphs Indexes Results: n_q

Channel	Frequency Range	Asymptotic Limits	Index 1 [^{o}]	Index 2 [^{o}]	Channel	Frequency Range	Asymptotic Limits	Index 1 [^{o}]	Index 2 [^{o}]
$DD-Channel$	**Range 1**	**M1**	0.1934	1.3877	$DQ-Channel$	**Range 1**	**M1**	0.1039	0.1290
		M2	0.7349	1.3877			**M2**	0.1039	0.1290
		M3	0.1934	1.3877			**M3**	0.1039	0.1290
	Range 2	**M1**	3.2861	3.7576		**Range 2**	**M1**	3.9941	4.4767
		M2	5.5264	3.7576			**M2**	3.9941	4.4767
		M3	3.2861	3.7576			**M3**	3.9941	4.4767
	Range 3	**M1**	34.9287	6.7679e-04		**Range 3**	**M1**	146.8813	0.1878
		M2	34.9064	6.7679e-04			**M2**	146.8813	0.1878
		M3	34.9287	6.7679e-04			**M3**	146.8813	0.1878
$QD-Channel$	**Range 1**	**M1**	3.5343	8.2240e-04	$QQ-Channel$	**Range 1**	**M1**	0.2587	1.5028
		M2	2.9122	8.2240e-04			**M2**	0.2587	1.5028
		M3	3.5243	8.2240e-04			**M3**	0.2587	1.5028
	Range 2	**M1**	65.0506	0.0023		**Range 2**	**M1**	3.4213	3.9947
		M2	34.6510	0.0023			**M2**	3.4213	3.9947
		M3	65.0506	0.0023			**M3**	3.4213	3.9947
	Range 3	**M1**	146.9302	2.4878e-04		**Range 3**	**M1**	34.9292	2.0285e-04
		M2	157.8378	2.4878e-04			**M2**	34.9292	2.0285e-04
		M3	146.9302	2.4878e-04			**M3**	34.9292	2.0285e-04

Sensitivity Variable: I_{od}

In Tables 6.7-6.10 are presented the index analysis of the numerical assessment of the I_{od} variable. Note that in this case the graphs and their respective index analysis have been divided into two groups, when $I_{od} < 0$ and $I_{od} > 0$, in order to avoid mounted plots.

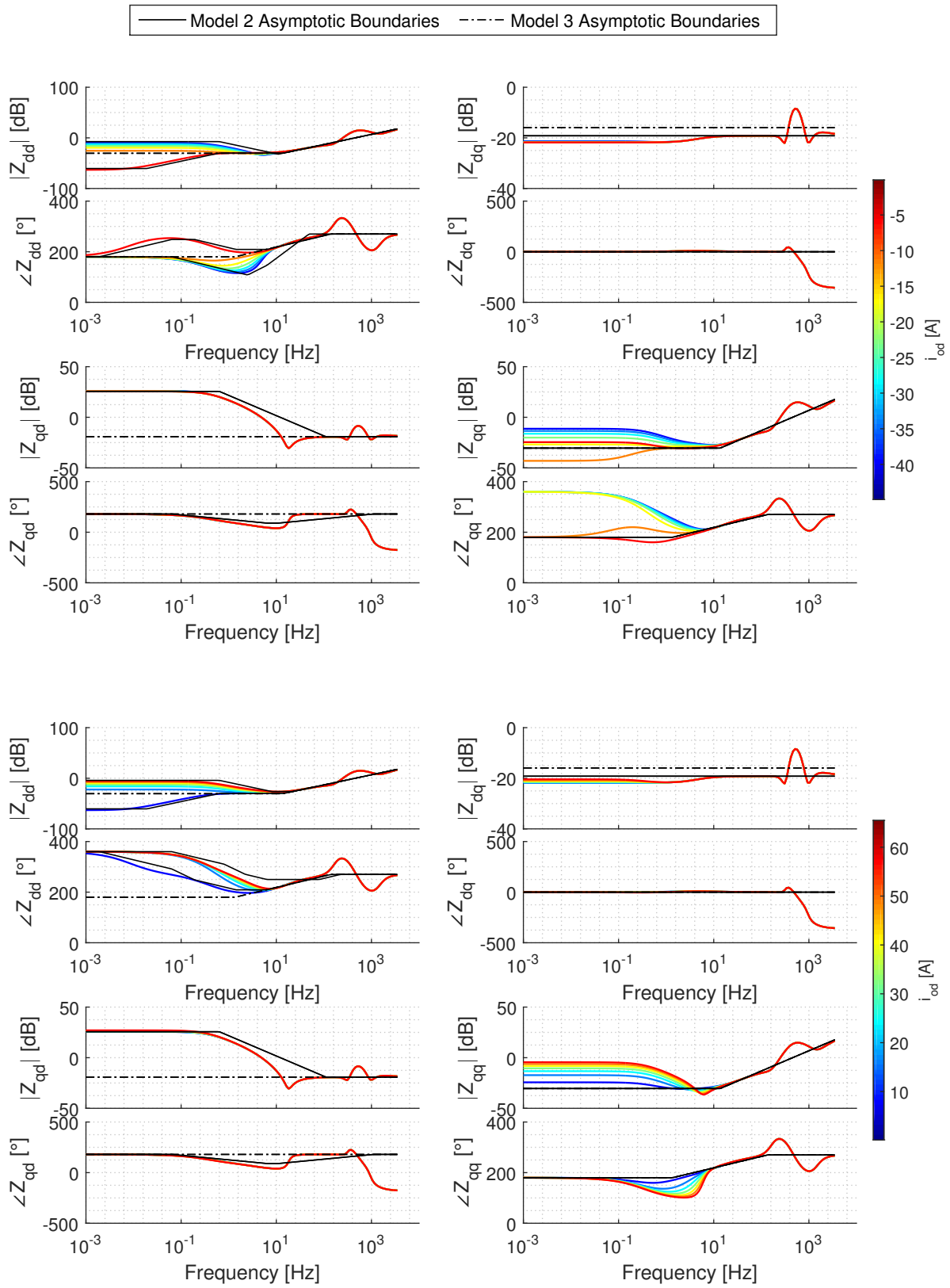

Figure 6.9: M6 Small-Signal Impedance Sensitivity: $I_{od} < 0$ and $I_{od} > 0$

- DD-**Channel**
  - **Range 1 and 2** In this case, only M2 is able to recreate the small-signal impedance behavior with respect to changes in I_{od}.
  - **Range 3** Same as previously, M1, M2, and M3 behave the same for high frequencies, where a major deviation is described by index 1, due to the LCL-filter resonance.
- DQ-**Channel**
  - **Ranges 1 and 2** Similar to previous analysis, M1 and M2 present almost the same index 1 and index 2, having a better performance than M3 and describing well-enough the non-dependency of the impedance to perturbations in I_{od}.
  - **Range 3** All the three models behave the same for high frequencies, experiencing a deviation due to the LCL-filter.
- QD-**Channel**
  - **Range 1, 2 and 3** As index 1 behaves similar to previously analyzed parameters, the same analysis can be made. Nevertheless, in regard to index 2, it can be stated that M2 precisely predicts the sensitivity of the small-signal impedance with respect to changes in the analyzed variable, specially for lower frequencies.
- QQ-**Channel**
  - **Range 1, 2 and 3** As none of the developed models is sensitive to changes in the analyzed variable, major indexes values are obtained for the lower frequencies, as there are major deviations between the simplified and the full-order models. In higher frequencies, however, the curves tend to converge, reducing the indexes values.

Obviating the resonances, it can be noticed that M2 accurately and precisely represent the behavior of the full-order inverter with respect to changes in I_{od}, excepting for the QQ-channel.

Table 6.7: Magnitude Graphs Indexes Results: $I_{od} < 0$

Channel	Frequency Range	Asymptotic Limits	Index 1 [dB]	Index 2 [dB]	Channel	Frequency Range	Asymptotic Limits	Index 1 [dB]	Index 2 [dB]
$DD-Channel$	**Range 1**	**M1**	3.8541	46.7461	$DQ-Channel$	**Range 1**	**M1**	2.3844	0.4817
		M2	1.4678	3.6730			**M2**	2.3793	0.4817
		M3	3.8541	46.7461			**M3**	5.6230	0.4817
	Range 2	**M1**	3.2945	8.3667		**Range 2**	**M1**	1.3600	0.0902
		M2	2.1180	4.7611			**M2**	1.3549	0.0902
		M3	3.2945	8.3667			**M3**	4.5986	0.0902
	Range 3	**M1**	5.3199	1.1443e-04		**Range 3**	**M1**	2.5036	0.0032
		M2	5.3199	1.1443e-04			**M2**	2.5048	0.0032
		M3	5.3199	1.1443e-04			**M3**	3.6395	0.0032
$QD-Channel$	**Range 1**	**M1**	44.9931	0.4608	$QQ-Channel$	**Range 1**	**M1**	12.5041	13.2240
		M2	0.1659	0.5371			**M2**	12.5041	13.2240
		M3	44.9931	0.4608			**M3**	12.5041	13.2240
	Range 2	**M1**	22.4837	0.1350		**Range 2**	**M1**	4.6650	5.9156
		M2	7.9162	0.1447			**M2**	4.6650	5.9156
		M3	22.4837	0.1350			**M3**	4.6650	5.9156
	Range 3	**M1**	2.5447	0.0040		**Range 3**	**M1**	5.3200	1.1610e-04
		M2	2.5452	0.0040			**M2**	5.3200	1.1610e-04
		M3	2.5447	0.0040			**M3**	5.3200	1.1610e-04

Table 6.8: Magnitude Graphs Indexes Results: $I_{od} > 0$

Channel	Frequency Range	Asymptotic Limits	Index 1 [dB]	Index 2 [dB]	Channel	Frequency Range	Asymptotic Limits	Index 1 [dB]	Index 2 [dB]
$DD - Channel$	**Range 1**	**M1**	3.0745	50.8371	$DQ - Channel$	**Range 1**	**M1**	1.9394	1.3711
		M2	1.4485	3.3144			**M2**	1.9343	1.3711
		M3	3.0745	50.8371			**M3**	5.1780	1.3711
	Range 2	**M1**	4.9562	10.8189		**Range 2**	**M1**	1.2980	0.2428
		M2	1.5004	3.6640			**M2**	1.2930	0.2428
		M3	4.9562	10.8189			**M3**	4.5366	0.2428
	Range 3	**M1**	5.3198	1.9719e-04		**Range 3**	**M1**	2.5060	0.0047
		M2	5.3198	1.9719e-04			**M2**	2.5075	0.0047
		M3	5.3198	1.9719e-04			**M3**	3.6418	0.0047
$QD - Channel$	**Range 1**	**M1**	45.4609	1.3955	$QQ - Channel$	**Range 1**	**M1**	16.0108	19.8333
		M2	0.6253	1.3191			**M2**	16.0108	19.8333
		M3	45.4609	1.3955			**M3**	16.0108	19.8333
	Range 2	**M1**	22.6342	0.3358		**Range 2**	**M1**	5.6634	8.4128
		M2	7.7860	0.2999			**M2**	5.6634	8.4128
		M3	22.6342	0.3358			**M3**	5.6634	8.4128
	Range 3	**M1**	2.5494	0.0058		**Range 3**	**M1**	5.3199	1.6996e-04
		M2	2.5499	0.0058			**M2**	5.3199	1.6996e-04
		M3	2.5494	0.0058			**M3**	5.3199	1.6996e-04

Table 6.9: Phase Graphs Indexes Results: $I_{od} < 0$

Channel	Frequency Range	Asymptotic Limits	Index 1 [^{o}]	Index 2 [^{o}]	Channel	Frequency Range	Asymptotic Limits	Index 1 [^{o}]	Index 2 [^{o}]
$DD - Channel$	**Range 1**	**M1**	20.9730	48.6093	$DQ - Channel$	**Range 1**	**M1**	0.0041	0.1896
		M2	5.0473	14.7369			**M2**	0.0041	0.1896
		M3	20.9730	48.6093			**M3**	0.0041	0.1896
	Range 2	**M1**	13.2322	46.6254		**Range 2**	**M1**	3.4952	0.5989
		M2	8.0152	15.4580			**M2**	3.4952	0.5989
		M3	13.2322	46.6254			**M3**	3.4952	0.5989
	Range 3	**M1**	34.9297	0.0025		**Range 3**	**M1**	146.8790	0.0320
		M2	34.8844	0.2284			**M2**	146.8790	0.0320
		M3	34.9297	0.0025			**M3**	146.8790	0.0320
$QD - Channel$	**Range 1**	**M1**	3.6481	0.2316	$QQ - Channel$	**Range 1**	**M1**	87.1003	177.5934
		M2	3.0259	0.2316			**M2**	87.1003	177.5934
		M3	3.6481	0.2316			**M3**	87.1003	177.5934
	Range 2	**M1**	65.3282	0.8349		**Range 2**	**M1**	23.8288	59.4845
		M2	34.9818	0.8286			**M2**	23.8288	59.4845
		M3	65.3282	0.8349			**M3**	23.8288	59.4845
	Range 3	**M1**	146.9242	0.0196		**Range 3**	**M1**	34.9285	0.0019
		M2	157.8265	0.0868			**M2**	34.9285	0.0019
		M3	146.9242	0.0196			**M3**	34.9285	0.0019

Table 6.10: Phase Graphs Indexes Results: $I_{od} > 0$

Channel	Frequency Range	Asymptotic Limits	Index 1 [°]	Index 2 [°]	Channel	Frequency Range	Asymptotic Limits	Index 1 [°]	Index 2 [°]
$DD-Channel$	**Range 1**	**M1**	152.1434	47.2809	$DQ-Channel$	**Range 1**	**M1**	0.2033	0.5878
		M2	10.3634	13.5388			**M2**	0.2033	0.5878
		M3	152.1434	47.2809			**M3**	0.2033	0.5878
	Range 2	**M1**	37.7861	35.7045		**Range 2**	**M1**	3.4289	1.6837
		M2	13.6244	16.6237			**M2**	3.4289	1.6837
		M3	37.7861	35.7045			**M3**	3.4289	1.6837
	Range 3	**M1**	34.9265	0.0040		**Range 3**	**M1**	146.8862	0.0469
		M2	35.6283	1.2532			**M2**	146.8862	0.0469
		M3	34.9265	0.0040			**M3**	146.8862	0.0469
$QD-Channel$	**Range 1**	**M1**	3.7965	0.5286	$QQ-Channel$	**Range 1**	**M1**	2.7610	2.0482
		M2	3.1744	0.5286			**M2**	2.7610	2.0482
		M3	3.7965	0.5286			**M3**	2.7610	2.0482
	Range 2	**M1**	65.9385	1.7565		**Range 2**	**M1**	23.8227	29.2592
		M2	35.4369	1.7483			**M2**	23.8227	29.2592
		M3	65.9385	1.7565			**M3**	23.8227	29.2592
	Range 3	**M1**	146.9428	0.0293		**Range 3**	**M1**	34.9308	0.0028
		M2	157.8608	0.1261			**M2**	34.9308	0.0028
		M3	146.9428	0.0293			**M3**	34.9308	0.0028

Sensitivity Variable: I_{oq}

In Tables 6.11-6.14 are presented the index analysis of the numerical assessment of the I_{oq} variable. Same as in the case of I_{od}, the graphs and their respective index analysis have been divided into two groups, when $I_{oq} < 0$ and $I_{oq} > 0$, in order to avoid mounted plots.

- DD-**Channel**
  - **Range 1** In this case, only M2 recreates the small-signal impedance behavior relatively good with respect to changes in I_{oq}.
  - **Range 2** Despite performing slightly better with respect to index 1, M1 and M3 show a lower performance with respect to index 2. Hence, M2 describes in a better way the response to changes in I_{oq} in a general view.
  - **Range 3** In this case, M1, M2, and M3 behave mainly the same for high frequencies as excepted because of the major deviation, described by index 1, due to the LCL-filter resonance.
- DQ-**Channel**
  - **Ranges 1 and 2** Once again, M1 and M2 present almost the same index 1 and index 2 values, having a better performance than M3 and describing well-enough the non-dependency of the impedance to perturbations in I_{oq}.
  - **Range 3** All the three models behave the same for high frequencies, deviating due to the LCL-filter. The non-dependency in this range of the impedance to changes in the analyzed parameter is accurately predicted.
- QD-**Channel**
  - **Range 1, 2 and 3** Considering the similar behavior of the indexes, the same analysis as for the sensitivity in respect with I_{od} can be made.

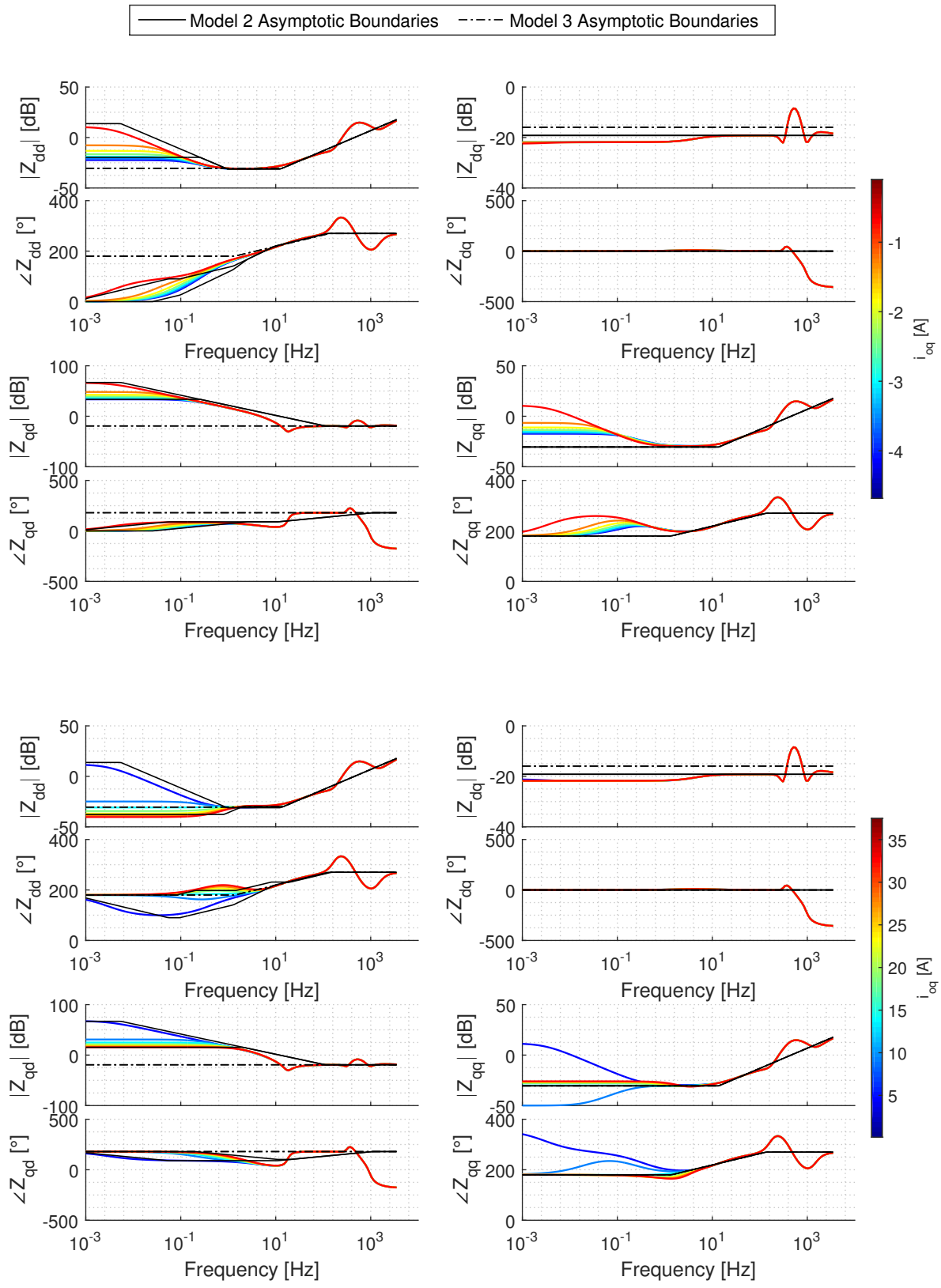

Figure 6.10: M6 Small-Signal Impedance Sensitivity:$I_{oq} < 0$ and $I_{oq} > 0$

- QQ-**Channel**
  - **Range 1, 2 and 3** Similarly to the case of I_{od}, major indexes values are obtained in the lower frequencies, as there are major deviations between the simplified and the full-order models. In the higher frequencies, the models tends to converge, as expected from previous results.

Similar to the case of I_{od}, it can be noticed that, obviating the resonances, M2 represents in a better way the behavior of the full-order inverter with respect to changes in I_{oq}, excepting for the QQ-channel.

Table 6.11: Magnitude Graphs Indexes Results: $I_{oq} < 0$

Channel	Frequency Range	Asymptotic Limits	Index 1 [dB]	Index 2 [dB]	Channel	Frequency Range	Asymptotic Limits	Index 1 [dB]	Index 2 [dB]
$DD-Channel$	**Range 1**	**M1**	18.5712	21.3087	$DQ-Channel$	**Range 1**	**M1**	2.7501	0.1524
		M2	4.8074	3.8513			**M2**	2.7450	0.1524
		M3	18.5712	21.3087			**M3**	5.9789	0.1528
	Range 2	**M1**	1.6729	0.5699		**Range 2**	**M1**	1.4171	0.0063
		M2	2.1204	0.3417			**M2**	1.4120	0.0063
		M3	1.6729	0.5699			**M3**	4.6459	0.0055
	Range 3	**M1**	5.3198	4.0592e-05		**Range 3**	**M1**	2.5043	3.2513e-05
		M2	5.3198	4.0592e-05			**M2**	2.5056	3.2513e-05
		M3	5.3198	4.0592e-05			**M3**	3.6348	0.0032
$QD-Channel$	**Range 1**	**M1**	63.0870	21.2970	$QQ-Channel$	**Range 1**	**M1**	21.1629	16.4534
		M2	2.1822	3.8630			**M2**	21.1629	16.4534
		M3	63.0870	21.2970			**M3**	21.1629	16.4534
	Range 2	**M1**	23.4032	0.5289		**Range 2**	**M1**	2.6524	0.6579
		M2	8.6846	0.3457			**M2**	2.6524	0.6579
		M3	23.4032	0.5289			**M3**	2.6524	0.6579
	Range 3	**M1**	2.5467	1.8174e-04		**Range 3**	**M1**	5.3199	4.0226e-05
		M2	2.5472	1.8174e-04			**M2**	5.3199	4.0226e-05
		M3	2.5467	1.8174e-04			**M3**	5.3199	4.0226e-05

Table 6.12: Magnitude Graphs Indexes Results: $I_{oq} > 0$

Channel	Frequency Range	Asymptotic Limits	Index 1 [dB]	Index 2 [dB]	Channel	Frequency Range	Asymptotic Limits	Index 1 [dB]	Index 2 [dB]
$DD-Channel$	**Range 1**	**M1**	9.8826	39.3571	$DQ-Channel$	**Range 1**	**M1**	2.5297	0.1528
		M2	4.4636	3.8713			**M2**	2.5246	0.1528
		M3	9.8826	39.3571			**M3**	5.7734	0.1513
	Range 2	**M1**	1.1172	3.8913		**Range 2**	**M1**	1.3952	0.0370
		M2	1.5633	1.8194			**M2**	1.3901	0.0370
		M3	1.1172	3.8913			**M3**	4.6389	0.0315
	Range 3	**M1**	5.3199	3.3102e-04		**Range 3**	**M1**	2.5044	2.8024e-04
		M2	5.3199	3.3102e-04			**M2**	2.5057	2.8024e-04
		M3	5.3199	3.3102e-04			**M3**	3.6430	0.0265
$QD-Channel$	**Range 1**	**M1**	54.3446	39.4520	$QQ-Channel$	**Range 1**	**M1**	16.9648	24.9458
		M2	1.8971	3.7834			**M2**	16.9648	24.9458
		M3	54.3446	39.4520			**M3**	16.9648	24.9458
	Range 2	**M1**	21.8555	3.9778		**Range 2**	**M1**	2.1113	1.0888
		M2	7.7332	1.8183			**M2**	2.1113	1.0888
		M3	21.8555	3.9778			**M3**	2.1113	1.0888
	Range 3	**M1**	2.5460	0.0015		**Range 3**	**M1**	5.3200	3.2124e-04
		M2	2.5465	0.0015			**M2**	5.3200	3.2124e-04
		M3	2.5460	0.0015			**M3**	5.3200	3.2124e-04

Table 6.13: Phase Graphs Indexes Results: $I_{oq} < 0$

Channel	Frequency Range	Asymptotic Limits	Index 1 [^{o}]	Index 2 [^{o}]	Channel	Frequency Range	Asymptotic Limits	Index 1 [^{o}]	Index 2 [^{o}]
$DD - Channel$	**Range 1**	**M1**	141.0234	54.3282	$DQ - Channel$	**Range 1**	**M1**	0.5153	1.0472
		M2	8.6117	6.8697			**M2**	0.5153	1.0472
		M3	141.0234	54.3282			**M3**	0.5153	1.0472
	Range 2	**M1**	24.4924	8.9840		**Range 2**	**M1**	3.8180	0.0128
		M2	13.1778	5.6745			**M2**	3.8180	0.0128
		M3	24.4924	8.9840			**M3**	3.8180	0.0128
	Range 3	**M1**	34.9283	2.8526e-04		**Range 3**	**M1**	146.8811	5.3878e-04
		M2	34.8355	0.0232			**M2**	146.8811	5.3878e-04
		M3	34.9283	2.8526e-04			**M3**	146.8811	5.3878e-04
$QD - Channel$	**Range 1**	**M1**	144.5204	54.2911	$QQ - Channel$	**Range 1**	**M1**	32.8975	52.8755
		M2	5.1496	6.8832			**M2**	32.8975	52.8755
		M3	144.5204	54.2911			**M3**	32.8975	52.8755
	Range 2	**M1**	87.9376	9.0103		**Range 2**	**M1**	17.2769	5.0987
		M2	28.8677	5.5561			**M2**	17.2769	5.0987
		M3	87.9376	9.0103			**M3**	17.2769	5.0987
	Range 3	**M1**	146.9302	1.7123e-04		**Range 3**	**M1**	34.9281	3.9346e-04
		M2	157.8378	1.7123e-04			**M2**	34.9281	3.9346e-04
		M3	146.9302	1.7123e-04			**M3**	34.9281	3.9346e-04

Table 6.14: Phase Graphs Indexes Results: $I_{oq} > 0$

Channel	Frequency Range	Asymptotic Limits	Index 1 [^{o}]	Index 2 [^{o}]	Channel	Frequency Range	Asymptotic Limits	Index 1 [^{o}]	Index 2 [^{o}]
$DD - Channel$	**Range 1**	**M1**	29.5150	64.4544	$DQ - Channel$	**Range 1**	**M1**	0.5315	1.0922
		M2	5.7833	9.7954			**M2**	0.5315	1.0922
		M3	29.5150	64.4544			**M3**	0.5315	1.0922
	Range 2	**M1**	7.4823	31.3253		**Range 2**	**M1**	3.7647	0.1089
		M2	10.2619	8.5512			**M2**	3.7647	0.1089
		M3	7.4823	31.3253			**M3**	3.7647	0.1089
	Range 3	**M1**	34.9289	0.0023		**Range 3**	**M1**	146.8815	0.0045
		M2	34.9588	0.2216			**M2**	146.8815	0.0045
		M3	34.9289	0.0023			**M3**	146.8815	0.0045
$QD - Channel$	**Range 1**	**M1**	33.1816	64.1554	$QQ - Channel$	**Range 1**	**M1**	55.4631	111.7539
		M2	5.0443	9.7235			**M2**	55.4631	111.7539
		M3	33.1816	64.1554			**M3**	55.4631	111.7539
	Range 2	**M1**	67.1929	31.5478		**Range 2**	**M1**	9.6855	23.5682
		M2	32.5741	6.8561			**M2**	9.6855	23.5682
		M3	67.1929	31.5478			**M3**	9.6855	23.5682
	Range 3	**M1**	146.9302	0.0014		**Range 3**	**M1**	34.9297	0.0031
		M2	157.8378	0.0014			**M2**	34.9297	0.0031
		M3	146.9302	0.0014			**M3**	34.9297	0.0031

Sensitivity Variable: V_{bD}

The index analysis of the numerical assessment of V_{bD} is presented in Tables 6.15 and 6.16.

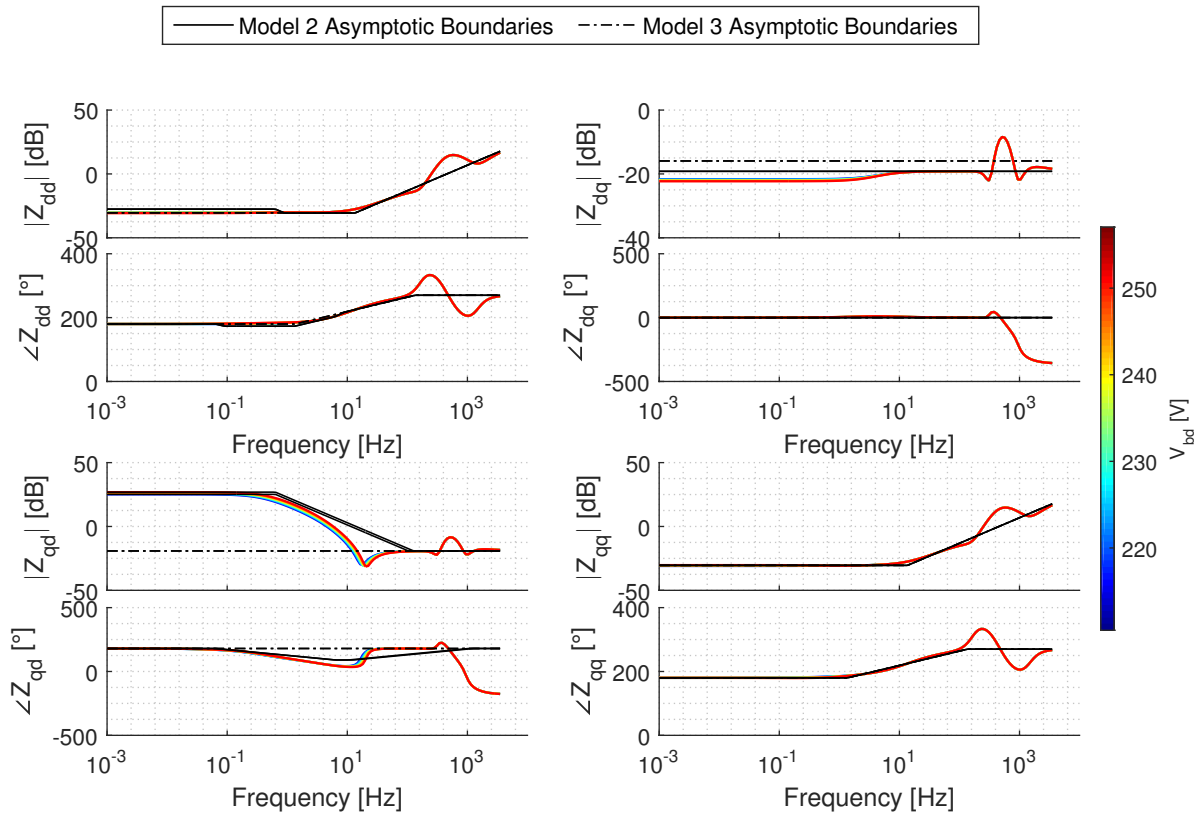

Figure 6.11: M6 Small-Signal Impedance Sensitivity: V_{bD}

- DD**-Channel**
  - **Range 1, 2 and 3** It can be noted that the resulting indexes are similar to the ones of the case of m_p. The main difference between the sensitivities of m_p and the V_{bD} is the results of index 2, where no difference exist between the different asymptotic models in the case of V_{bD}. Despite presenting a higher index 2 (for both magnitude and phase graphs), it still shows a low dependency of the impedance with respect to the analyzed variable.
- DQ**-Channel**
  - **Ranges 1, 2 and 3** Same as the previous channel, the resulting indexes are similar to the ones of the case of m_p, including both index 1 and 2. Hence, similar conclusions can be made.
- QD**-Channel**
  - **Range 1, 2 and 3** In the case of indexes 1, very similar results to m_p are obtained. Index 2, however, presents a notably better performance in this case, with exception of the higher frequencies phase angle, where the same deviation is present.
- QQ**-Channel**
  - **Range 1, 2 and 3** M1, M2, and M3 behave the same in this channel. With the exception of the resonance in higher frequencies, the models represent precisely the behavior of the full-order model, specially with respect to index 2.

Similar as in the case of m_p, this analysis shows that variations in V_{bD} mainly affects only the small-signal impedance in the $QD - channel$. The values of index 2 for M2 represents the sensitivity of the inverter with respect to the V_{bD} parameter in all four channels.

Table 6.15: Magnitude Graphs Indexes Results: V_{bd}

Channel	Frequency Range	Asymptotic Limits	Index 1 [dB]	Index 2 [dB]	Channel	Frequency Range	Asymptotic Limits	Index 1 [dB]	Index 2 [dB]
$DD - Channel$	**Range 1**	**M1**	0.1092	0.6527	$DQ - Channel$	**Range 1**	**M1**	2.7979	0.6585
		M2	2.7923	0.6527			**M2**	2.7928	0.6585
		M3	0.1092	0.6527			**M3**	6.0365	0.6585
	Range 2	**M1**	0.6623	0.1213		**Range 2**	**M1**	1.4883	0.3346
		M2	1.4309	0.1213			**M2**	1.4883	0.3346
		M3	0.6623	0.1213			**M3**	4.7269	0.3346
	Range 3	**M1**	5.3199	1.3989e-05		**Range 3**	**M1**	2.5041	0.0025
		M2	5.3199	1.3989e-05			**M2**	2.5041	0.0025
		M3	5.3199	1.3989e-05			**M3**	3.6399	0.0025
$QD - Channel$	**Range 1**	**M1**	45.1620	1.7493	$QQ - Channel$	**Range 1**	**M1**	0.1231	0.6705
		M2	0.0317	0.0133			**M2**	0.1231	0.6705
		M3	45.1620	1.7493			**M3**	0.1231	0.6705
	Range 2	**M1**	22.9719	2.9395		**Range 2**	**M1**	0.6519	0.1268
		M2	7.7673	2.0714			**M2**	0.6519	0.1268
		M3	22.9719	2.9395			**M3**	0.6519	0.1268
	Range 3	**M1**	2.5507	0.0172		**Range 3**	**M1**	5.3199	2.3955e-05
		M2	2.5700	0.0550			**M2**	5.3199	2.3955e-05
		M3	2.5507	0.0172			**M3**	5.3199	2.3955e-05

Table 6.16: Phase Graphs Indexes Results: V_{bd}

Channel	Frequency Range	Asymptotic Limits	Index 1 [^{o}]	Index 2 [^{o}]	Channel	Frequency Range	Asymptotic Limits	Index 1 [^{o}]	Index 2 [^{o}]
$DD - Channel$	**Range 1**	**M1**	0.1434	0.2933	$DQ - Channel$	**Range 1**	**M1**	0.1000	0.0275
		M2	0.6850	0.2933			**M2**	0.1000	0.0275
		M3	0.1434	0.2933			**M3**	0.1000	0.0275
	Range 2	**M1**	3.3768	0.8468		**Range 2**	**M1**	4.0439	0.9543
		M2	5.6160	0.8468			**M2**	4.0439	0.9543
		M3	3.3768	0.8468			**M3**	4.0439	0.9543
	Range 3	**M1**	34.9287	9.6789e-05		**Range 3**	**M1**	146.8829	0.0393
		M2	34.9064	9.6789e-05			**M2**	146.8829	0.0393
		M3	34.9287	9.6789e-05			**M3**	146.8829	0.0393
$QD - Channel$	**Range 1**	**M1**	3.3930	0.6654	$QQ - Channel$	**Range 1**	**M1**	0.0615	0.2955
		M2	2.7708	0.6654			**M2**	0.0615	0.2955
		M3	3.3930	0.6654			**M3**	0.0615	0.2955
	Range 2	**M1**	65.7566	6.9509		**Range 2**	**M1**	3.0579	0.8741
		M2	33.8798	6.8721			**M2**	3.0579	0.8741
		M3	65.7566	6.9509			**M3**	3.0579	0.8741
	Range 3	**M1**	146.9335	0.0159		**Range 3**	**M1**	34.9293	1.8959e-04
		M2	157.9920	2.6368			**M2**	34.9293	1.8959e-04
		M3	146.9335	0.0159			**M3**	34.9293	1.8959e-04

Sensitivity Variable: $\overline{\omega}$

The index analysis of the numerical assessment of $\overline{\omega}$ is presented in Tables 6.17 and 6.18.

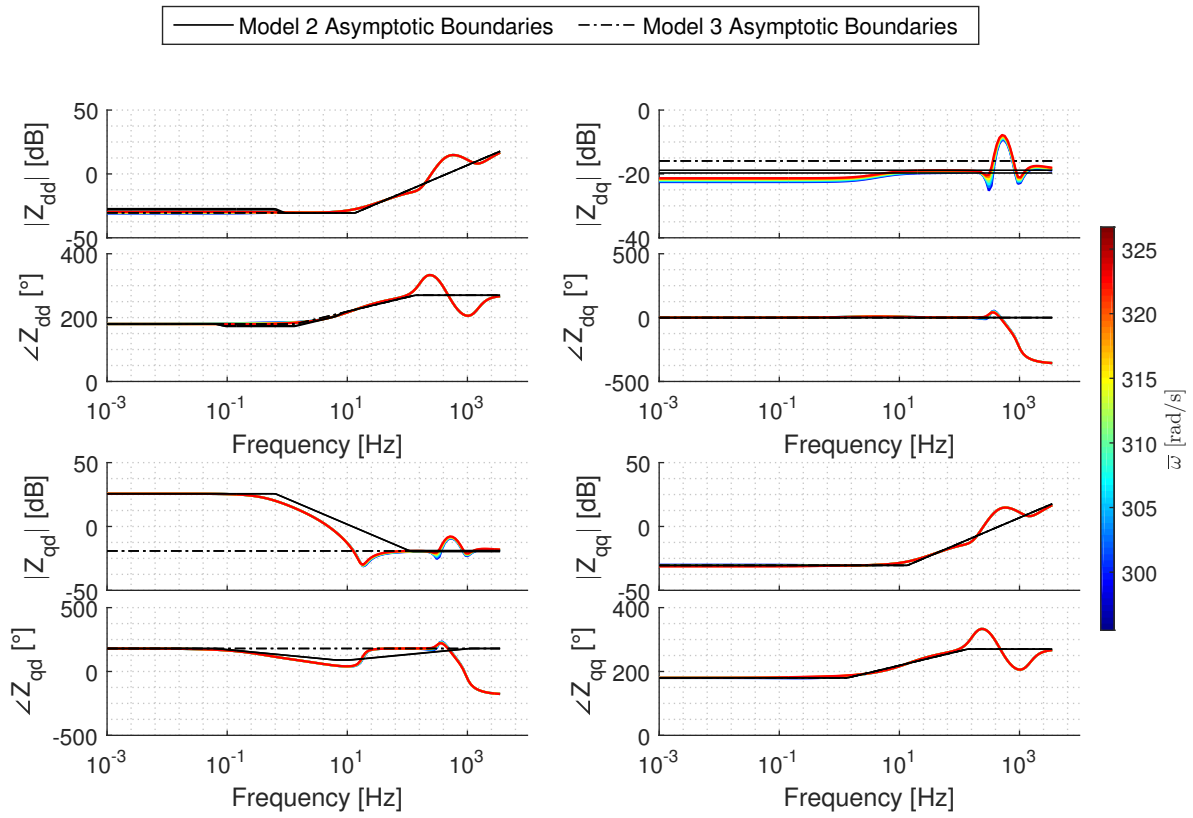

Figure 6.12: M6 Small-Signal Impedance Sensitivity: $\overline{\omega}$

- **DD-Channel, DQ-Channel and QQ-Channel**

  - **Range 1, 2 and 3** Same as in the previous case, it can be noted that the resulting indexes are similar to the ones of the case of m_p in DD-channel, DQ-channel and QQ-channel, specially for index 1. The main difference between the sensitivities of m_p and this case is the results of index 2, where slightly higher results are obtained. Nevertheless, it still shows that the asymptotic models represent precisely the non-dependency of the impedance with respect to this parameter.

- **QD-Channel**

  - **Range 1, 2 and 3** In this channel, the results are similar to the ones of the case of n_q. Hence, the same conclusions can be made.

In this case, it can be observed that M2 represents effectively the shape of the impedance graphs as well as the low dependency of the small-signal impedance with respect to changes in $\overline{\omega}$.

Table 6.17: Magnitude Graphs Indexes Results: $\overline{\omega}$

Channel	Frequency Range	Asymptotic Limits	Index 1 [dB]	Index 2 [dB]	Channel	Frequency Range	Asymptotic Limits	Index 1 [dB]	Index 2 [dB]
$DD-Channel$	**Range 1**	**M1**	0.1506	1.1751	$DQ-Channel$	**Range 1**	**M1**	2.7568	1.1854
		M2	2.6601	0.3034			**M2**	2.6609	0.3138
		M3	0.1506	1.1751			**M3**	5.9954	1.1854
	Range 2	**M1**	0.6675	0.2116		**Range 2**	**M1**	1.5107	1.0146
		M2	1.3882	0.1081			**M2**	1.4167	0.1746
		M3	0.6675	0.2116			**M3**	4.7493	1.0146
	Range 3	**M1**	5.3199	0.0040		**Range 3**	**M1**	2.5046	1.4209
		M2	5.3199	0.0040			**M2**	2.5244	0.7326
		M3	5.3199	0.0040			**M3**	3.7068	1.4209
$QD-Channel$	**Range 1**	**M1**	44.7578	6.7185e-04	$QQ-Channel$	**Range 1**	**M1**	0.1949	1.2228
		M2	0.0343	6.7185e-04			**M2**	0.1949	1.2228
		M3	44.7578	6.7185e-04			**M3**	0.1949	1.2228
	Range 2	**M1**	22.5006	0.3777		**Range 2**	**M1**	0.6601	0.2217
		M2	7.9098	0.3777			**M2**	0.6601	0.2217
		M3	22.5006	0.3777			**M3**	0.6601	0.2217
	Range 3	**M1**	2.5470	1.4253		**Range 3**	**M1**	5.3200	0.0040
		M2	2.5603	0.7337			**M2**	5.3200	0.0040
		M3	2.5470	1.4253			**M3**	5.3200	0.0040

Table 6.18: Phase Graphs Indexes Results: $\overline{\omega}$

Channel	Frequency Range	Asymptotic Limits	Index 1 [^{o}]	Index 2 [^{o}]	Channel	Frequency Range	Asymptotic Limits	Index 1 [^{o}]	Index 2 [^{o}]
$DD-Channel$	**Range 1**	**M1**	0.1366	0.4935	$DQ-Channel$	**Range 1**	**M1**	0.0943	0.0129
		M2	0.6668	0.4054			**M2**	0.0943	0.0129
		M3	0.1366	0.4935			**M3**	0.0943	0.0129
	Range 2	**M1**	3.2939	1.4475		**Range 2**	**M1**	3.8474	0.4660
		M2	5.4319	0.8818			**M2**	3.8474	0.4660
		M3	3.2939	1.4475			**M3**	3.8474	0.4660
	Range 3	**M1**	34.9277	0.0264		**Range 3**	**M1**	146.8133	5.6074
		M2	34.9061	0.0344			**M2**	146.8133	5.6074
		M3	34.9277	0.0264			**M3**	146.8133	5.6074
$QD-Channel$	**Range 1**	**M1**	3.5343	2.4154e-04	$QQ-Channel$	**Range 1**	**M1**	0.0914	0.5081
		M2	2.9122	2.4154e-04			**M2**	0.0914	0.5081
		M3	3.5343	2.4154e-04			**M3**	0.0914	0.5081
	Range 2	**M1**	65.1915	1.3507		**Range 2**	**M1**	3.1708	1.5090
		M2	34.6623	1.3207			**M2**	3.1708	1.5090
		M3	65.1915	1.3507			**M3**	3.1708	1.5090
	Range 3	**M1**	146.9187	5.6769		**Range 3**	**M1**	34.9282	0.0262
		M2	157.5303	5.7073			**M2**	34.9282	0.0262
		M3	146.9187	5.6769			**M3**	34.9282	0.0262

Sensitivity Variable: r_C

Tables 6.19 and 6.20 present the index analysis of the numerical assessment of the r_C variable.

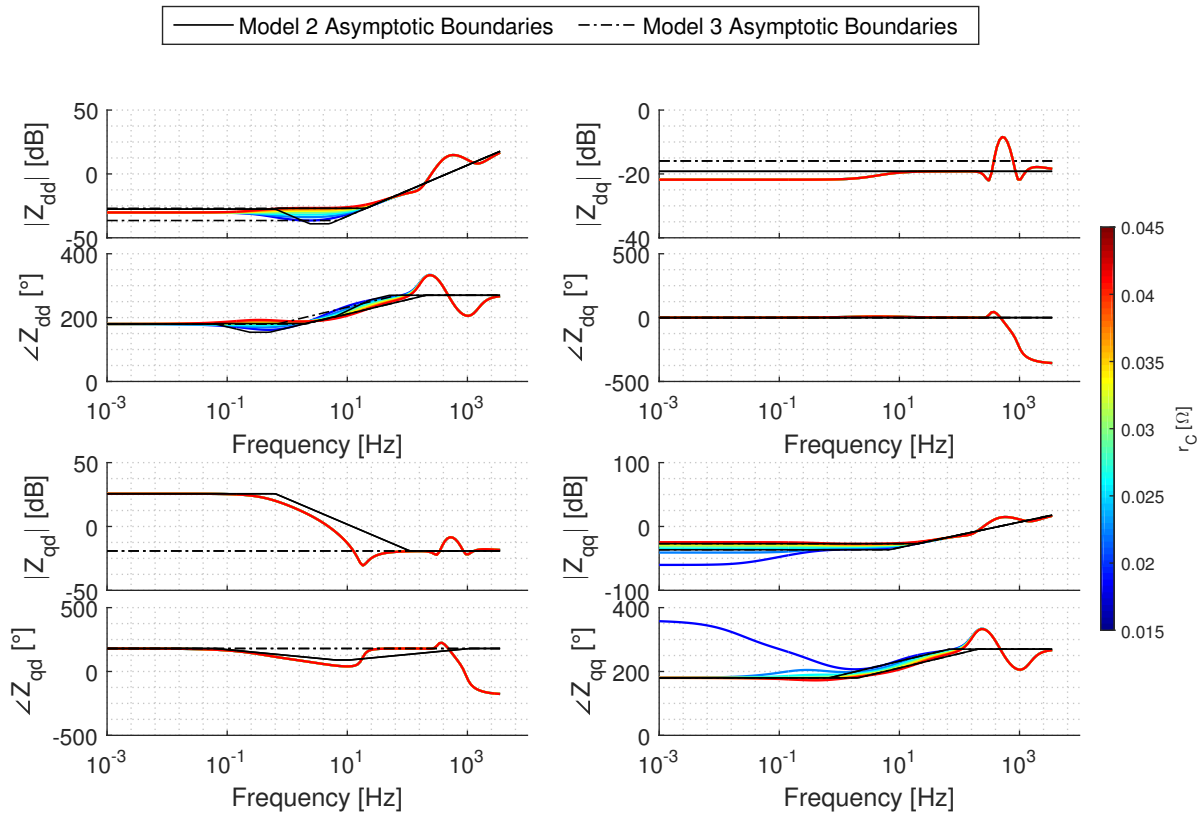

Figure 6.13: M6 Small-Signal Impedance Sensitivity: r_C

- DD-**Channel**
  - **Range 1** In this frequency range, both M1 and M3 have a slightly better performance with respect to index 1 than M2, but presents considerably higher index 2 value than the latter.
  - **Range 2** In this frequencies, M2 has slightly worse performance than the other models with respect to index 1, but a slightly better with respect to index 2.
  - **Range 3** As expected, all models have almost the same indexes values, similar as in previous cases.
- DQ-**Channel**
  - **Ranges 1, 2 and 3** M1 and M2 present almost the same index 1 and index 2, having a better performance than M3 in all the frequency ranges.
- QD-**Channel**
  - **Range 1, 2 and 3** Regarding indexes 1, the results are similar to the presented for m_p, hence the analysis is analog. In the case of index 2 it is shown that the small-signal impedances of both the asymptotic models and the full-order model are not sensitive to changes in the value of r_C.
- QQ-**Channel**
  - **Range 1, 2 and 3** In this case, the asymptotic models describe a poor performance, specially with respect to index 2, as the curves of the full model present high dependency with respect to values of r_C, specially at low values.

From the aforementioned results, it can be noted that M2 describes effectively the behavior of the small-signal impedance (specially regarding the sensitivity represented by index 2), with the exception of the QQ-channel, where the high dependency between the impedance and changes in r_C is not correctly predicted.

Table 6.19: Magnitude Graphs Indexes Results: r_C

Channel	Frequency Range	Asymptotic Limits	Index 1 [dB]	Index 2 [dB]	Channel	Frequency Range	Asymptotic Limits	Index 1 [dB]	Index 2 [dB]
$DD-Channel$	**Range 1**	**M1**	1.5369	9.4692	$DQ-Channel$	**Range 1**	**M1**	2.6270	0.0015
		M2	2.6140	0.0733			**M2**	2.6219	0.0015
		M3	1.5369	9.4692			**M3**	5.8656	0.0015
	Range 2	**M1**	1.0048	2.3192		**Range 2**	**M1**	1.4026	8.2008e-04
		M2	1.6190	2.1588			**M2**	1.3975	8.2008e-04
		M3	1.0048	2.3192			**M3**	4.6412	8.2008e-04
	Range 3	**M1**	5.3177	0.1339		**Range 3**	**M1**	2.5044	7.7678e-06
		M2	5.3177	0.1339			**M2**	2.5057	7.7678e-06
		M3	5.3177	0.1339			**M3**	3.6402	7.7678e-06
$QD-Channel$	**Range 1**	**M1**	44.7578	0.0104	$QQ-Channel$	**Range 1**	**M1**	9.2680	23.2138
		M2	0.0342	0.0052			**M2**	9.2680	23.2138
		M3	44.7578	0.0104			**M3**	9.2680	23.2138
	Range 2	**M1**	22.4707	0.0096		**Range 2**	**M1**	1.0359	2.4625
		M2	7.8872	0.0072			**M2**	1.0359	2.4625
		M3	22.4707	0.0096			**M3**	1.0359	2.4625
	Range 3	**M1**	2.5463	4.6972e-05		**Range 3**	**M1**	5.3177	0.1339
		M2	2.5467	4.6972e-05			**M2**	5.3177	0.1339
		M3	2.5463	4.6972e-05			**M3**	5.3177	0.1339

Table 6.20: Phase Graphs Indexes Results: r_C

Channel	Frequency Range	Asymptotic Limits	Index 1 [^{o}]	Index 2 [^{o}]	Channel	Frequency Range	Asymptotic Limits	Index 1 [^{o}]	Index 2 [^{o}]
$DD-Channel$	**Range 1**	**M1**	0.0533	3.3699	$DQ-Channel$	**Range 1**	**M1**	0.0922	4.9322e-05
		M2	0.2961	2.5658			**M2**	0.0922	4.9322e-05
		M3	0.0533	3.3699			**M3**	0.0922	4.9322e-05
	Range 2	**M1**	3.0050	15.2400		**Range 2**	**M1**	3.7964	0.0022
		M2	4.9773	7.9946			**M2**	3.7964	0.0022
		M3	3.0050	15.2400			**M3**	3.7964	0.0022
	Range 3	**M1**	35.3356	0.5448		**Range 3**	**M1**	146.8813	1.1572e-04
		M2	35.3392	0.5448			**M2**	146.8813	1.1572e-04
		M3	35.3356	0.5448			**M3**	146.8813	1.1572e-04
$QD-Channel$	**Range 1**	**M1**	3.5343	2.1064e-05	$QQ-Channel$	**Range 1**	**M1**	72.4482	146.5629
		M2	2.9122	2.1064e-05			**M2**	72.4482	146.5629
		M3	3.5343	2.1064e-05			**M3**	72.4482	146.5629
	Range 2	**M1**	65.0506	0.0157		**Range 2**	**M1**	10.1809	24.3032
		M2	34.6510	0.0156			**M2**	10.1809	24.3032
		M3	65.0506	0.0157			**M3**	10.1809	24.3032
	Range 3	**M1**	146.9302	4.4966e-05		**Range 3**	**M1**	35.3361	0.5448
		M2	157.8378	0.0077			**M2**	35.3361	0.5448
		M3	146.9302	4.4966e-05			**M3**	35.3361	0.5448

Sensitivity Variable: L_C

Finally, in Tables 6.21 and 6.22 are presented the index analysis of the numerical assessment of the L_C variable.

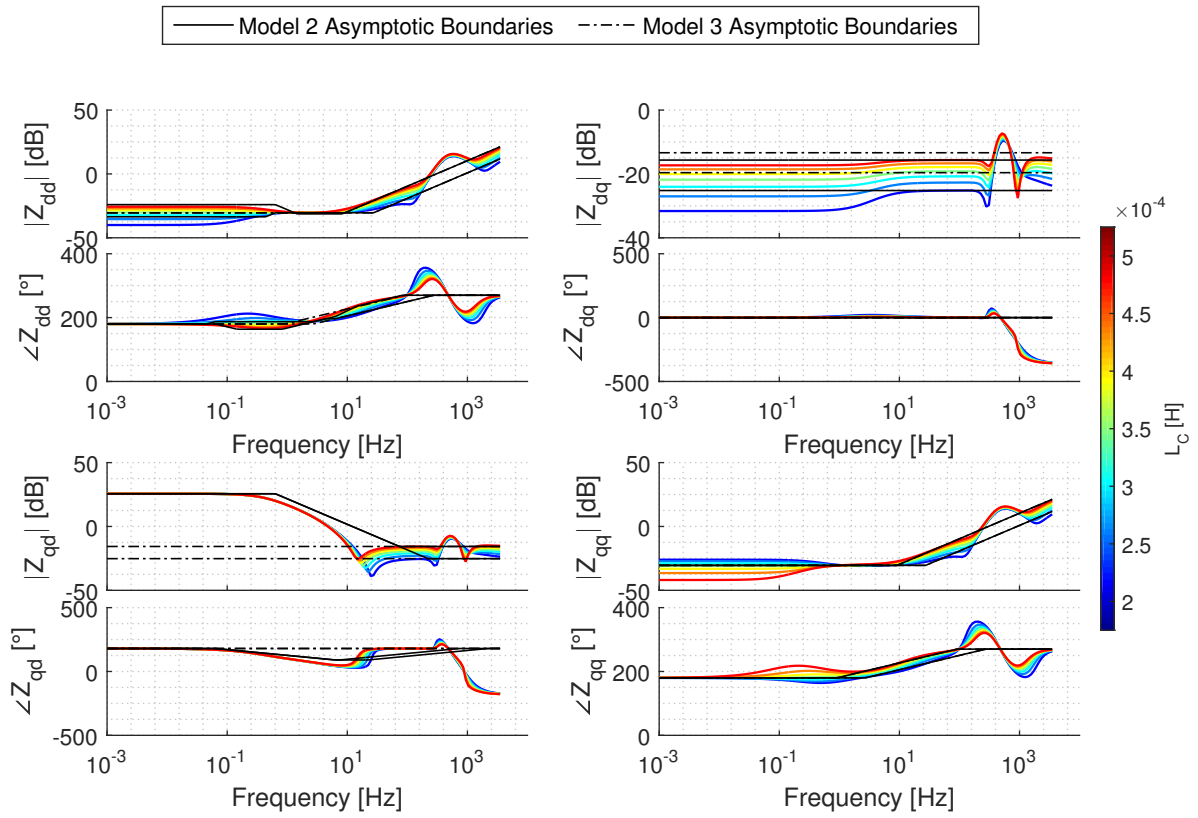

Figure 6.14: Model 6 Small-Signal Impedance Sensitivity: L_C

- DD**-Channel**
  - **Range 1 and 2** In this frequency ranges the behavior of the indexes are similar to the presented for r_C, hence the analysis can be analogized.
  - **Range 3** As expected, all models have almost the same indexes values, similar as in previous cases. However, unlike the results presented for r_C, here a relatively high index 2 is presented, mainly produced by the resonance introduced by the LCL-filter.
- DQ**-Channel**
  - **Ranges 1, 2 and 3** M1 and M2 present almost the same indexes 1 and 2. Despite having a considerably better performance than model 3, the indexes of these models are still slightly higher than previous cases, specifically with respect to index 2.
- QD**-Channel**
  - **Range 1, 2 and 3** With respect to indexes 1 and same as previous cases, the results are similar to the presented for m_p, hence the analysis is analog. In the case of index 2 it is shown that higher results are obtained, because of the effects of the LCL-filter, as presented in Figure 6.14.
- QQ**-Channel**
  - **Range 1** In this case, for lower frequencies, the asymptotic models describe a poor

performance, specially with respect to index 2, as the curves of the full Mpresent high dependency with respect to values of L_C, specially at low values.

– **Range 2 and 3** For medium and high frequencies, a good performance is presented by both index 1 and 2 of the asymptotic models with respect to the magnitude of the impedance, having in consideration the deviation produced by the LCL-filter. Nevertheless, a worse performance is presented with respect to the phase graphs.

Consistent with previous results, M2 is the one that better describes the characteristics of the small-signal impedance, with the exception of the QQ-channel. Having in consideration the deviations produced by the peak resonances, the magnitude graph is accurately and precisely determined by this model. With respect to the phase graphs, bigger indexes were obtained for higher frequencies, due to the deviation presented by the full-order model.

Table 6.21: Magnitude Graphs Indexes Results: L_C

Channel	Frequency Range	Asymptotic Limits	Index 1 [dB]	Index 2 [dB]	Channel	Frequency Range	Asymptotic Limits	Index 1 [dB]	Index 2 [dB]
$DD-Channel$	**Range 1**	**M1**	2.2553	14.0066	$DQ-Channel$	**Range 1**	**M1**	4.0405	4.7685
		M2	3.9071	4.4628			**M2**	4.0354	4.7685
		M3	2.2553	14.0066			**M3**	7.9802	8.0735
	Range 2	**M1**	0.7795	2.5607		**Range 2**	**M1**	2.0616	2.3257
		M2	1.2975	1.7077			**M2**	2.0566	2.3257
		M3	0.7795	2.5607			**M3**	6.0013	5.6305
	Range 3	**M1**	6.0665	5.1283		**Range 3**	**M1**	3.0016	4.6075
		M2	6.0665	5.1283			**M2**	3.0042	4.6075
		M3	6.0665	5.1283			**M3**	3.9439	4.0946
$QD-Channel$	**Range 1**	**M1**	46.0072	9.5357	$QQ-Channel$	**Range 1**	**M1**	3.3124	15.4503
		M2	0.0342	0.0068			**M2**	3.3124	15.4503
		M3	46.0072	9.5357			**M3**	3.3124	15.4503
	Range 2	**M1**	23.1787	8.5326		**Range 2**	**M1**	0.7795	2.8182
		M2	8.1664	3.7163			**M2**	0.7795	2.8182
		M3	23.1787	8.5326			**M3**	0.7795	2.8182
	Range 3	**M1**	3.0561	4.6698		**Range 3**	**M1**	6.0665	5.1283
		M2	3.3794	5.3132			**M2**	6.0665	5.1283
		M3	3.0561	4.6698			**M3**	6.0665	5.1283

6.3. Reference Frame Angle Sensitivity

As stated before, it was assumed for the obtained results that $\delta \approx 0$. However, this is not true, as it should be computed as presented in (2.16). Despite this, as microgrids and distribution systems in general present highly resistive lines, voltage phase angles does not deviate considerably, as in [34], where a modified IEEE 33-Bus distribution system is simulated, obtaining a deviation of less than 1 degree at every busbar.

In Figures 6.15 and 6.16 are presented the sensitivity analysis where the angle δ is forcedly evaluated from -10 to 10 degrees, ignoring (2.16), in order to identify the effects of changing the voltage angle, without modifying the impedance by the effects of changes in the voltages and currents. Figure 6.15 present the complete frequency range while Figure 6.16 focuses on the low-frequency range. The dashed line corresponds to the impedance value when $\delta = 0$.

Table 6.22: Phase Graphs Indexes Results: L_C

Channel	Frequency Range	Asymptotic Limits	Index 1 [°]	Index 2 [°]	Channel	Frequency Range	Asymptotic Limits	Index 1 [°]	Index 2 [°]
$DD-Channel$	**Range 1**	**M1**	2.7279	8.1637	$DQ-Channel$	**Range 1**	**M1**	0.1697	0.2304
		M2	2.4831	6.4299			**M2**	0.1697	0.2304
		M3	2.7279	8.1637			**M3**	0.1697	0.2304
	Range 2	**M1**	4.2211	19.4028		**Range 2**	**M1**	5.8424	6.9047
		M2	5.6646	9.9953			**M2**	5.8424	6.9047
		M3	4.2211	19.4028			**M3**	5.8424	6.9047
	Range 3	**M1**	40.7906	29.0387		**Range 3**	**M1**	146.9061	18.6928
		M2	40.8084	29.0744			**M2**	146.9061	18.6928
		M3	40.7906	29.0387			**M3**	146.9061	18.6928
$QD-Channel$	**Range 1**	**M1**	3.5344	0.0024	$QQ-Channel$	**Range 1**	**M1**	3.6552	10.1781
		M2	2.9122	0.0024			**M2**	3.6552	10.1781
		M3	3.5344	0.0024			**M3**	3.6552	10.1781
	Range 2	**M1**	66.9397	14.3932		**Range 2**	**M1**	4.8997	19.3714
		M2	32.3382	14.7442			**M2**	4.8997	19.3714
		M3	66.9397	14.3932			**M3**	4.8997	19.3714
	Range 3	**M1**	146.9908	18.8049		**Range 3**	**M1**	40.7914	29.0398
		M2	157.4332	27.6882			**M2**	40.7914	29.0398
		M3	146.9908	18.8049			**M3**	40.7914	29.0398

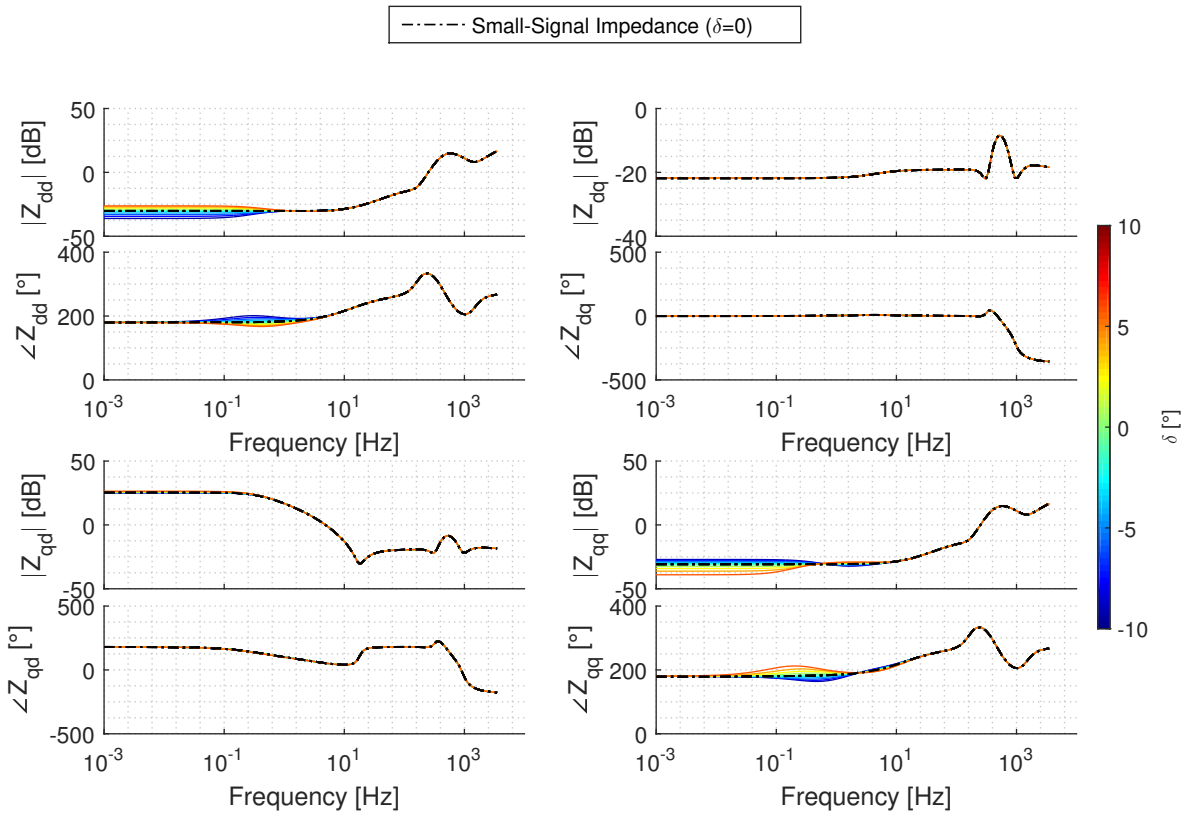

Figure 6.15: M6 Small-Signal Impedance Sensitivity: δ (Complete Frequency Range)

It can be noted that the principal affected are the channels DD and QQ, specially in the low-frequency range. As the angle δ increases, the magnitude of Z_{dd} also increases, while the magnitude of Z_{qq} decreases. The phases, on the other hand, experience a slight deviation

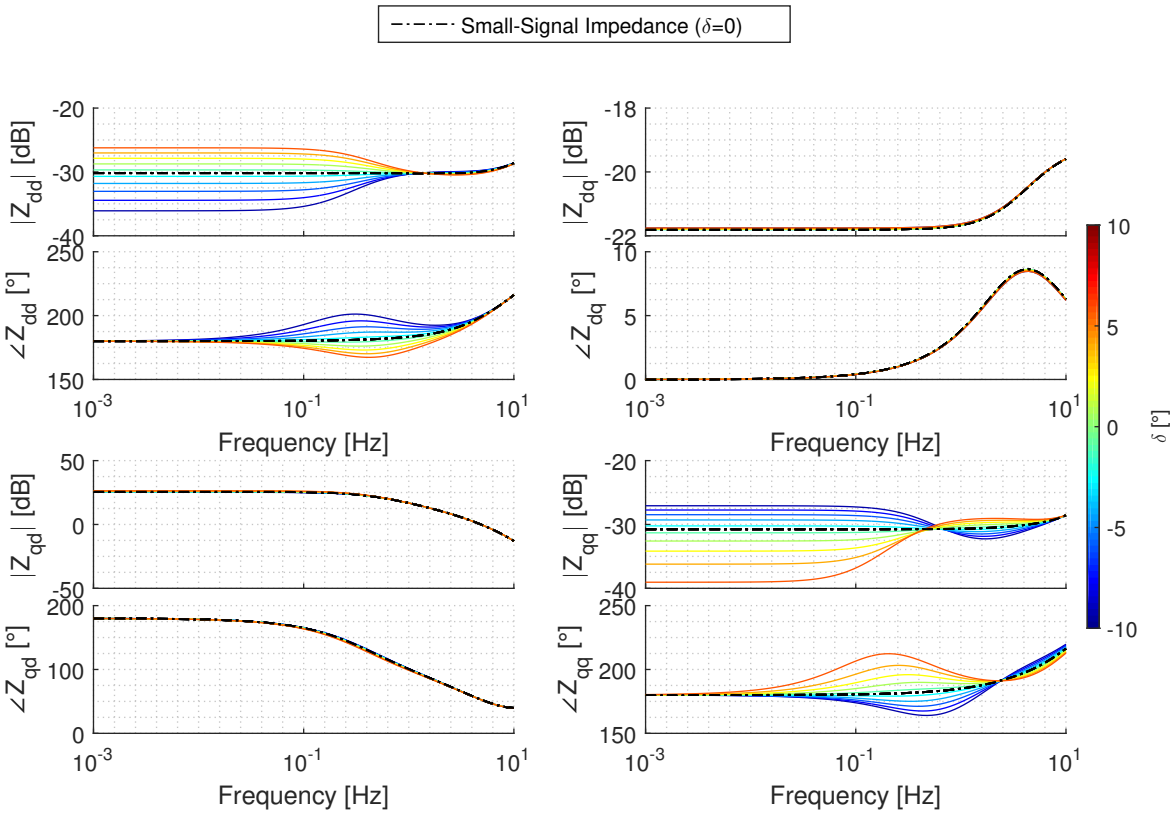

Figure 6.16: M6 Small-Signal Impedance Sensitivity: δ (Low-Frequency Range)

Table 6.23: Minimum and Maximum Reference Frame Angle for each Sensitivity Values

		I_{od}		I_{oq}		V_{bD}		$\overline{\omega}$		r_C		L_C	
	Base, m_p, n_q	**Min**	**Max**	**Min**	**Max**	**Min**	**Max**	**Min**	**Max**	**Min**	**Max**	**Min**	**Max**
δ [°]	-0,0359	-1,1978	1,9394	-0,1265	0,1676	-0,0379	-0,031	-0,041	-0,0284	-0,0811	0,0093	-0,0994	0,0272

that converges back to the dashed curve.

In the context of the study case, as the inverter is connected to the defined reference busbar, the angle δ is defined only by the output currents and voltages of the inverter, according to (2.16).

In Table 6.23 are presented the corresponding computed δ angles for each minimum and maximum sensitivity value, including the corresponding reference frame angle for the base case and for the droop gains, which do not change the angle value when swept.

It can be noted that, considering that the larger reference frame angle value is less than 2 degrees in this case, and based on the results shown in Figure 6.16, the results are barely affected by changes in δ, as the larger difference generated by $\mid \delta \mid \approx 2$ is 0,95 dB.

Chapter 7

Conclusions

Throughout this work, it was confirmed the hypothesis that sensitivity of droop-controlled inverters can be analytically characterized by the transfer functions of the linearized reduced-order inverter models. By treating the linearized small-signal impedances of the simplified inverter models as MIMO-system transfer functions, approximate log-magnitude asymptotic curves were computed. As these curves can be constructed only by the zero frequency value, the poles and the zeros, analytical expressions, involving the internal parameters and the electrical variables evaluated in the operating point, were developed.

By comparing the differences between the small-signal impedances of the different six models, an approach about the influence of each subsystem of the inverter in the small-signal impedance was obtained. It can be concluded that the active-power droop control has a deeper impact on the QD-channel, as well as affecting the initial value of the magnitude curve, while the reactive-power droop control impacts the DQ-channel deeper. The inclusion of the LC-filter generates a peak in the filter resonance frequency, and by considering the measuring low-pass filter another resonance peak appears in the QD-channel.

Notwithstanding the simplifications, a good characterization of the small-signal impedances of the full model of the inverter was developed, through the log-magnitude asymptotic curves of the simplified models, specifically by M2. Despite the presented differences, a good approach about the impact of each operating variable and internal parameter was obtained, as validated through a real study case. In general terms, M2 performs the best with respect to the other models, with the exception of the low-frequency range of the DD-Channel, where a slightly worse performance is determined by the developed indexes.

The results also indicate that principally is the low-frequency range of the small-signal impedance that gets affected by changes in the operating conditions, as the high-frequency range tends to converge to the large-signal impedance. Particularly in the high-frequency range of the DQ and QD-Channels, a major deviation is present between the impedance phase angle of the full-order and the simplified models, induced by the LCL-filter resonance peak.

Additionally, the dependence of the obtained results on the reference frame angle δ was

analyzed. Changes in δ mainly affect the low-frequency range of the DD and QQ channels, increasing the DD-channel impedance and decreasing the QQ-channel impedance as δ increase. As in microgrids and distribution systems the lines are mainly resistive, no large voltage angles are expected, hence the results are not expected to be significantly altered.

Considering the magnitude order of the studied critical parameters, the results could lead to determine which operating variable has deepest impact on the small-signal impedance. Hence, this work could lead to improved small-signal stability studies, in which one of the biggest problems nowadays is the dependence of the small-signal impedance on the changing operating point, and where the influence of the droop-controlled inverters has barely been studied.

7.1. Future Work

Despite the promising results of this thesis work, there are still several tasks to keep working. Particularly, it is necessary to first analyze the results experimentally. It would be interesting to apply small-signal measuring techniques to compare the computed results of the Huatacondo case with the real small-signal impedance behavior.

As presented by the indexes results, the QQ-Channel could not be effectively characterized. Nevertheless, similarities with the results of DD-Channel can be observed. These similarities must be further explored in order to characterize this channel in particular.

Another interesting aspect is the analysis of the frequency-channel related transfer function presented in Section 2.5.2. Once the small-signal impedance related channels are characterized, in order to fully analyze the small-signal stability of the droop-controlled inverter, the frequency channel must be firstly identified and modeled, and then also characterized in order to understand its sensitivity to the operating point conditions.

Finally, once the droop-controlled inverter is fully characterized, it would be interesting to extrapolate these results to a full inverter-driven microgrid. In order to do this, it would be necessary to also consider the models of grid-forming and grid-feeding inverters, and their impact on the final microgrid impedance, considering also others microgrid elements and characteristics, as topology, loads, protections and controllers.

Chapter 8

Bibliography

[1] B. Yu, J. Guo, C. Zhou, Z. Gan, J. Yu, and F. Lu, "A review on microgrid technology with distributed energy," in *2017 International Conference on Smart Grid and Electrical Automation (ICSGEA)*, May 2017, pp. 143–146.

[2] R. Majumder, "Some aspects of stability in microgrids," *IEEE Transactions on Power Systems*, vol. 28, no. 3, pp. 3243–3252, Aug 2013.

[3] P. A. Mendoza-Araya and G. Venkataramanan, "Impedance matching based stability criteria for ac microgrids," in *2014 IEEE Energy Conversion Congress and Exposition (ECCE)*, Sept 2014, pp. 1558–1565.

[4] R. Turner, S. Walton, and R. Duke, "A case study on the application of the nyquist stability criterion as applied to interconnected loads and sources on grids," *IEEE Transactions on Industrial Electronics*, vol. 60, no. 7, pp. 2740–2749, July 2013.

[5] R. D. Middlebrook, "Input filter considerations in design and application switching regualtors," *IEEE IAS'76*, 1976.

[6] C. M. Wildrick, F. C. Lee, B. H. Cho, and B. Choi, "A method of defining the load impedance specification for a stable distributed power system," *IEEE Transactions on Power Electronics*, vol. 10, no. 3, pp. 280–285, May 1995.

[7] X. Feng, J. Liu, and F. C. Lee, "Impedance specifications for stable dc distributed power systems," *IEEE Transactions on Power Electronics*, vol. 17, no. 2, pp. 157–162, March 2002.

[8] S. D. Sudhoff, S. F. Glover, P. T. Lamm, D. H. Schmucker, and D. E. Delisle, "Admittance space stability analysis of power electronic systems," *IEEE Transactions on Aerospace and Electronic Systems*, vol. 36, no. 3, pp. 965–973, July 2000.

[9] Z. Liu, J. Liu, W. Bao, and Y. Zhao, "Infinity-norm of impedance-based stability criterion for three-phase AC distributed power systems with constant power loads," *IEEE Transactions on Power Electronics*, vol. 30, no. 6, pp. 3030–3043, 2015.

[10] M. Belkhayat, "STABILITY CRITERIA FOR AC POWER SYSTEMS WITH REGULATED LOADS," Ph.D. dissertation, Purdue University, 1997.

[11] K. Jiang and X. Ge, "An improved forbidden-region-based criterion of vehicle-grid system," in *2017 IEEE Transportation Electrification Conference and Expo, Asia-Pacific, ITEC Asia-Pacific 2017*, 2017.

[12] Z. Liu, J. Liu, D. Boroyevich, R. Burgos, and T. Liu, "Small-signal terminal-characteristics modeling of three-phase droop-controlled inverters," in *2016 IEEE Energy Conversion Congress and Exposition (ECCE)*, Sept 2016, pp. 1–7.

[13] Z. Liu, J. Liu, D. Boroyevich, and R. Burgos, "Stability criterion of droop-controlled parallel inverters based on terminal-characteristics of individual inverters," in *2016 IEEE 8th International Power Electronics and Motion Control Conference (IPEMC-ECCE Asia)*, May 2016, pp. 2958–2963.

[14] B. Lasseter, "Microgrids [distributed power generation]," in *2001 IEEE Power Engineering Society Winter Meeting. Conference Proceedings (Cat. No.01CH37194)*, vol. 1, Jan 2001, pp. 146–149 vol.1.

[15] R. H. Lasseter, "Microgrids," in *2002 IEEE Power Engineering Society Winter Meeting. Conference Proceedings (Cat. No.02CH37309)*, vol. 1, 2002, pp. 305–308 vol.1.

[16] *IEEE Guide for Design, Operation, and Integration of Distributed Resource Island Systems with Electric Power Systems*, IEEE Std. 1547.4-2011, July 2011.

[17] Office of Electricity Delivery and Energy Reliability Smart Grid R&D Program, "DOE microgrid workshop report," August 2011.

[18] M. Ding, Y. Zhang, and M. Mao, "Key technologies for microgrids-a review," in *2009 International Conference on Sustainable Power Generation and Supply*, April 2009, pp. 1–5.

[19] IEEE PES Power System Dynamic Performance Committee and IEEE PES Task Force on Microgid Stability Analysis and Modeling, "Microgrid Stability Definitions, Analysis, and Modeling," IEEE Power & Energy Society, Tech. Rep. PES-TR66, 2018.

[20] A. Engler and N. Soultanis, "Droop control in lv-grids," in *2005 International Conference on Future Power Systems*, Nov 2005, pp. 6 pp.–6.

[21] D. Semënov, G. Mirzaeva, C. D. Townsend, and G. C. Goodwin, "A battery storage control scheme for ac microgrids," in *2017 20th International Conference on Electrical Machines and Systems (ICEMS)*, Aug 2017, pp. 1–6.

[22] N. Pogaku, M. Prodanovic, and T. C. Green, "Modeling, analysis and testing of autonomous operation of an inverter-based microgrid," *IEEE Transactions on Power Electronics*, vol. 22, no. 2, pp. 613–625, March 2007.

[23] D. E. Olivares, A. Mehrizi-Sani, A. H. Etemadi, C. A. Cañizares, R. Iravani, M. Kaze-

rani, A. H. Hajimiragha, O. Gomis-Bellmunt, M. Saeedifard, R. Palma-Behnke, G. A. Jiménez-Estévez, and N. D. Hatziargyriou, "Trends in microgrid control," *IEEE Transactions on Smart Grid*, vol. 5, no. 4, pp. 1905–1919, July 2014.

[24] J. Rocabert, A. Luna, F. Blaabjerg, and P. Rodríguez, "Control of power converters in ac microgrids," *IEEE Transactions on Power Electronics*, vol. 27, no. 11, pp. 4734–4749, Nov 2012.

[25] N. Pogaku, M. Prodanovic, and T. C. Green, "Modeling, analysis and testing of autonomous operation of an inverter-based microgrid," *IEEE Transactions on Power Electronics*, vol. 22, no. 2, pp. 613–625, March 2007.

[26] ——, "Inverter-based microgrids: small-signal modelling and testing," in *The 3rd IET International Conference on Power Electronics, Machines and Drives, 2006. PEMD 2006*, April 2006, pp. 499–504.

[27] S. M. Kaviri, M. Pahlevani, P. Jain, and A. Bakhshai, "A review of ac microgrid control methods," in *2017 IEEE 8th International Symposium on Power Electronics for Distributed Generation Systems (PEDG)*, April 2017, pp. 1–8.

[28] U. B. Tayab, M. A. B. Roslan, L. J. Hwai, and M. Kashif, "A review of droop control techniques for microgrid," *Renewable and Sustainable Energy Reviews*, vol. 76, pp. 717 – 727, 2017. [Online]. Available: http://www.sciencedirect.com/science/article/pii/S1364032117303453

[29] M. C. Chandorkar, D. M. Divan, and R. Adapa, "Control of parallel connected inverters in standalone ac supply systems," *IEEE Transactions on Industry Applications*, vol. 29, no. 1, pp. 136–143, Jan 1993.

[30] P. Kundur, J. Paserba, V. Ajjarapu, G. Andersson, A. Bose, C. Canizares, N. Hatziargyriou, D. Hill, A. Stankovic, C. Taylor, T. V. Cutsem, and V. Vittal, "Definition and classification of power system stability ieee/cigre joint task force on stability terms and definitions," *IEEE Transactions on Power Systems*, vol. 19, no. 3, pp. 1387–1401, Aug 2004.

[31] J. Lai, C. Hu, G. Li, X. Lu, and H. Zhou, "Networked-based distributed cooperative voltage control for power electronics interfaced microgrids," in *2016 IEEE 11th Conference on Industrial Electronics and Applications (ICIEA)*, June 2016, pp. 1880–1885.

[32] E. Barklund, N. Pogaku, M. Prodanovic, C. Hernandez-Aramburo, and T. C. Green, "Energy management in autonomous microgrid using stability-constrained droop control of inverters," *IEEE Transactions on Power Electronics*, vol. 23, no. 5, pp. 2346–2352, Sept 2008.

[33] K. Ogata, *Ingeniería de control moderna*, 5th ed. Ribera del Loira 28 28042, Madrid, España: Pearson Educación, S.A., 2010.

[34] L. Luo, W. Gu, Y. Wang, and C. Chen, "An affine arithmetic-based power flow algorithm considering the regional control of unscheduled power fluctuation," *Energies*, vol. 10, p.

1794, 11 2017.

Appendix A

Numerical Assessment

A.1. M1: Ideal Source

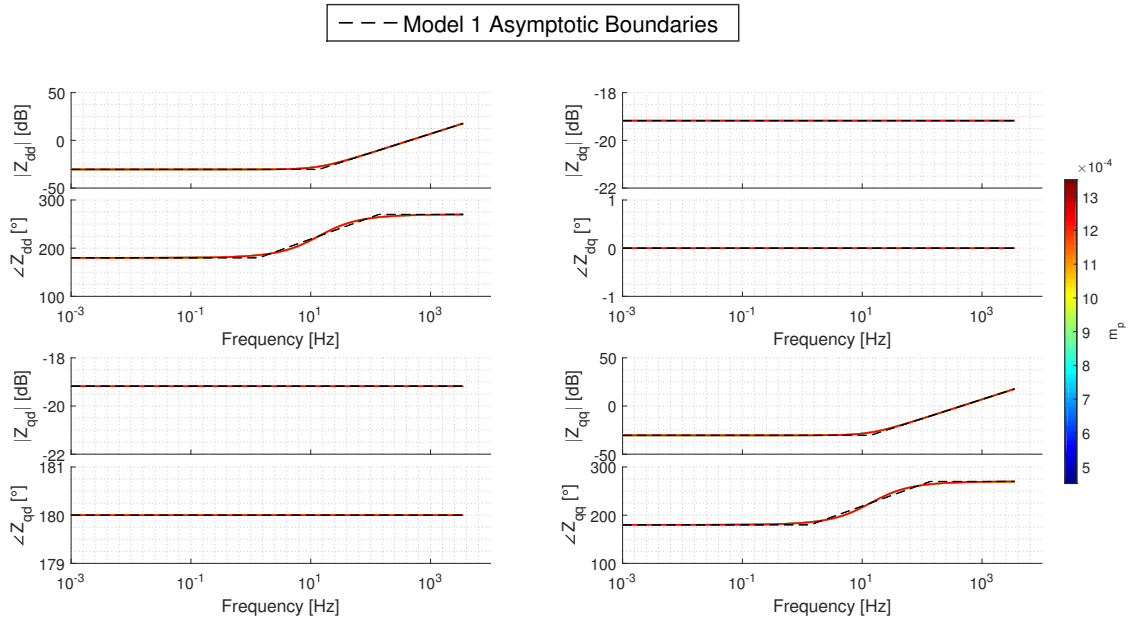

Figure A.1: M1 Small-Signal Impedance Sensitivity: m_p

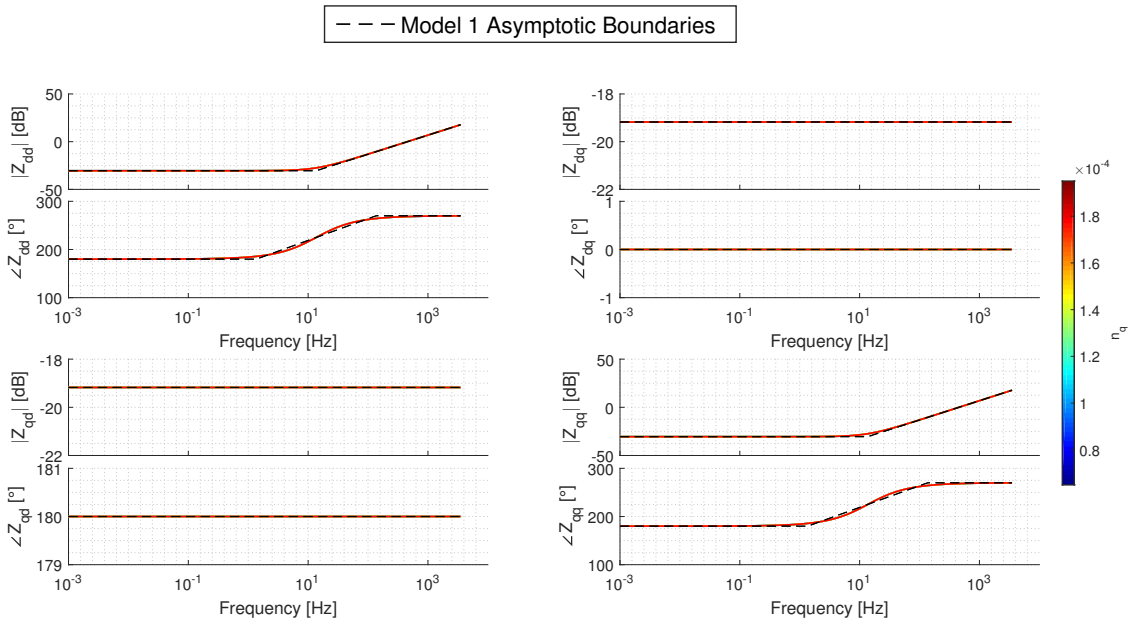

Figure A.2: M1 Small-Signal Impedance Sensitivity: n_q

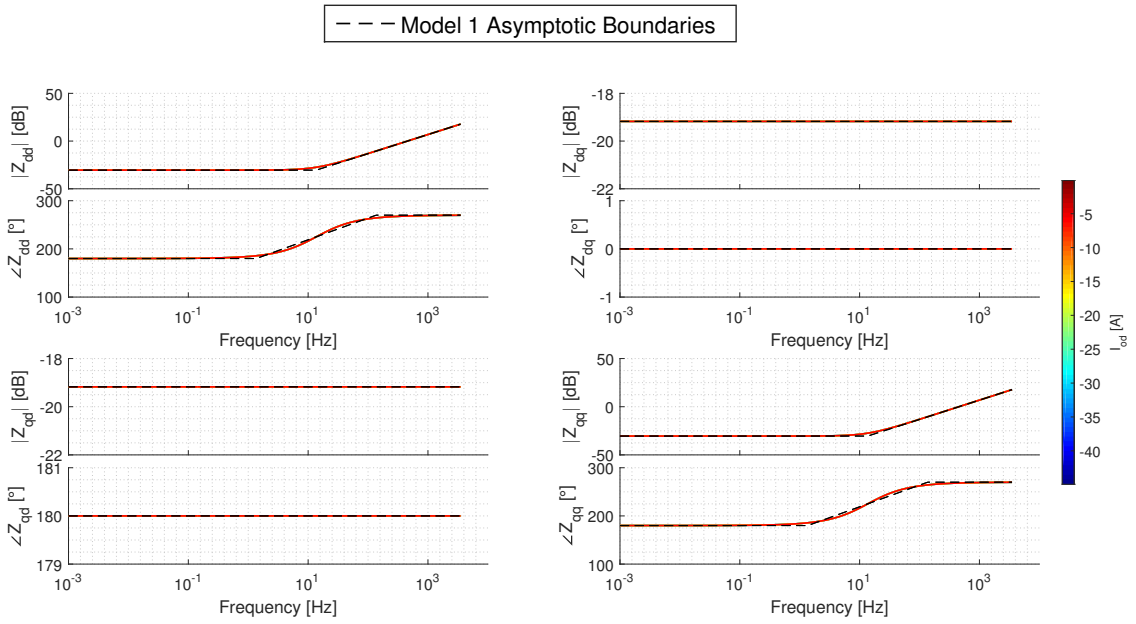

Figure A.3: M1 Small-Signal Impedance Sensitivity: $I_{od} < 0$

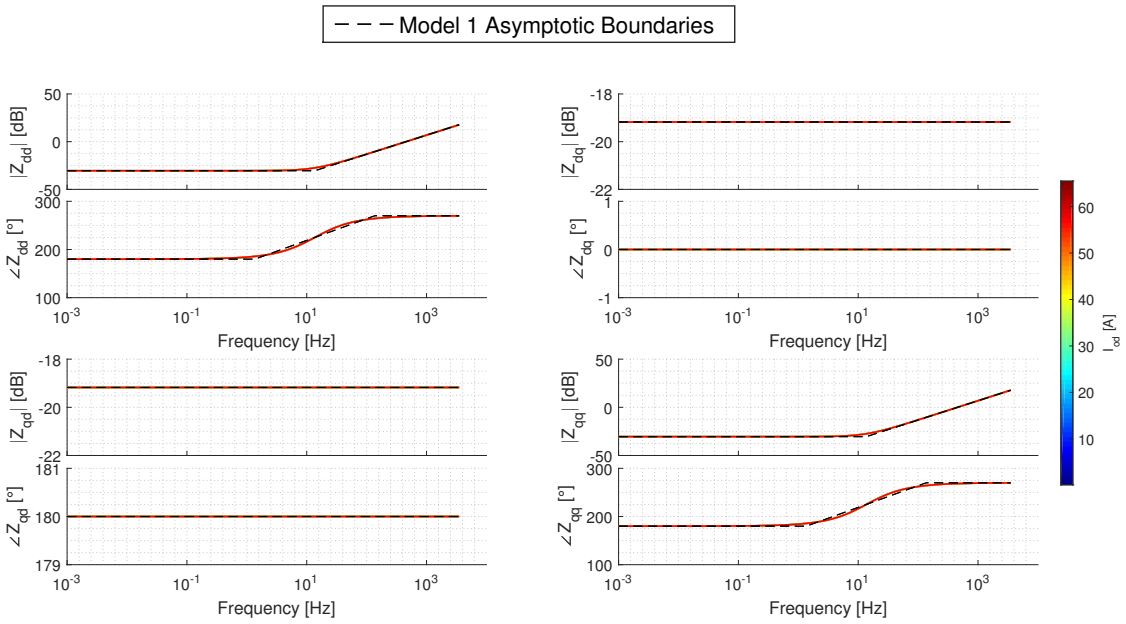

Figure A.4: M1 Small-Signal Impedance Sensitivity: $I_{od} > 0$

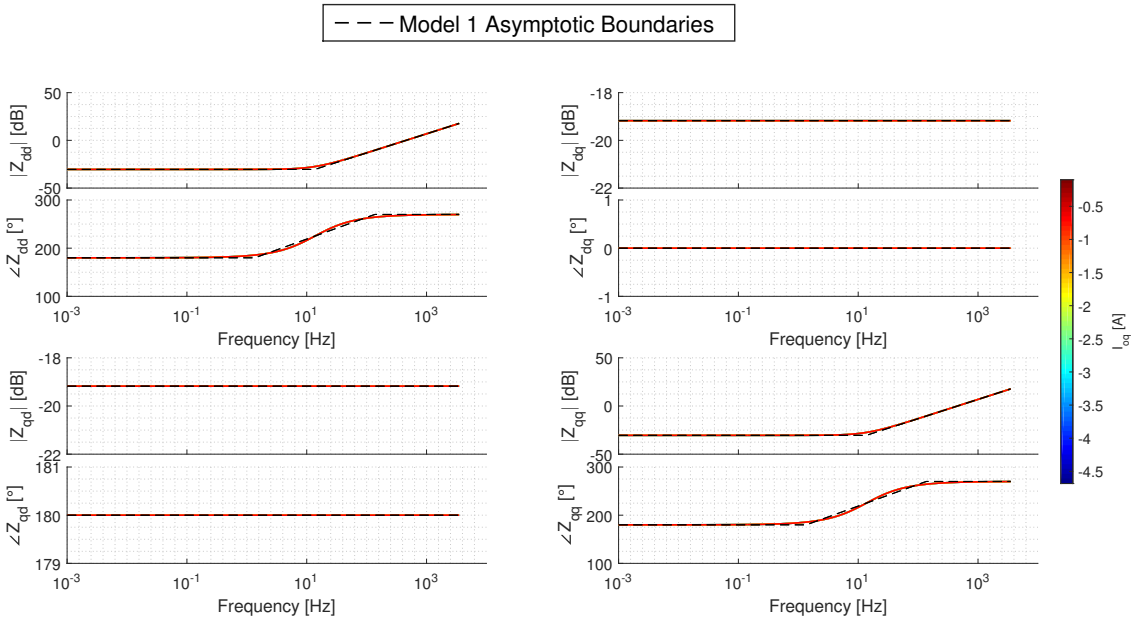

Figure A.5: M1 Small-Signal Impedance Sensitivity: $I_{oq} < 0$

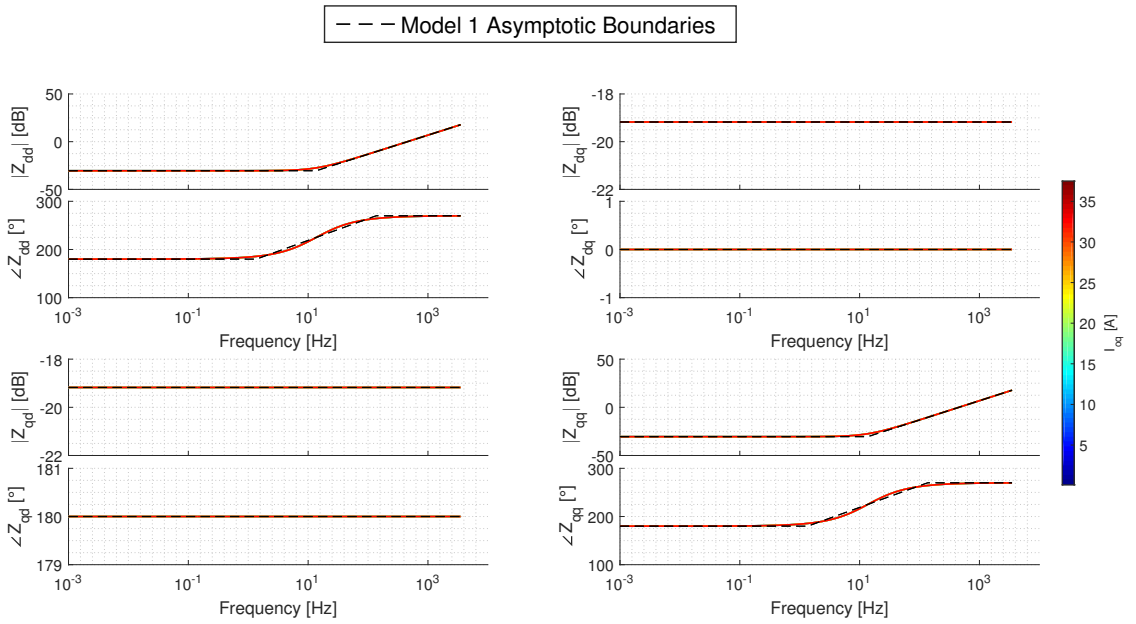

Figure A.6: M1 Small-Signal Impedance Sensitivity: $I_{oq} > 0$

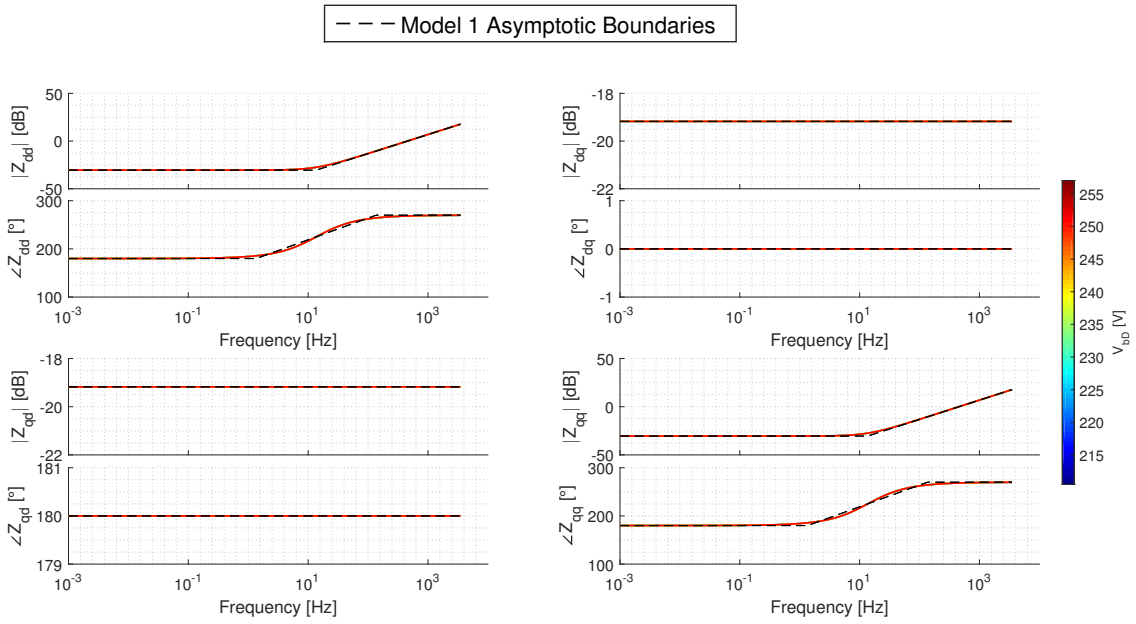

Figure A.7: M1 Small-Signal Impedance Sensitivity: V_{bD}

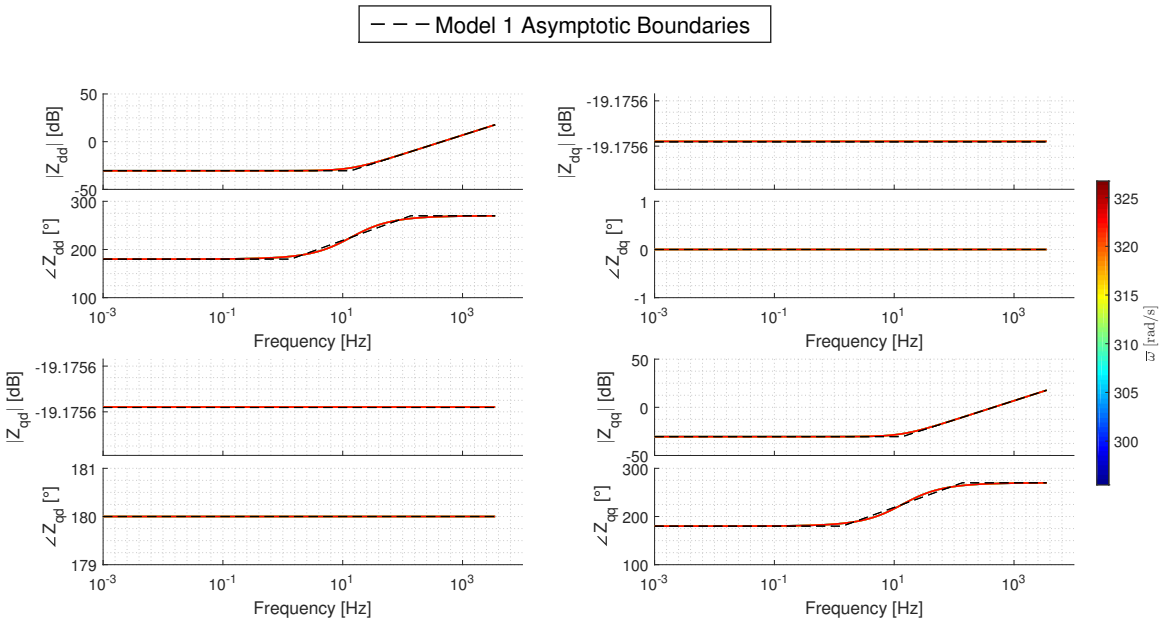

Figure A.8: M1 Small-Signal Impedance Sensitivity: $\overline{\omega}$

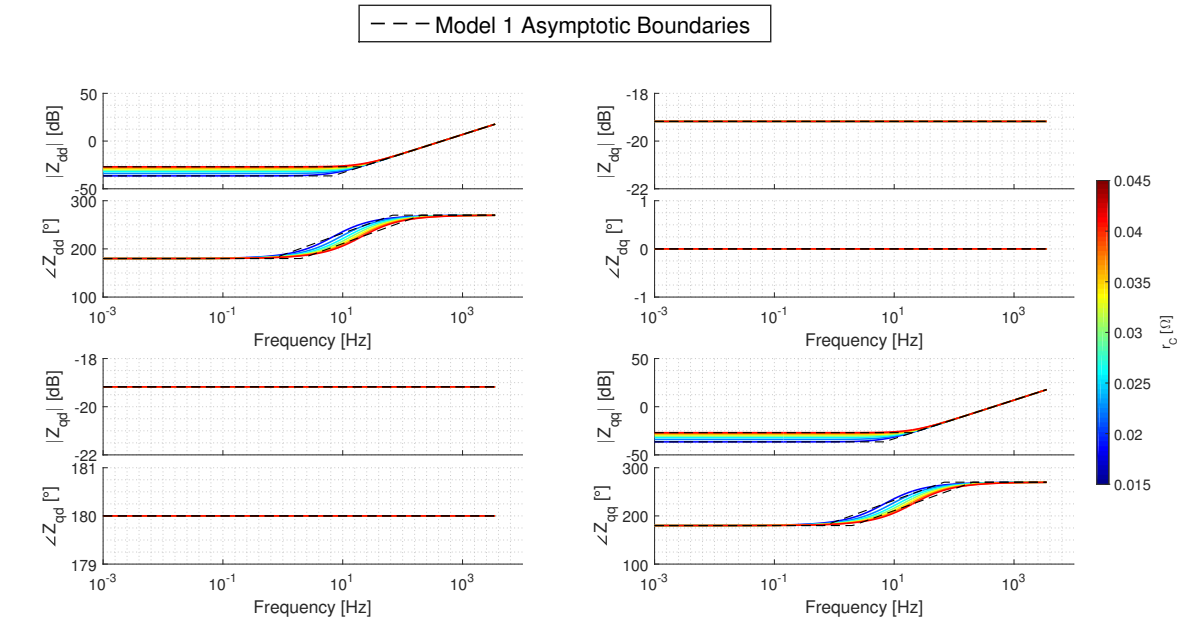

Figure A.9: M1 Small-Signal Impedance Sensitivity: r_C

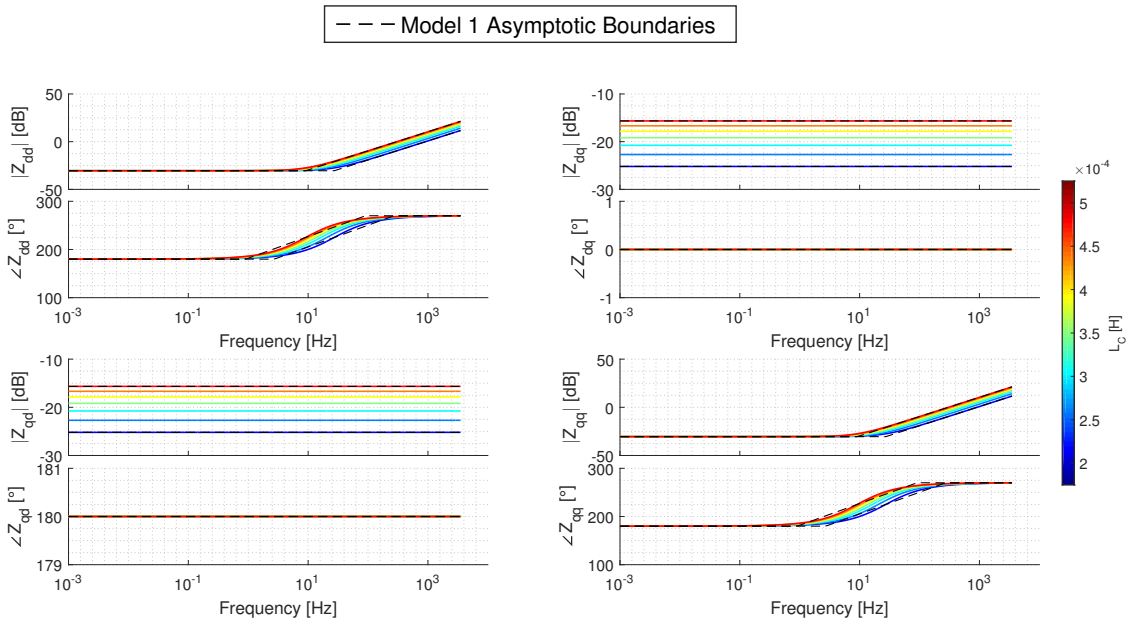

Figure A.10: M1 Small-Signal Impedance Sensitivity: L_C

A.2. M2: Active Power Droop-Controlled Source

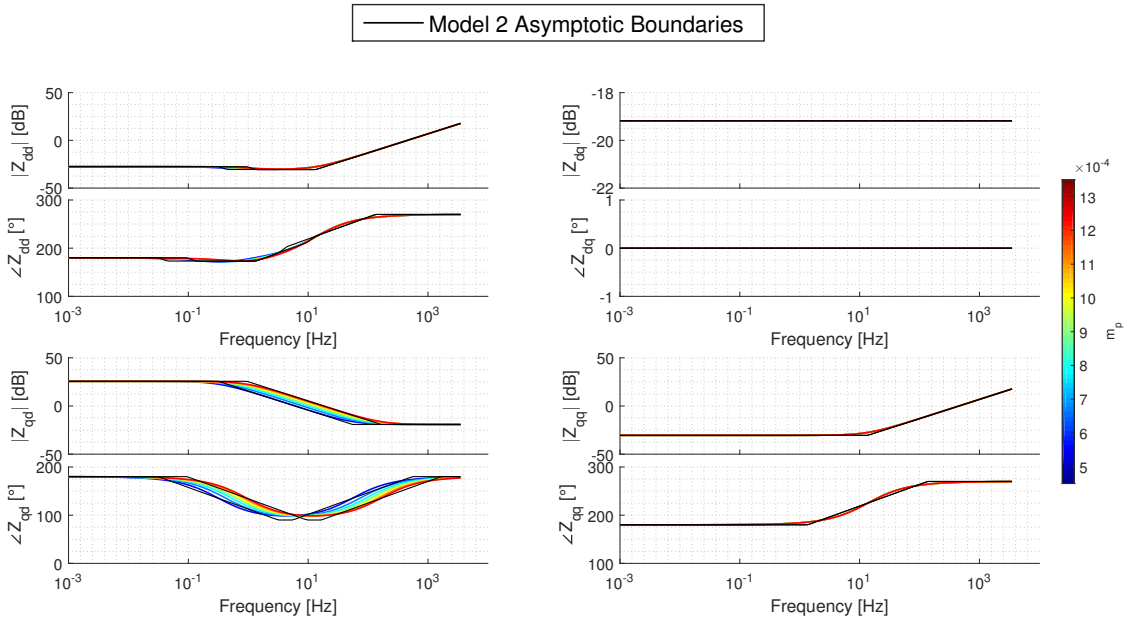

Figure A.11: M2 Small-Signal Impedance Sensitivity: m_p

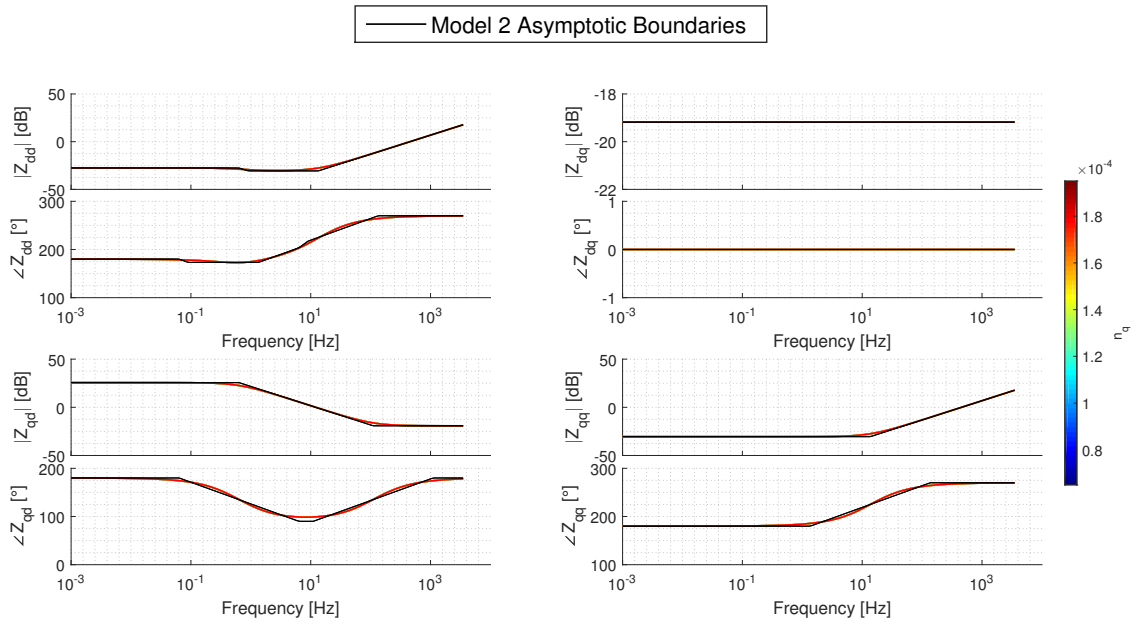

Figure A.12: M2 Small-Signal Impedance Sensitivity: n_q

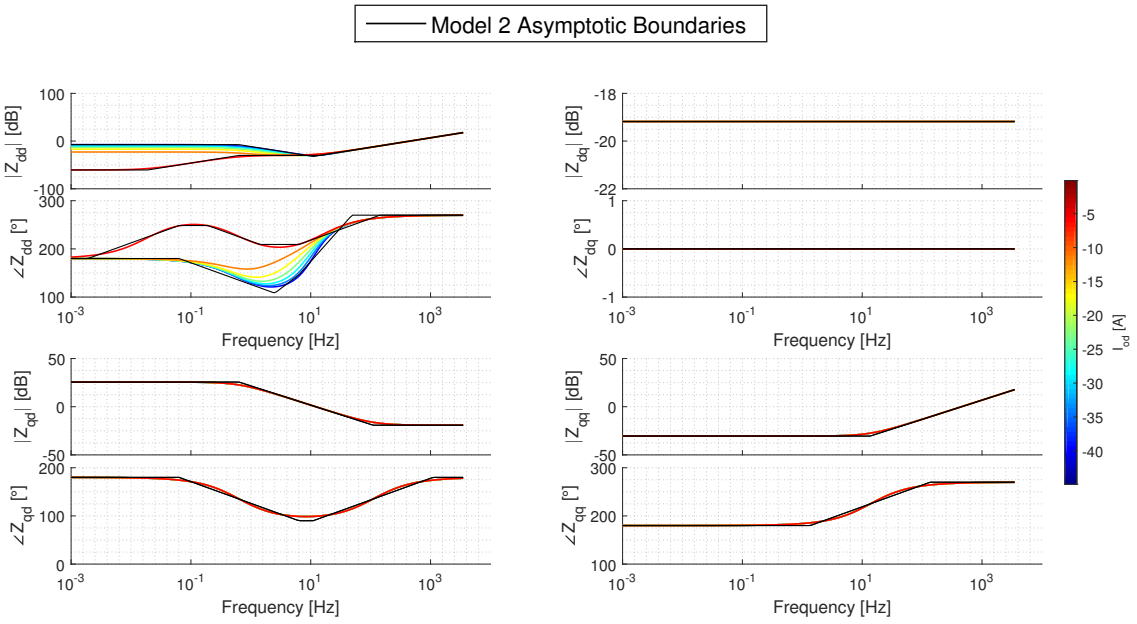

Figure A.13: M2 Small-Signal Impedance Sensitivity: $I_{od} < 0$

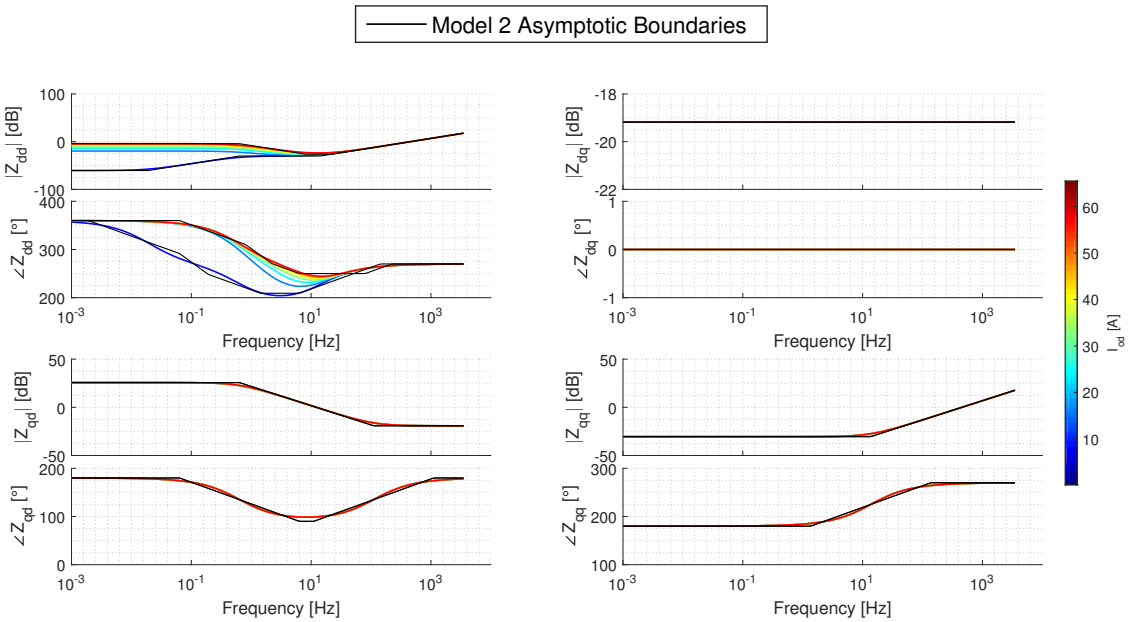

Figure A.14: M2 Small-Signal Impedance Sensitivity: $I_{od} > 0$

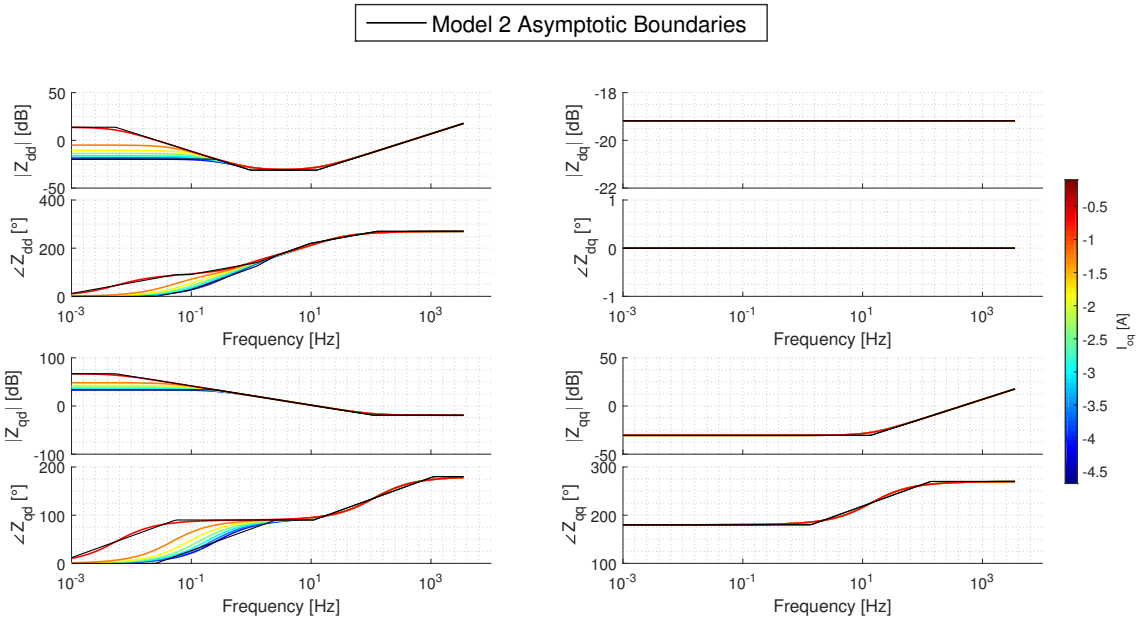

Figure A.15: M2 Small-Signal Impedance Sensitivity: $I_{oq} < 0$

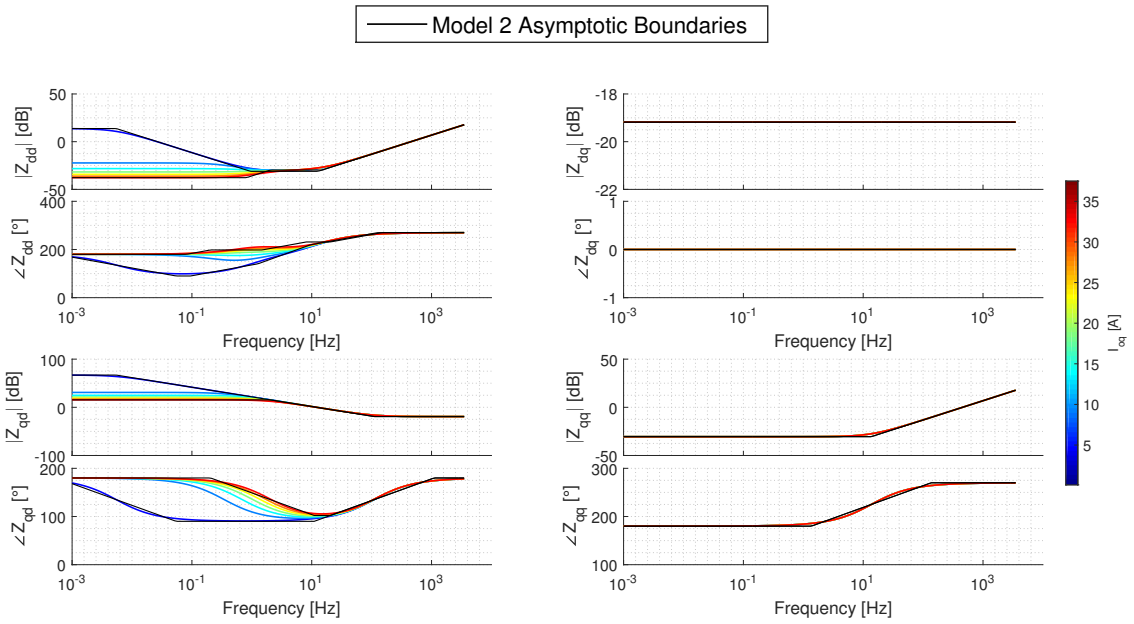

Figure A.16: M2 Small-Signal Impedance Sensitivity: $I_{oq} > 0$

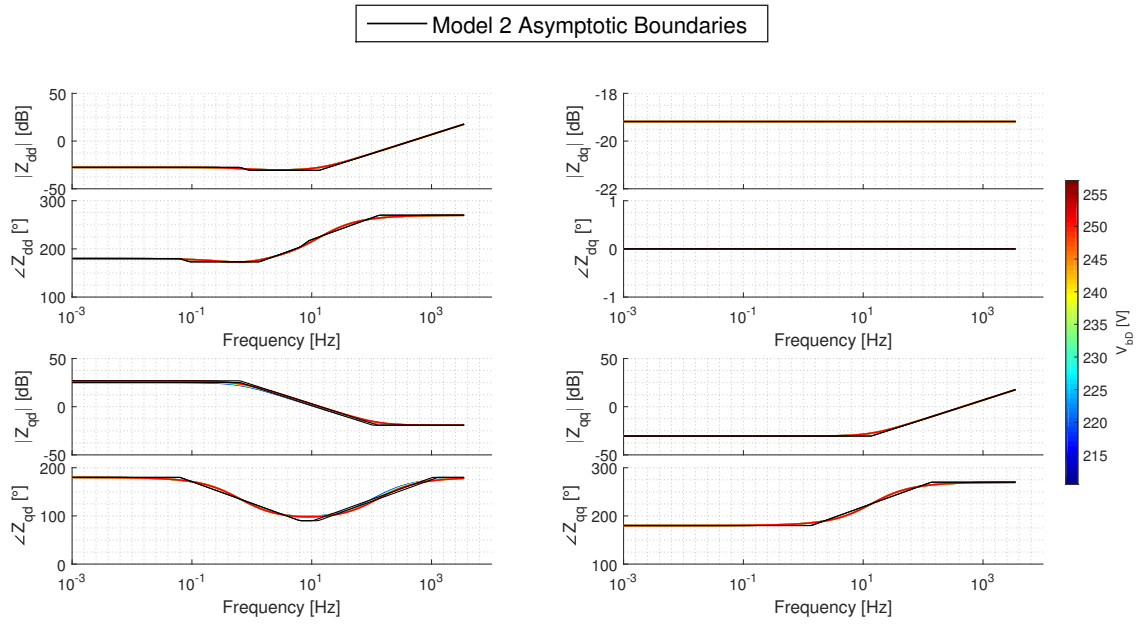

Figure A.17: M2 Small-Signal Impedance Sensitivity: V_{bD}

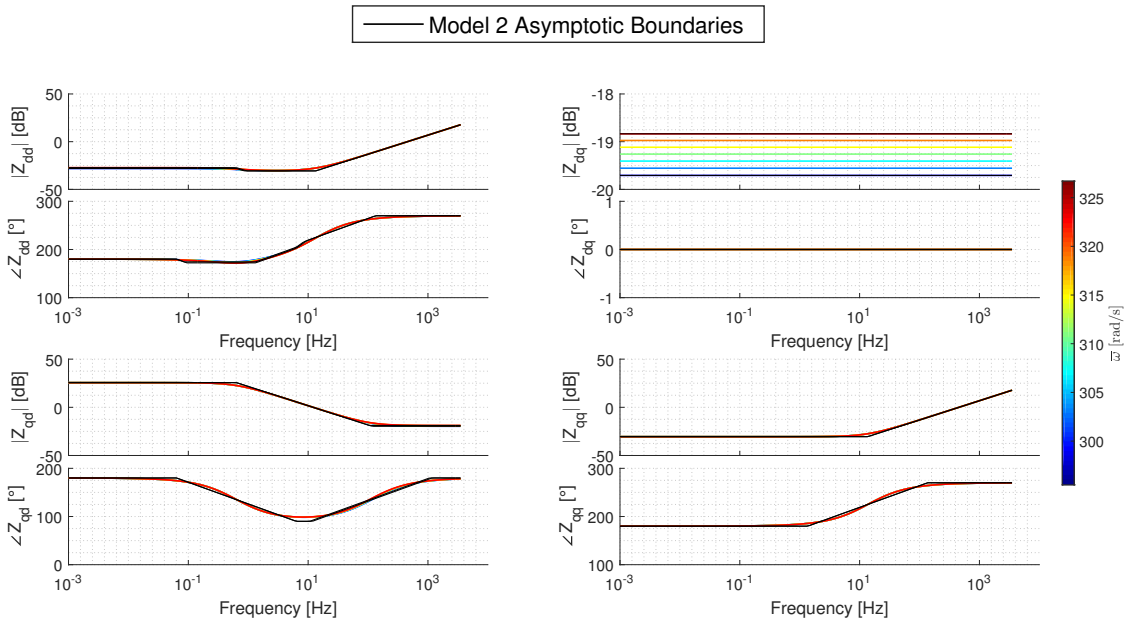

Figure A.18: M2 Small-Signal Impedance Sensitivity: $\overline{\omega}$

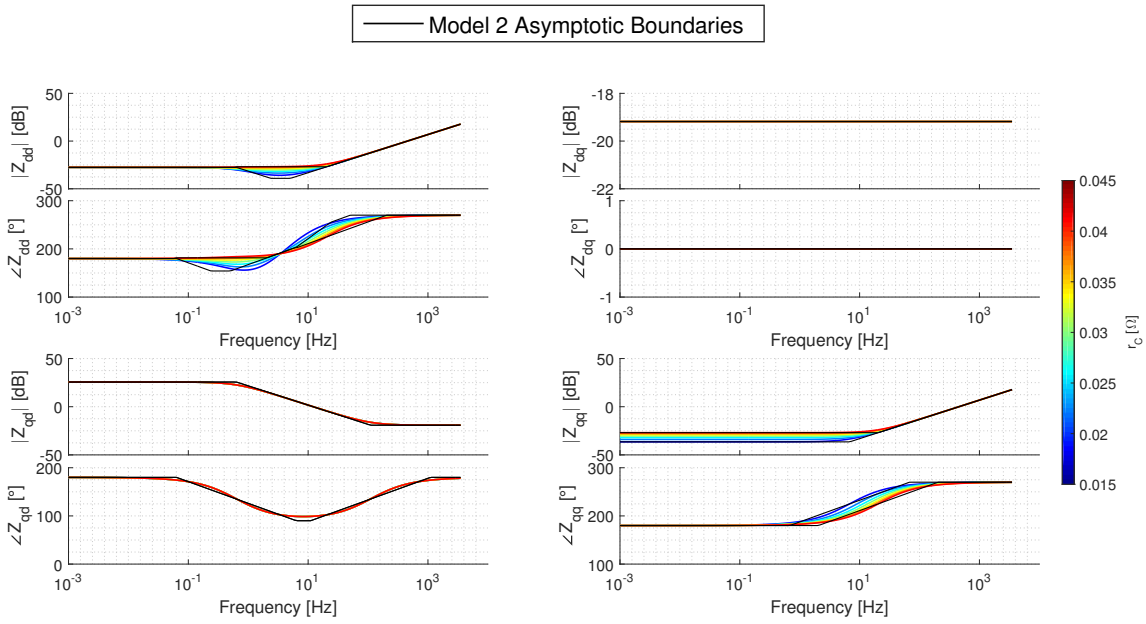

Figure A.19: M2 Small-Signal Impedance Sensitivity: r_C

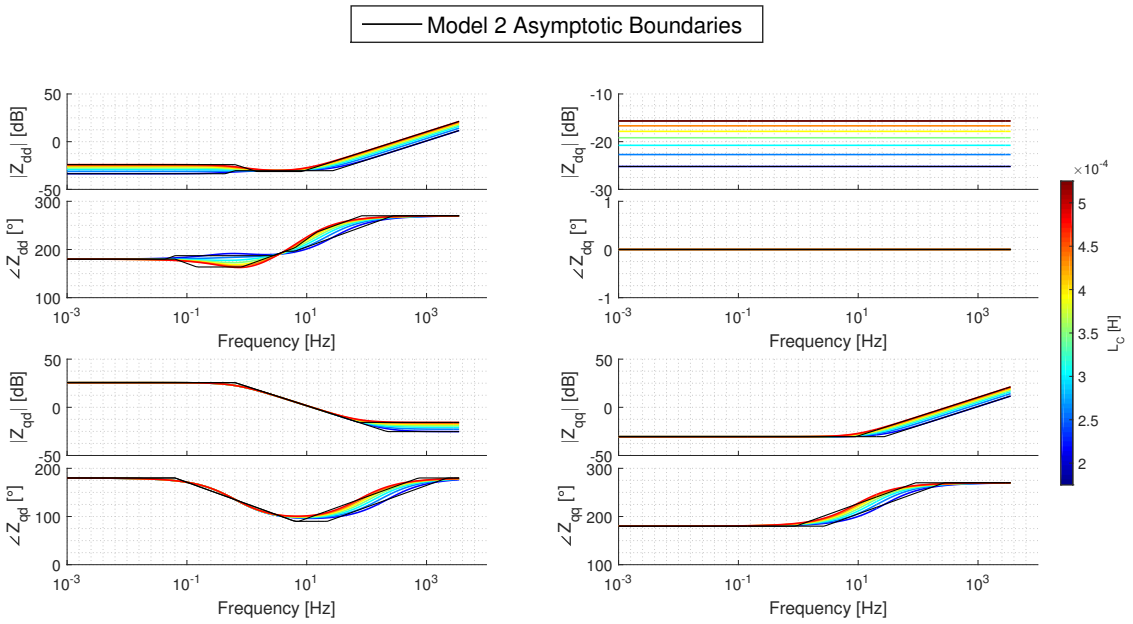

Figure A.20: M2 Small-Signal Impedance Sensitivity: L_C

A.3. M3: Reactive Power Droop-Controlled Source

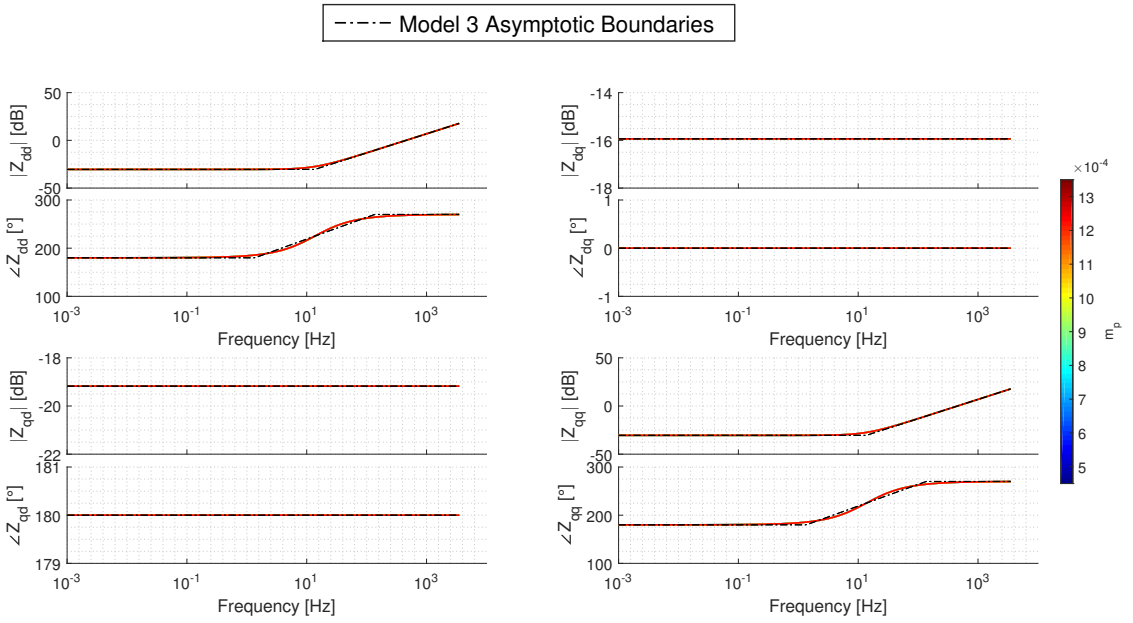

Figure A.21: M3 Small-Signal Impedance Sensitivity: m_p

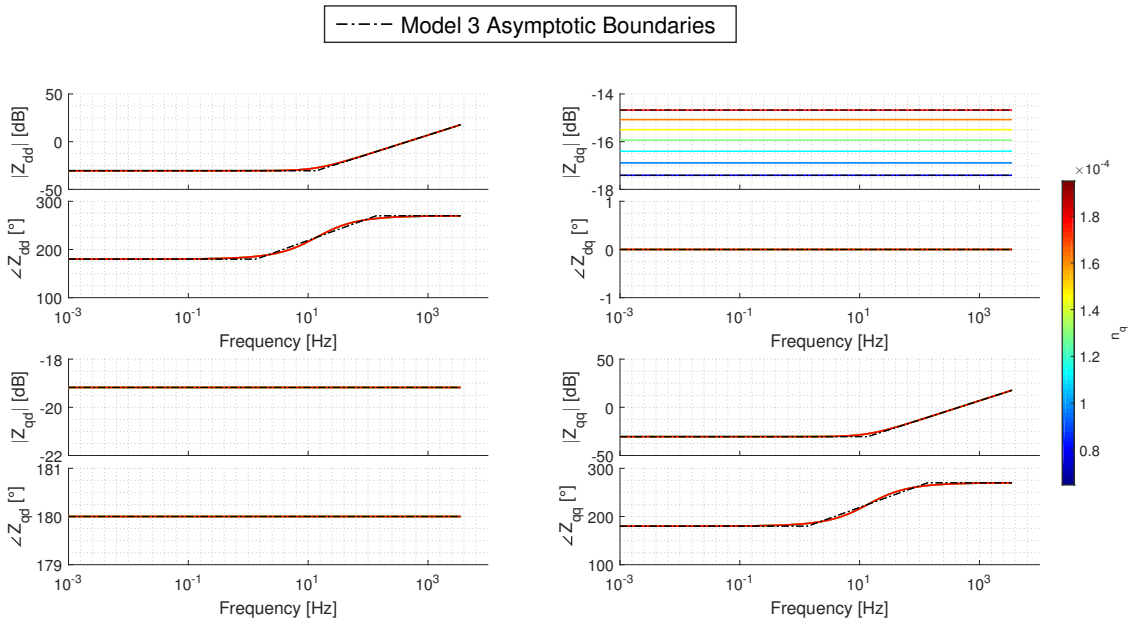

Figure A.22: M3 Small-Signal Impedance Sensitivity: n_q

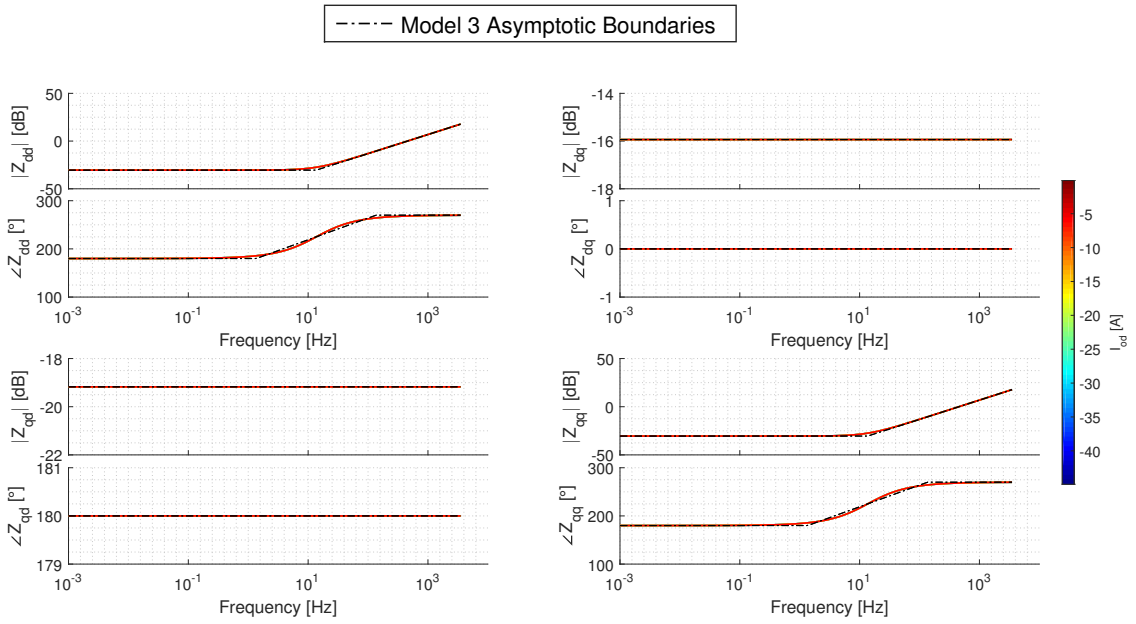

Figure A.23: M3 Small-Signal Impedance Sensitivity: $I_{od} < 0$

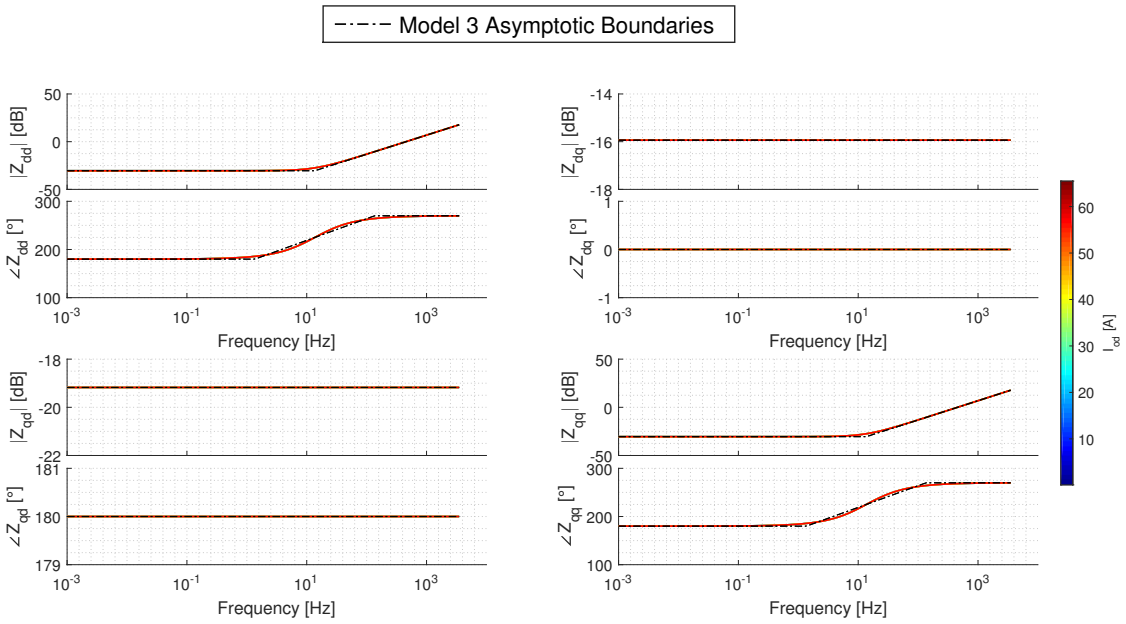

Figure A.24: M3 Small-Signal Impedance Sensitivity: $I_{od} > 0$

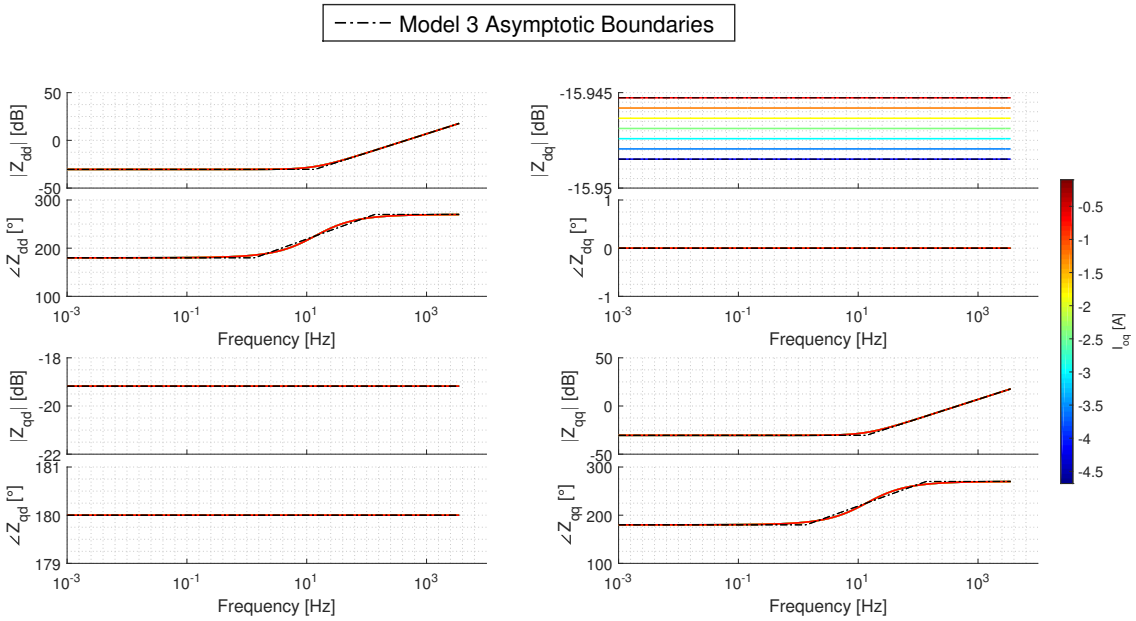

Figure A.25: M3 Small-Signal Impedance Sensitivity: $I_{oq} < 0$

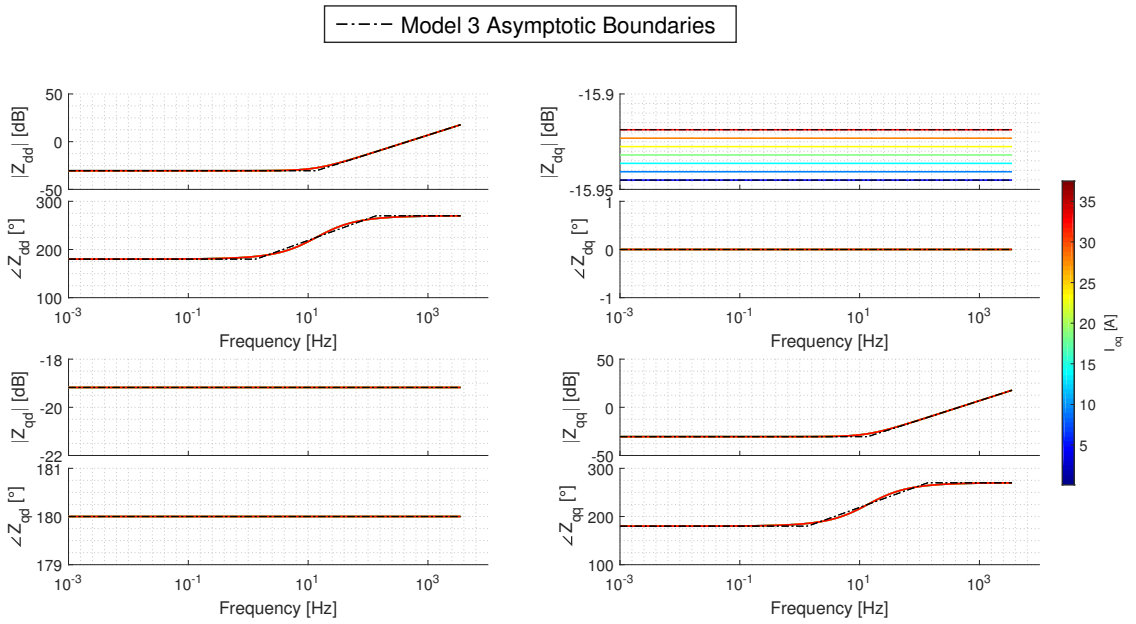

Figure A.26: M3 Small-Signal Impedance Sensitivity: $I_{oq} > 0$

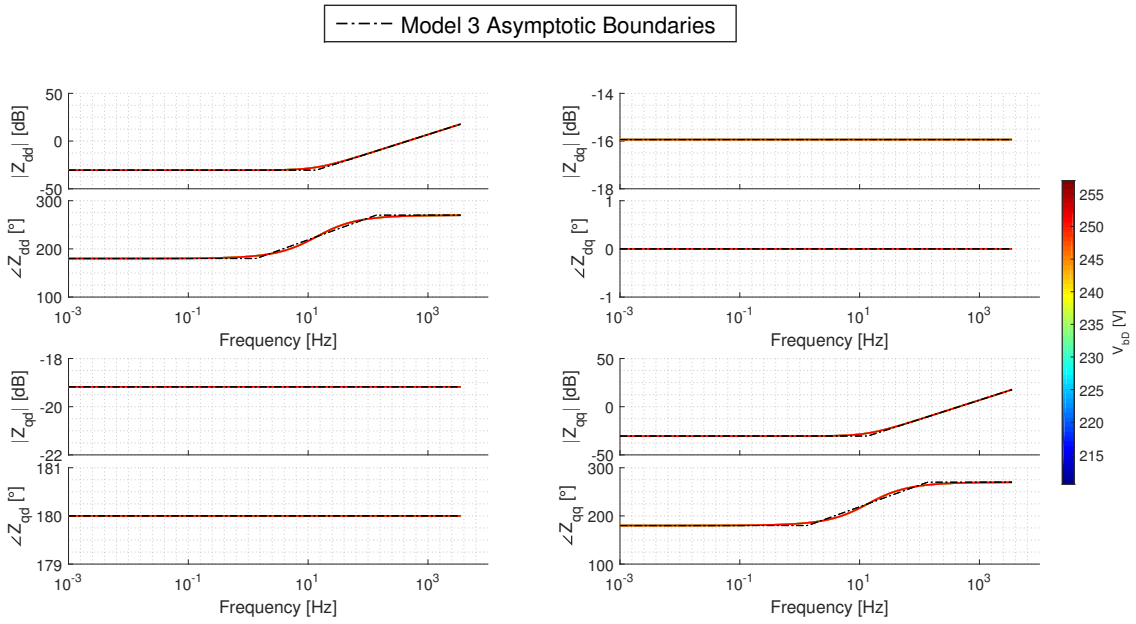

Figure A.27: M3 Small-Signal Impedance Sensitivity: V_{bD}

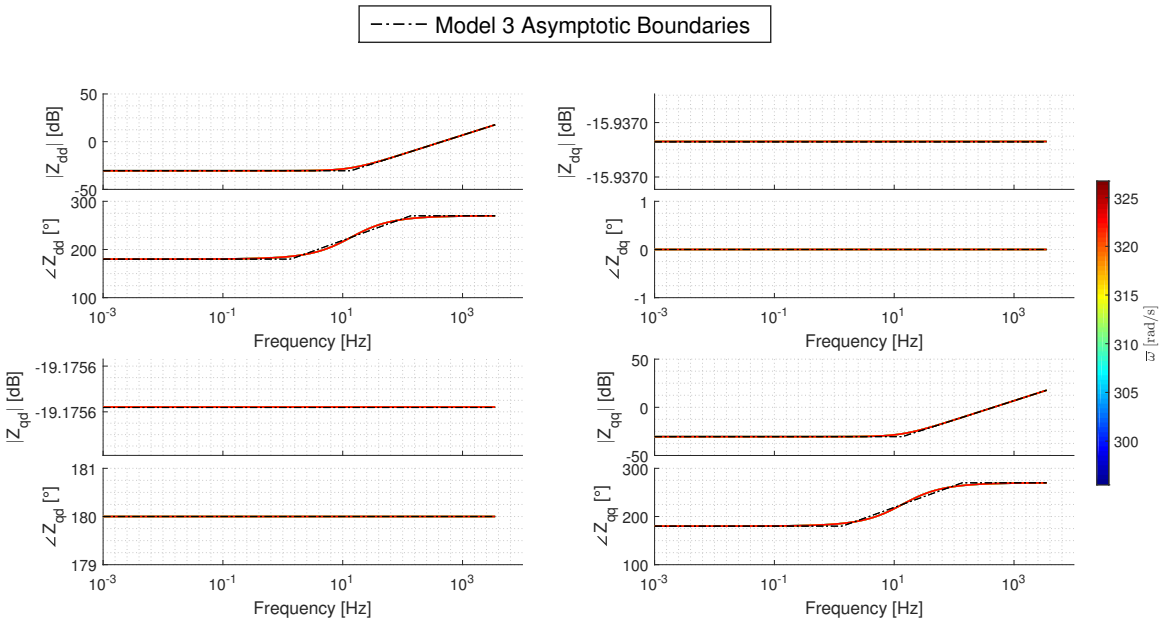

Figure A.28: M3 Small-Signal Impedance Sensitivity: $\overline{\omega}$

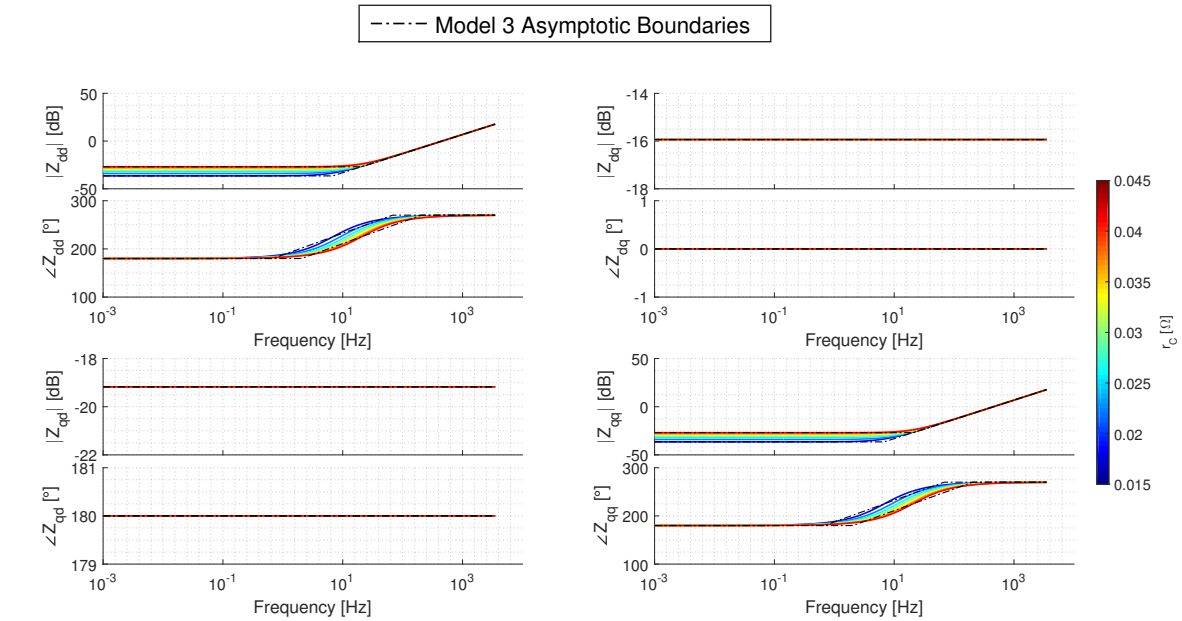

Figure A.29: M3 Small-Signal Impedance Sensitivity: r_C

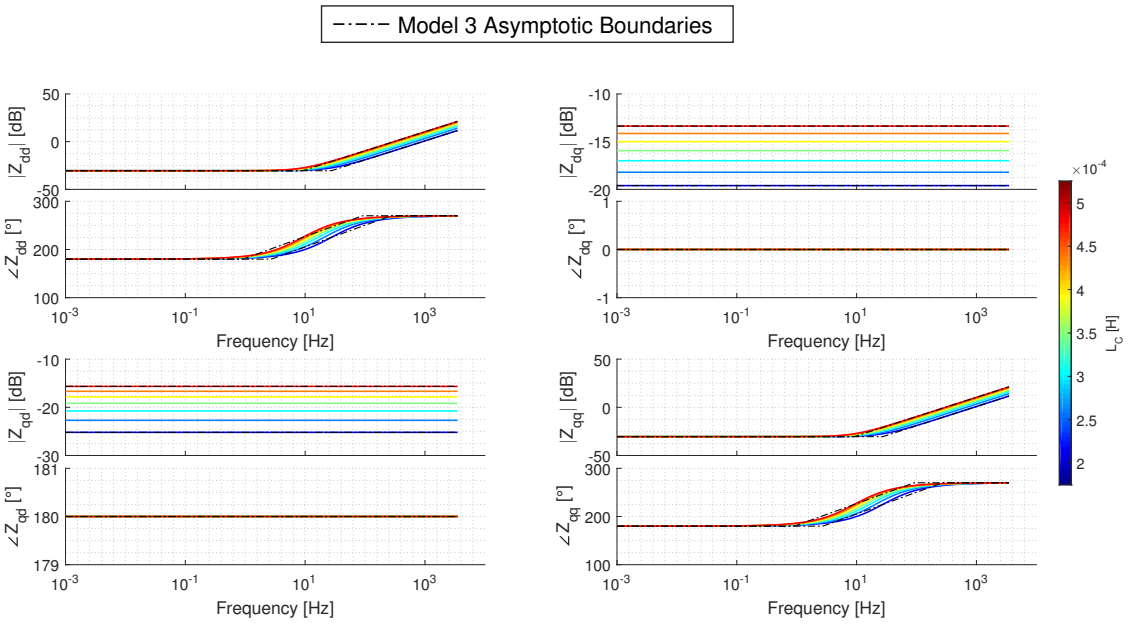

Figure A.30: M3 Small-Signal Impedance Sensitivity: L_C

A.4. M4: Active and Reactive Power Droop Controlled Source

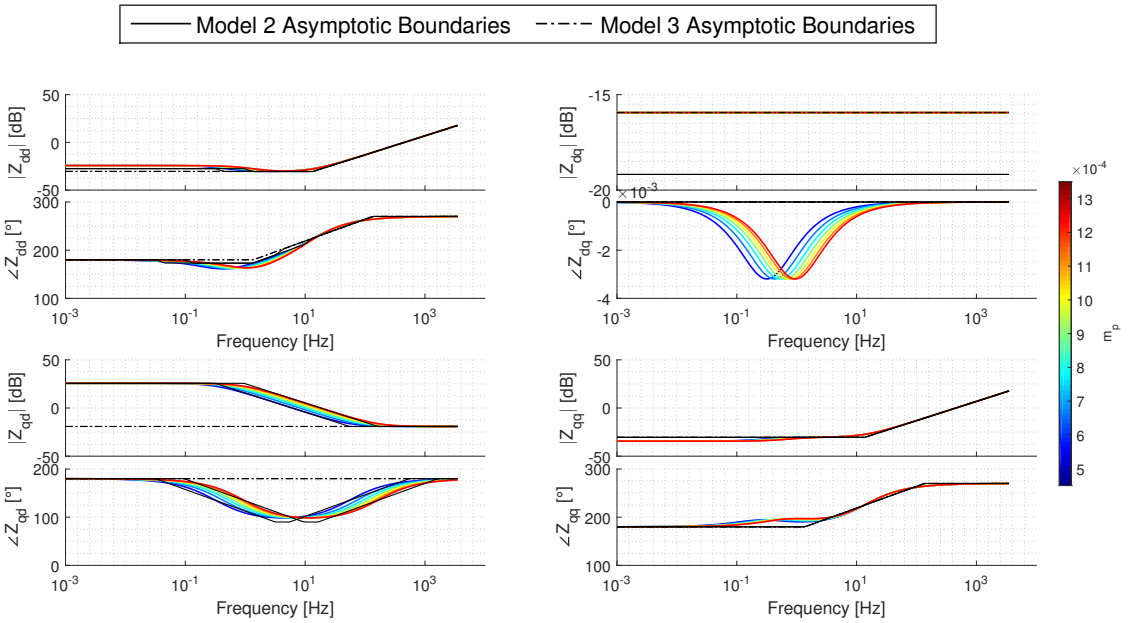

Figure A.31: M4 Small-Signal Impedance Sensitivity: m_p

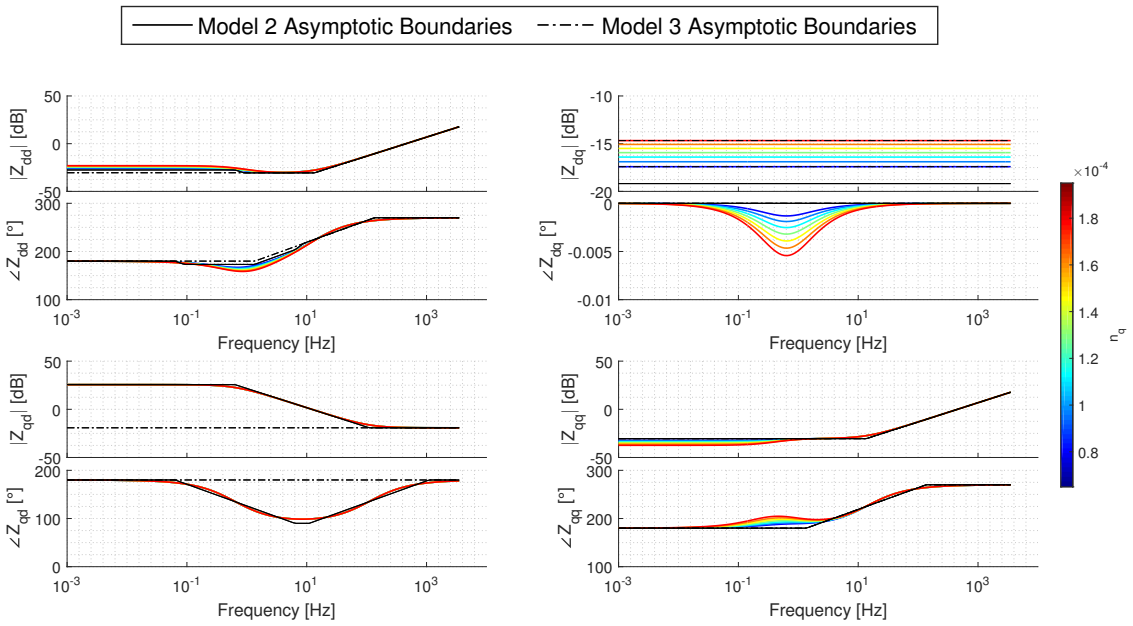

Figure A.32: M4 Small-Signal Impedance Sensitivity: n_q

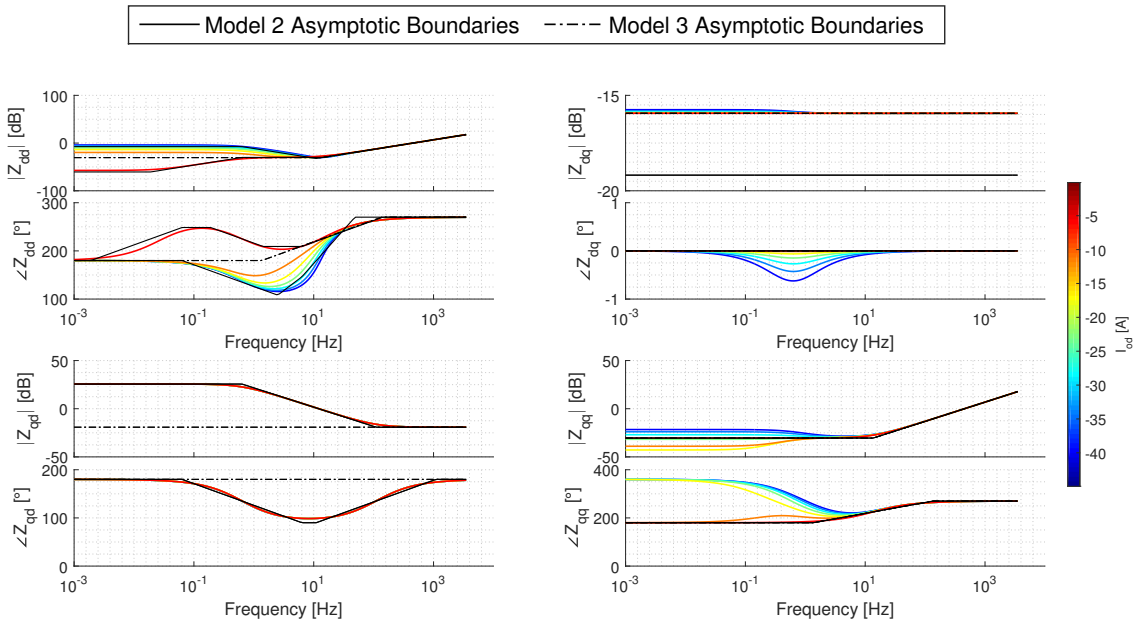

Figure A.33: M4 Small-Signal Impedance Sensitivity: $I_{od} < 0$

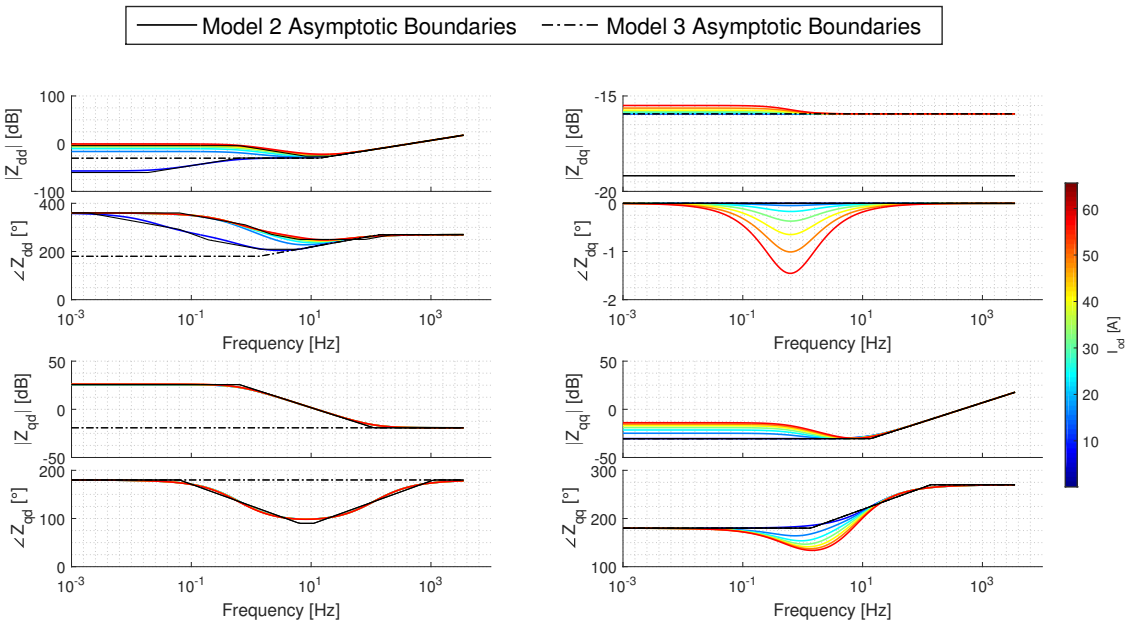

Figure A.34: M4 Small-Signal Impedance Sensitivity: $I_{od} > 0$

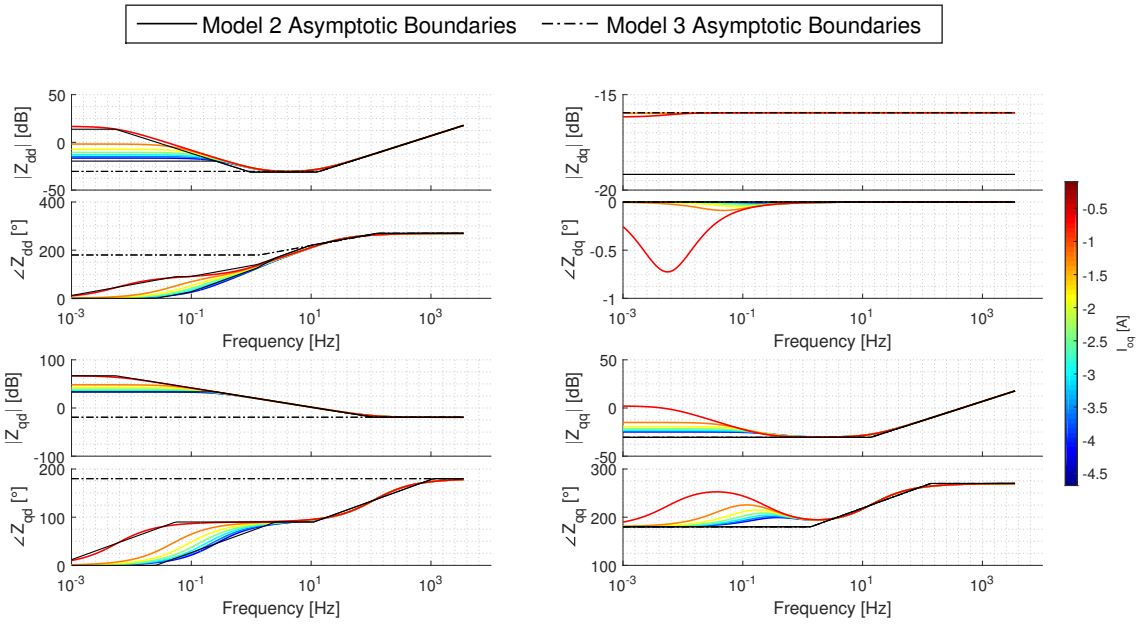

Figure A.35: M4 Small-Signal Impedance Sensitivity: $I_{oq} < 0$

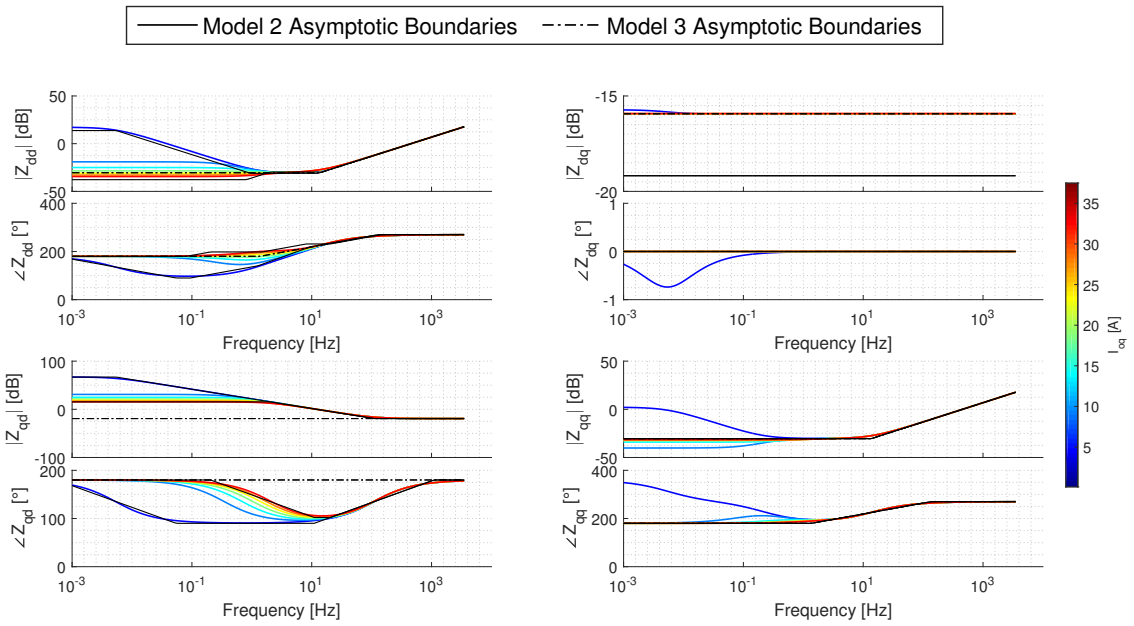

Figure A.36: M4 Small-Signal Impedance Sensitivity: $I_{oq} > 0$

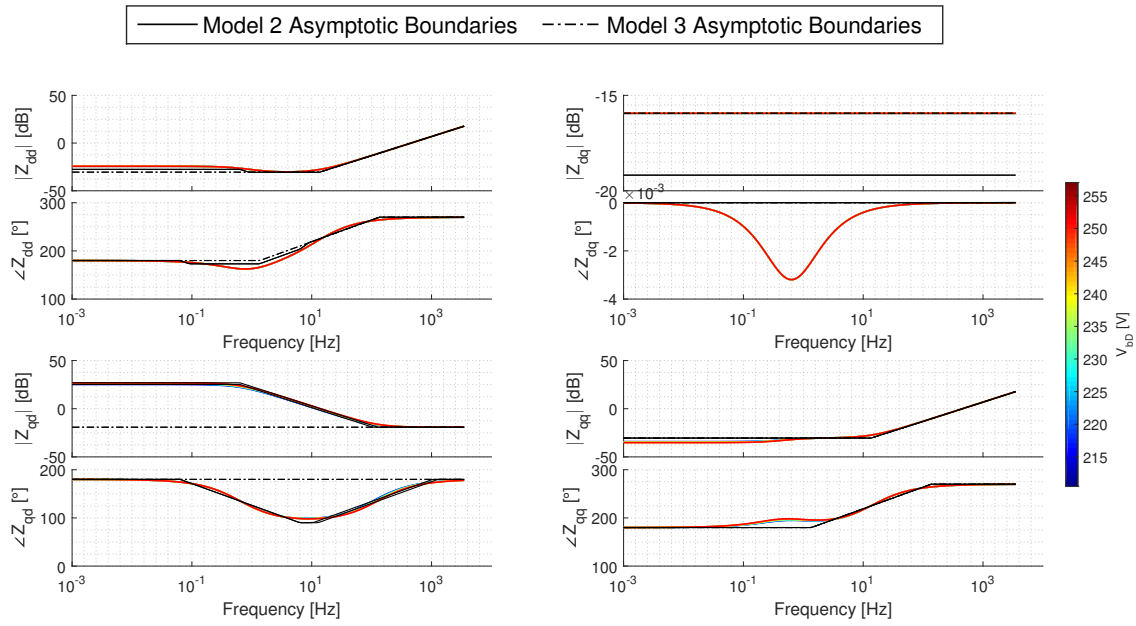

Figure A.37: M4 Small-Signal Impedance Sensitivity: V_{bD}

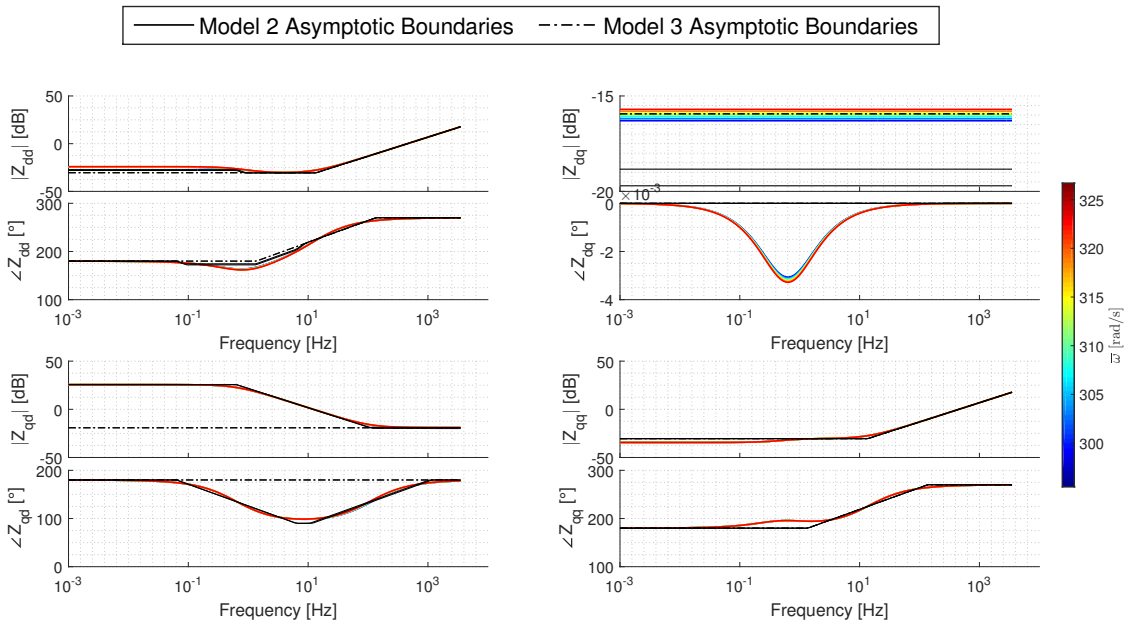

Figure A.38: M4 Small-Signal Impedance Sensitivity: $\overline{\omega}$

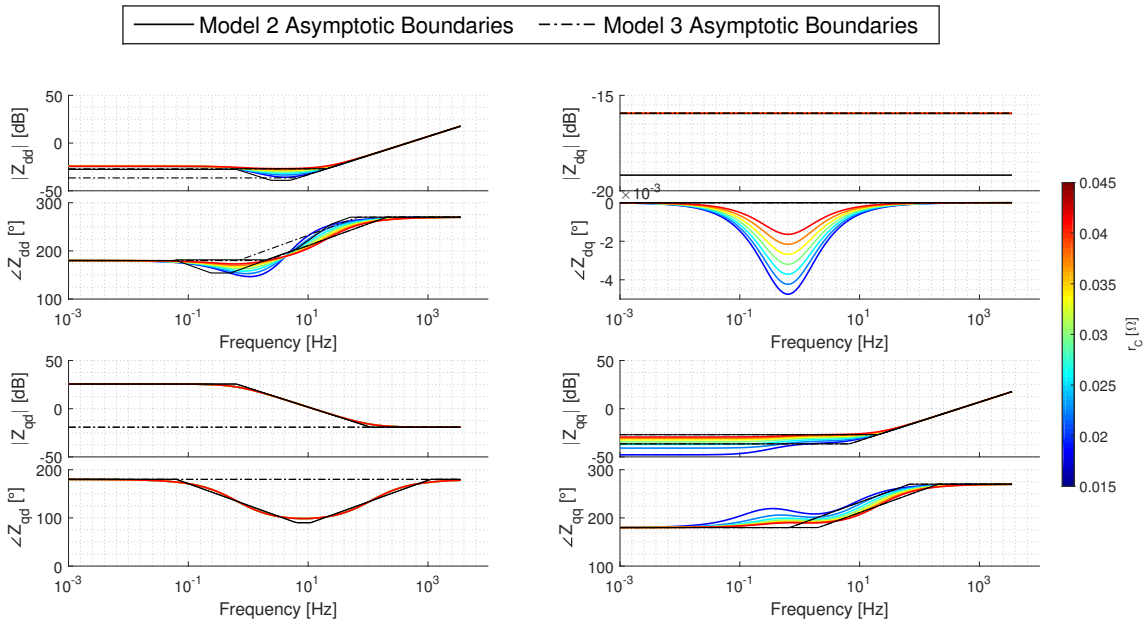

Figure A.39: M4 Small-Signal Impedance Sensitivity: r_C

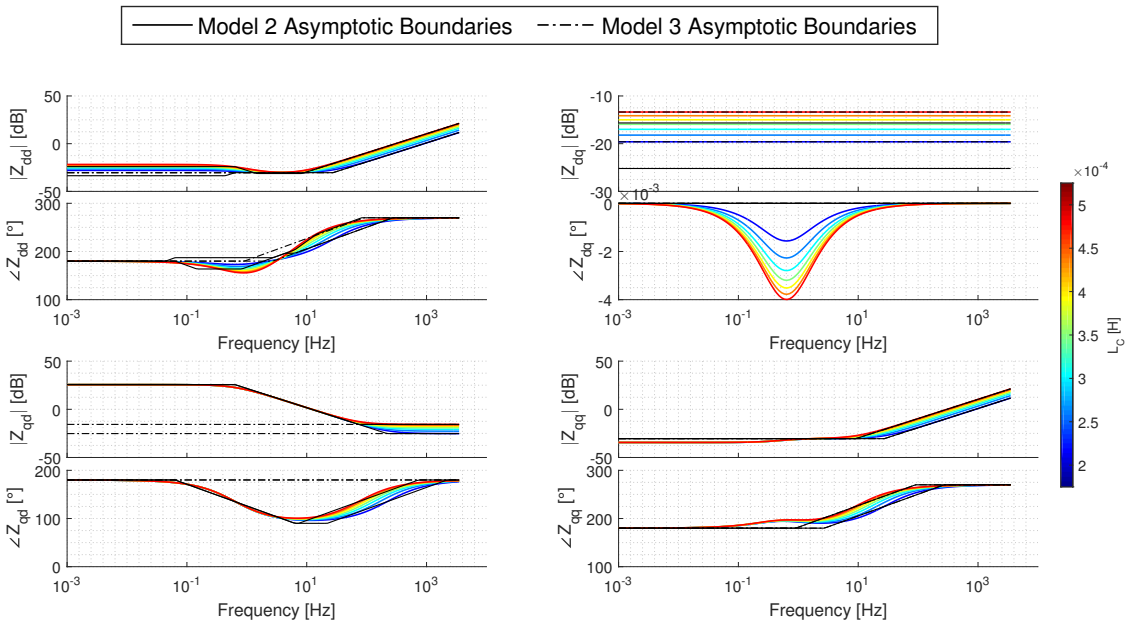

Figure A.40: M4 Small-Signal Impedance Sensitivity: L_C

A.5. M5: Active and Reactive Power Droop Controlled Source Considering LCL Filter

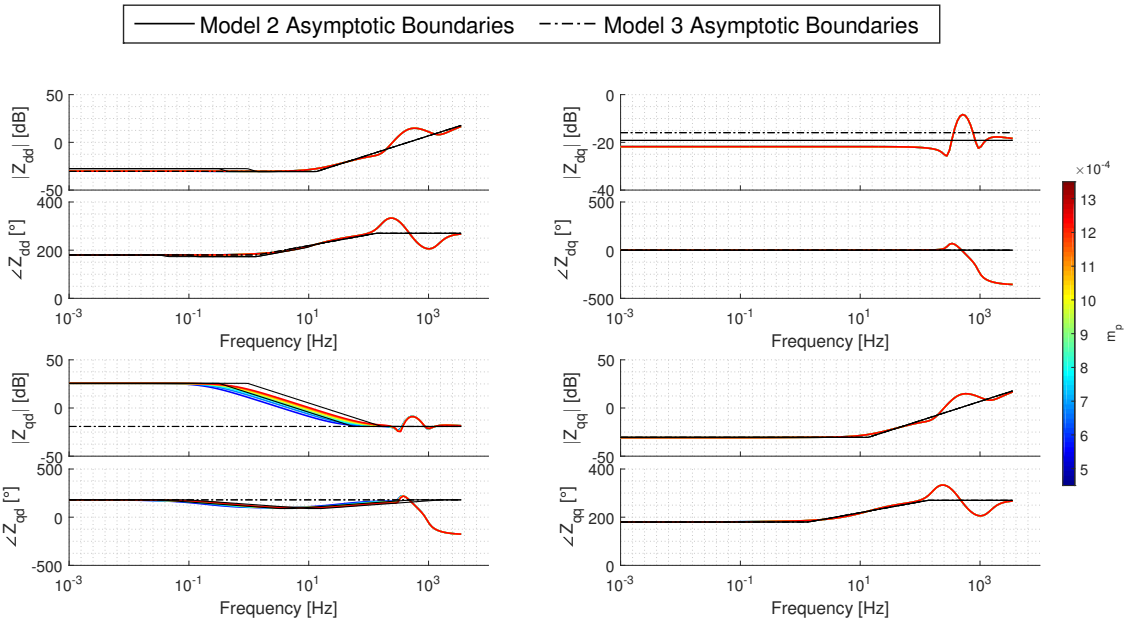

Figure A.41: M5 Small-Signal Impedance Sensitivity: m_p

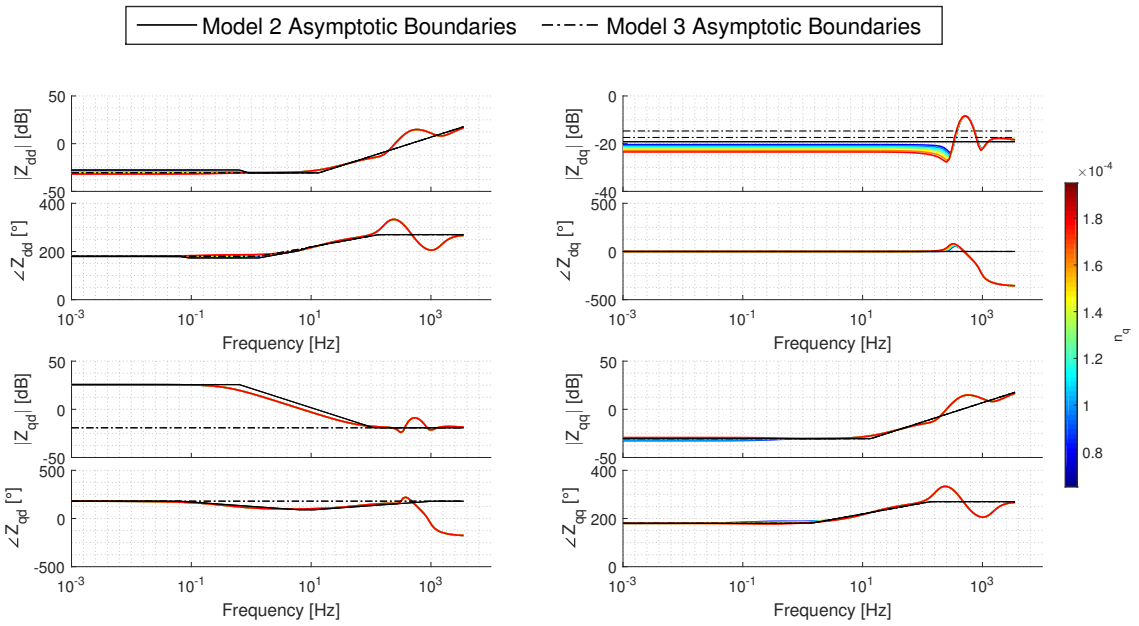

Figure A.42: M5 Small-Signal Impedance Sensitivity: n_q

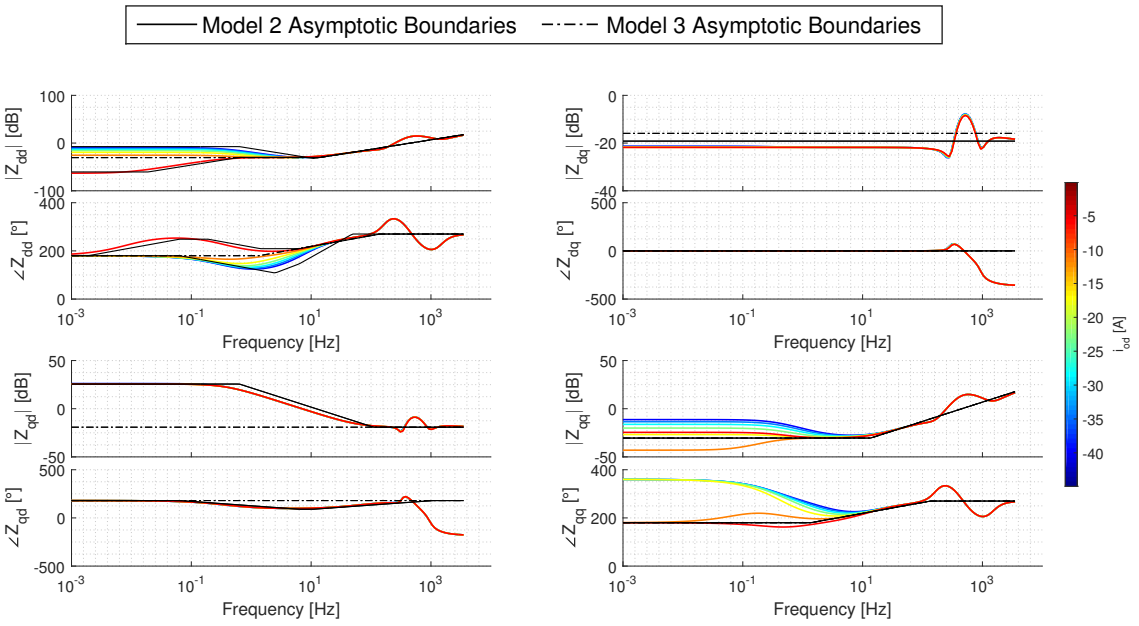

Figure A.43: M5 Small-Signal Impedance Sensitivity: $I_{od} < 0$

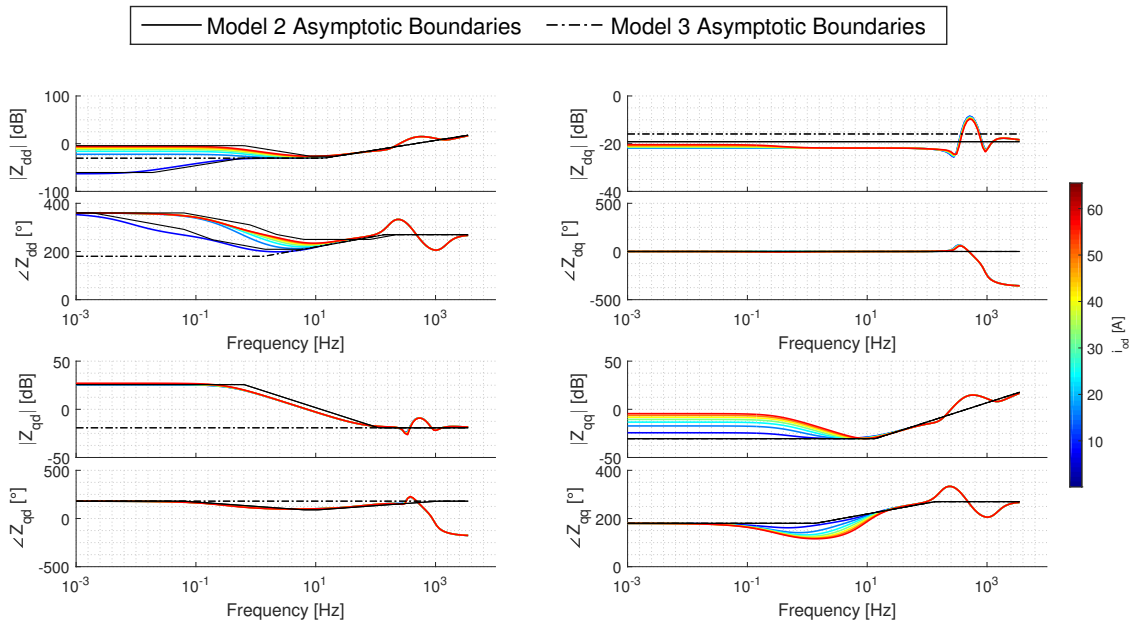

Figure A.44: M5 Small-Signal Impedance Sensitivity: $I_{od} > 0$

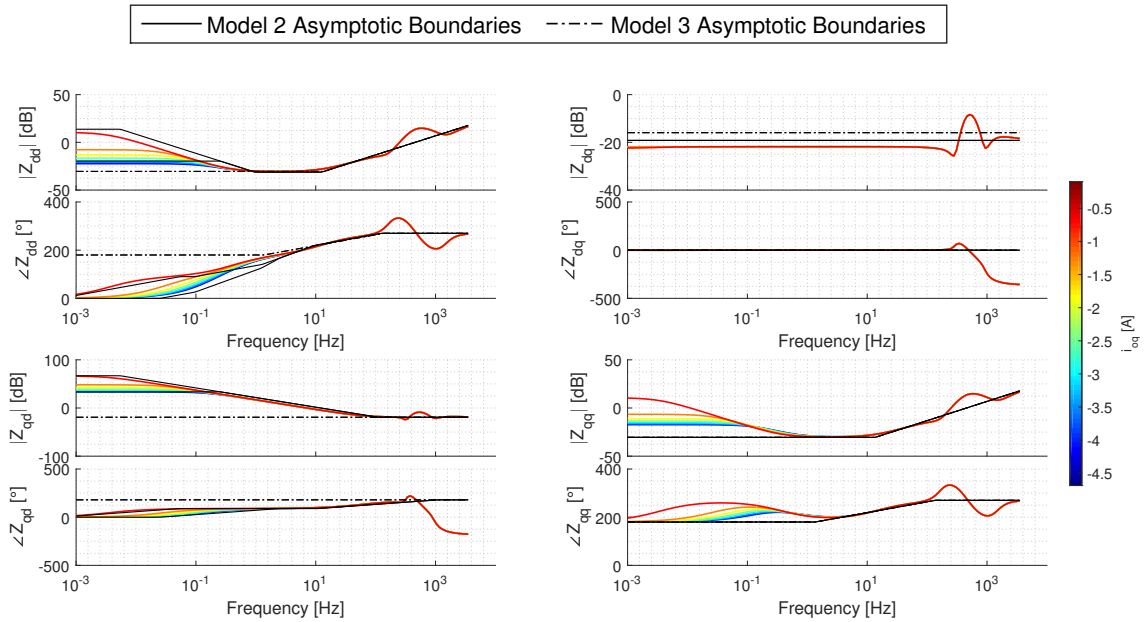

Figure A.45: M5 Small-Signal Impedance Sensitivity: $I_{oq} < 0$

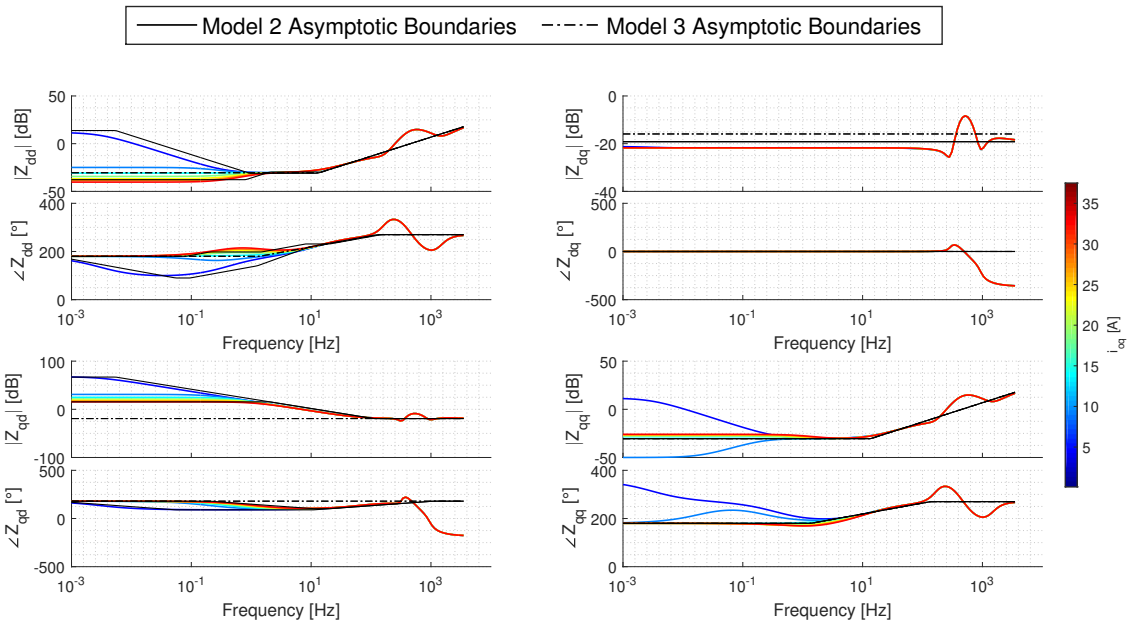

Figure A.46: M5 Small-Signal Impedance Sensitivity: $I_{oq} > 0$

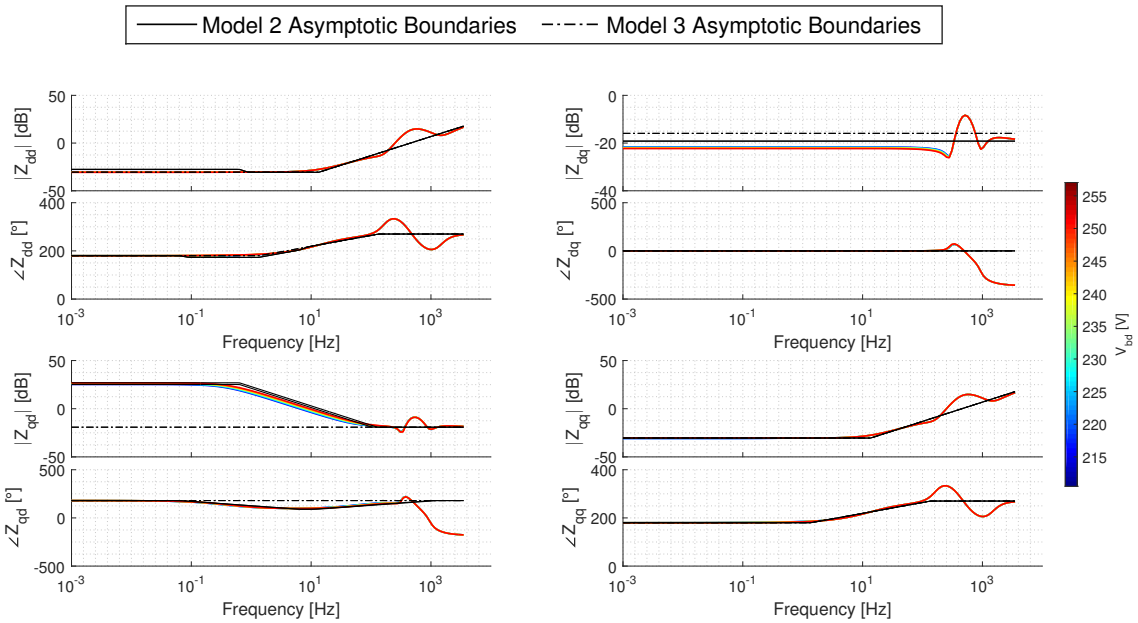

Figure A.47: M5 Small-Signal Impedance Sensitivity: V_{bD}

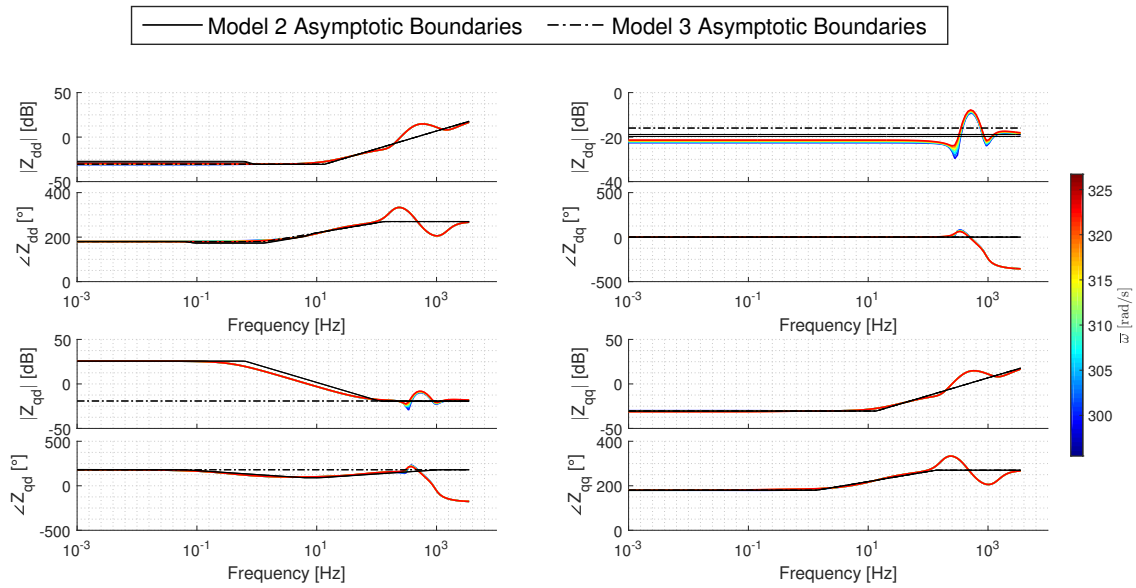

Figure A.48: M5 Small-Signal Impedance Sensitivity: $\overline{\omega}$

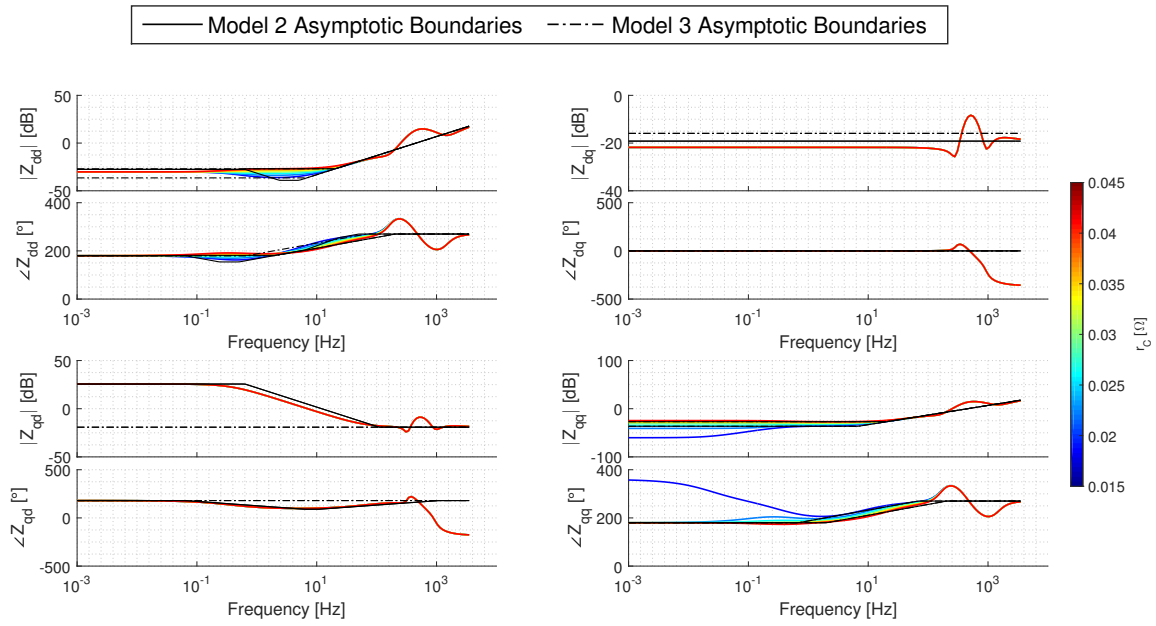

Figure A.49: M5 Small-Signal Impedance Sensitivity: r_C

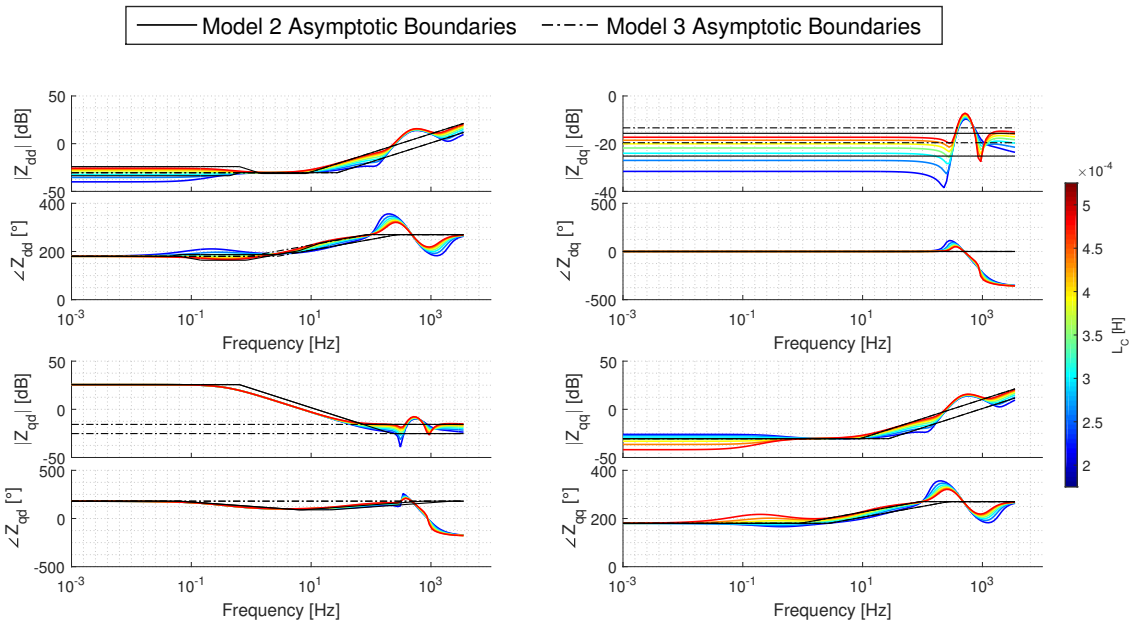

Figure A.50: M5 Small-Signal Impedance Sensitivity: L_C